ABSTRACT

ABOUELELLA, HAMDY. High-Temperature Mechanical Properties of Accident-Tolerant Fuel Cladding Materials. (Under the direction of Dr. K. L. Murty, and Dr. Jacob Eapen).

This thesis is on the creep behavior of high Cr-containing FeCrAl Advanced Powder Metallurgy Tubing (APMT) and 14YWT-NFA1 alloys. The observed APMT creep behavior revealed a transition between three regions. The first region at low stresses was characterized by dislocation viscous glide with a stress-exponent (n_I) of 2.8 and activation energy (Q_I) of 252.7 kJ/mol. The second region at intermediate stresses has a stress exponent (n_{II}) equal to ~ 7.45 and a high activation energy (Q_{II}) of 576 kJ/mol. The high stress third region is characterized by a high stress exponent (n_{III}) of 14.4 and high activation energy (Q_{III}) of 737.97±18.7 kJ/mol.

The threshold stress approach was employed to determine the dominant creep mechanism at the upper range of the examined stresses. Based on this analysis, dislocation-climb over precipitates facilitated by the increase in dislocation line length was found to be the creep rate-controlling mechanism at higher stresses, with a creep stress exponent of 6 and an activation energy of 252.8 ± 20.0 kJ/mol.

The modified Bird-Mukherjee-Dorn (BMD) equation was also utilized to find the stress exponent that best fit the data. The rate-controlling mechanism based on modified BMD equation was determined to be the dislocation-climb with a stress exponent equal to 6 in agreement with the results from the threshold stress approach.

The microstructural characterization of the APMT alloy provided preliminary evidence of the formation of (Cr, Mo)-rich carbides at the grain boundaries. The segregation observed might assist in locking the grain boundaries from sliding, thereby augmenting the overall strength of the material.

The 14YWT-NFA1 creep study revealed unique characteristics, featuring a transition between two distinct regions. The stress exponent *n*, is approximately one in the low stress region, coupled with the activation energy Q = 244.58 kJ/mol, suggesting the dominance of Nabarro-Herring lattice diffusion-controlled creep mechanism at lower stresses. In the high stress region, however, a stress exponent of around 15 and an activation energy Q of 388.56 kJ/mol highlight the role of precipitates as dislocation barriers.

BF-TEM images revealed that the grain structure remained stable due potentially to the presence of precipitates along the grain boundaries. Another observation was the existence of two distinct types of precipitates, W-rich and Y-Ti-O rich, which never co-occurred on the same grain boundary in the characterized area. The TEM-EDS mapping for W after creep tests demonstrated concentrated localizations at the grain boundaries with no signs of W inside the grains. In addition to that, the 14YWT-NFA1 alloy exhibits inherent microstructural deficiencies such as voids and micro-cracks in the as-received condition.

Molecular dynamics investigations analyzed the effect of Cr and Al on the ductility of FeCrAl system. The process started by verifying the reliability and accuracy of the interatomic potential used for the simulations accomplished through a series of tests, including lattice parameter calculations, and melting temperature using both single and two-phase melting methods. The impact of changing the Cr and Al content on the ductility of the FeCrAl supercell was studied and a local compositional space with Cr content of 18 at. % showed improved ductility, although the Al content needs to be controlled as it was observed to decrease the ductility with increasing content. In the light of these findings, the maximum ductility values were found in supercells with 18 at. % Cr and (2-3 at. %) Al content.

High-Temperature Mechanical Properties of Accident-Tolerant Fuel Cladding Materials

by
Hamdy Salah Abouelella

A dissertation submitted to the Graduate Faculty of
North Carolina State University
in partial fulfillment of the
requirements for the degree of
Doctor of Philosophy

Nuclear Engineering

Raleigh, North Carolina
2023

APPROVED BY:

_____	_____
Dr. K. L. Murty Co-Chair of Advisory Committee	Dr. Jacob Eapen Co-Chair of Advisory Committee
_____	_____
Dr. Tasnim Hassan	Dr. Benjamin Beeler
_____	
Dr. Lingfeng He	

DEDICATION

To my beloved wife, Wafaa,

To my precious daughter, Hana,

To my wonderful son, Mostafa,

To my loving parents, Salah, and Ibtisam,

To my dear brothers, Mohamed, and Mostafa,

And to the cherished memory of my late brother, Fathy.

Your unwavering love, support, and presence in my life have been invaluable. This dedication is a testament to the profound impact you had on shaping who I am today.

BIOGRAPHY

Hamdy Abouelella was born in Berkit Alsab, a quaint city situated just 40 minutes away from Cairo, the bustling capital of Egypt. His early education unfolded in this serene setting, building the foundation of his academic journey. Hamdy's quest for knowledge and his exemplary academic performance were evident from the outset. He consistently ranked among the top students in his classes, exhibiting an innate aptitude and dedication to learning.

In 2010, Hamdy relocated to Alexandria, in northern Egypt, to pursue higher education. He was admitted to a college where he chose to study Nuclear Engineering - a field that would come to define his career. His unwavering commitment to academics continued, and in 2014, he graduated with honors.

Following graduation, Hamdy became part of an illustrious research team that was backed by the International Atomic Energy Agency. The team's focus was the comprehensive study of the Fukushima accident and its repercussions on reactor structures. This experience provided Hamdy with invaluable insights and exposure to cutting-edge research in nuclear engineering.

In 2016, Hamdy’s path led him to Zewail City of Science and Technology, where he assumed the dual role of a research and teaching assistant. For three years, he contributed to both educational endeavors and research initiatives, honing his skills and deepening his understanding of the field.

A significant turning point in Hamdy’s career was in 2020 when he crossed continents to join the Department of Nuclear Engineering at North Carolina State University (NCSU) in Raleigh, NC, USA. Here, he embarked on his Ph.D. program in Nuclear Engineering, taking steps toward fulfilling his higher education aspirations.

Under the esteemed supervision of Dr. K. L. Murty, Hamdy became an integral part of the Nuclear Material Research Group at NCSU. His Ph.D. research was concentrated on high-temperature mechanical properties for accident-tolerant fuel cladding materials. This work is poised to make a significant contribution to the field of Nuclear Engineering.

Hamdy Abouelella's journey, from the small city of Berkit Alsab to the renowned halls of North Carolina State University, is a testament to his relentless pursuit of knowledge, his unwavering commitment to excellence, and his contributions to the ever-evolving field of Nuclear Engineering.

ACKNOWLEDGMENTS

In the Name of Allah, the Most Gracious, the Most Merciful.

First and foremost, I raise my heart in gratitude and praise to Allah (God), the source of all wisdom and knowledge, for blessing me with the perseverance, strength, and patience required to accomplish this work. This achievement is a testament to the boundless grace and empowerment He bestows upon His creation.

I would like to express my deepest admiration and gratitude to my supervisor, Prof. K.L. Murty. His relentless support, encouragement, and incisive guidance have been instrumental in shaping my scholarly pursuit. I remain deeply thankful for the profound advice he provided, allowing me to delve into the myriad dimensions of research, articulation, and publication. Prof. Murty's astute supervision and uplifting remarks have not only enriched this work but have also laid the foundation for my future as a contributor to the scientific community. It has been a privilege and an honor to be under the tutelage of such an esteemed mentor.

Additionally, my heartfelt appreciation extends to my Co-advisor, Prof. Jacob Eapen, whose invaluable insights have been a cornerstone in my academic development. Through him, I learned the essence of critical thinking and an acute attention to detail. His teachings have opened my eyes to the vast realms of simulation, for which I am eternally grateful.

My sincere gratitude to Dr. Benjamin Beeler, whose unwavering assistance has been an anchor through the turbulence of my Ph.D. journey. His generosity in offering his time, support, and guidance was a light that guided me through the challenges I faced. I extend my sincere appreciation to the esteemed committee members, Prof. Tasnim Hassan and Dr. Lingfeng He, for their invaluable time and contributions. Their insightful discussions and constructive feedback were paramount in refining my work. I am also thankful to Rajnikant Umretiya, Andrew Hoffman,

Raul Rebak, and Evan Dolley from General Electric Research Center, whose collaboration and input were indispensable.

I also acknowledge the financial support provided by the United States Department of Energy under grant number DE-NE-0009047. We also would like to express our gratitude to Prof. Indrajit Charit from the University of Idaho for generously providing the essential materials for this research.

Now, turning to the bedrock of my life - my family. To my beloved wife, children, parents, and brothers, your unwavering support and love have been the pillars upon which my resolve was built. You have been my refuge and my strength. I am immensely grateful for your sacrifices and understanding. To my friends, who have been my comrades in this journey, thank you for your camaraderie, encouragement, and good humor that lightened my path.

Lastly, I humbly ask for forgiveness from my family for any shortcomings on my part during this arduous journey. My dedication to this pursuit may have caused times of absence or preoccupation, for which I am sincerely sorry. This Ph.D. is not just a testament to my academic pursuit, but a tapestry woven with the threads of support, love, and guidance from all of you.

Alhamdulillah, thank you.

TABLE OF CONTENTS

LIST OF TABLES

LIST OF FIGURES

Dissertation Overview

The cornerstone of this research endeavor is an investigation of the creep properties of two distinct alloys, namely Advanced Powder Metallurgy Tubing (APMT) and 14YWT Nanostructured Ferritic Alloy (14YWT-NFA1). These alloys are in contention to be employed as structural materials for advanced water-cooled reactors as well as fusion reactors, signifying their potential importance in the realm of nuclear energy. To achieve an understanding of the creep behavior of APMT and 14YWT-NFA1, a series of tensile creep tests were carried out across a range of temperatures. These experiments are aimed at gauging how the materials respond to prolonged stress under varying thermal conditions.

In Chapter 1, the dissertation begins by setting the stage with an introduction that sheds light about accident-tolerant fuel cladding materials. The relevance and criticality of advancing structural materials for nuclear reactors, encompassing both fission and fusion reactors, are elucidated.

As the chapter progresses, it covers a concise yet informative overview of various FeCrAl alloys. This segment explores the diversity of FeCrAl alloys and their respective characteristics. Furthermore, the chapter addresses the driving forces and motivations behind undertaking this study. In essence, Chapter 1 serves as the gateway to the dissertation by providing a glimpse into the realm of accident-tolerant fuel cladding materials, the landscape of FeCrAl alloys, and the motivations steering this research.

Chapter 2 delineates the experimental methods and techniques employed throughout this research. It outlines the steps of creep tests, thereby enabling an understanding of the tests performed. The third chapter introduces the domain of molecular dynamics, focusing particularly on the concept of ensembles and interatomic potentials. It aims to establish an understanding of

the functioning of ensembles and the role of interatomic potentials, and this chapter sets the stage for the more advanced and specific topics discussed in Chapter 6.

In Chapter 4, the focus is on the creep properties of APMT. This chapter commences with an introductory section that gives an overview of the scholarly landscape surrounding APMT. This foundation paves the way for the subsequent analyses. Subsequently, the chapter discusses the analysis of the results, focusing on the creep behavior and microstructural evolution of the APMT alloy at elevated temperatures. Microstructure of the as-received material is presented and discussed followed by the creep results.

In Chapter 5, the dissertation takes a close look at what other researchers have already found out about the 14YWT-NFA1. The chapter starts by introducing what has been studied so far. Next, the chapter goes into the details of the microstructure and features of the 14YWT-NFA1 tested in this work. The chapter then presents the results of the creep tests including creep curves that show how the material creep behavior changed under different conditions.

In Chapter 6, the spotlight turns to an in-depth exploration using molecular dynamics simulations to understand the effect of composition on the ductility of FeCrAl alloy, executed using the Large-scale Atomic/Molecular Massively Parallel Simulator (LAMMPS). The first segment of this chapter is dedicated to establishing the credibility of the interatomic potentials employed to depict the interactions among atoms. A salient step in this validation process involves the computation of the equilibrium lattice constant at room temperature and comparing with the lattice parameter obtained through x-ray diffraction experiments. Additionally, the chapter ventures into the calculation of the melting temperature of the FeCrAl alloy and compare it with its experimental counterpart. This serves as another crucial validation measure for the interatomic

potential. Having established the reliability of the interatomic potential, the chapter proceeds to the discussion of the effects of Al and Cr content on the ductility of FeCrAl system.

The last chapter serves as the culmination of the dissertation, where it encapsulates the key takeaways concerning the creep properties observed in the APMT and 14YWT-NFA1 alloys. This chapter synthesizes the salient findings and reflects on the broader implications and significance of the results obtained for both materials.

In addition to summarizing and contextualizing the core observations, the chapter looks toward the horizon by delineating an array of prospective research endeavors pertaining to both APMT and 14YWT-NFA1 alloys. The areas earmarked for future exploration encompass the optimization of material composition to enhance performance, as well as in-depth studies into the fracture toughness, fatigue, and the interplay between creep and fatigue properties of the alloys.

1. Introduction and Motivation

1. Background

The quest for sustainable and clean energy sources has brought nuclear power into the spotlight [1]. As the world grapples with the challenges of climate change, the development of advanced structural materials for nuclear reactors, both fission and fusion, is emerging as a critical area of research [2]. Nuclear fission reactors have been in operation for over half a century, producing electricity by splitting heavy atomic nuclei [3]. Conversely, nuclear fusion seeks to generate power by combining light atomic nuclei, mirroring the process that powers the sun. While fission is a mature technology, fusion is still in the experimental phase. Both technologies present unique challenges that hinge significantly on the properties and performance of structural materials [4].

The catastrophic events at Fukushima highlighted the vulnerability of current fission reactor designs [5]. Advancing structural materials, particularly fuel cladding, is essential for enhancing safety. Materials that can withstand extreme temperatures without undergoing rapid oxidation can mitigate the consequences of severe accidents [6].

Such advanced cladding materials will not only ensure safety but also allow operating reactors for longer periods between maintenance and achieving higher burnups of nuclear fuel, and directly contribute to economic efficiency. Advanced structural materials can endure radiation damage and high temperatures better than traditional materials. This could reduce the volume and radiotoxicity of the waste produced, alleviating one of the most significant challenges facing nuclear power [7].

Materials for fusion reactors are subject to an unrivaled combination of high temperatures, neutron bombardment, and chemical reactivity. Existing materials are inadequate for such

conditions and developing materials that can withstand this environment is indispensable for realizing nuclear fusion [8].

Advancing structural materials in nuclear reactors is at the heart of unlocking the full potential of nuclear power, both fission and fusion [9]. The development is not just an incremental step but an imperative leap toward establishing a safe, sustainable, and efficient nuclear energy landscape. Through continuous research and innovation in materials science, society can edge closer to a future where nuclear energy significantly contributes to global energy security and climate change mitigation.

2. History of Accident Tolerant Fuels Program

Accident tolerant fuels (ATFs) are a relatively new material development research program in the field of nuclear energy [10], which has been actively pursued since the Fukushima disaster in 2011 [5]. Before the Fukushima disaster, nuclear fuel research focused mainly on improving fuel performance and economics, but not as much on accident tolerance [3].

2.1. Fukushima Disaster

The Fukushima Daiichi nuclear disaster [5], which occurred in March 2011, was the result of a complex interaction between natural events and the material limitations of the nuclear reactors. On March 11, 2011, a magnitude 9.0 earthquake struck off the coast of Japan. The reactors at the Fukushima Daiichi Nuclear Power Plant were designed to withstand earthquakes, and initially, the safety systems functioned as intended. However, approximately 45 minutes later, a massive tsunami hit the coast. The tsunami's height exceeded the seawall that was designed to protect the plant, flooding the site. The flooding caused by the tsunami disabled the backup diesel generators needed to maintain the cooling systems, leading to a complete loss of power.

Without sufficient cooling, the fuel rods began to heat up. The Zr cladding around the fuel reacted with steam to produce Zr-oxide and H. This is an exothermic reaction, which further increased the temperature. As temperatures continued to rise, the fuel rods (Zr cladding) began to fail. The nuclear fuel, made primarily of UO_2, started to melt. The melted fuel, cladding, and other materials formed a highly radioactive mass known as corium, which began to eat through the containment structures. The production of H from the reaction between Zr cladding and steam led to the accumulation of H gas in the reactor buildings.

H is highly flammable, and the buildup of H gas led to several explosions. This not only damaged the reactor buildings but also complicated the efforts to stabilize the reactors [5]. The damage to the reactor vessels and containment structures, as well as the H explosions, resulted in the release of radioactive materials into the environment. Radioisotopes such as iodine-131, cesium-134, and cesium-137 were released, leading to contamination of the surrounding areas and the evacuation of residents. The disaster highlighted the vulnerability of the Zr-based cladding used in fuel rods, particularly its reaction with water at high temperatures to produce H. This led to a global re-evaluation of nuclear power plant materials and designs. Research into accident-tolerant fuels, with alternate cladding materials and fuel matrices that can better withstand severe accident conditions, intensified.

2.2. U.S. Department of Energy Initiative

In response to the Fukushima Daiichi nuclear disaster in 2011, the U.S. Department of Energy (DOE) launched an initiative in 2012 to develop Accident Tolerant Fuels for light-water reactors [6, 11-14]. The goal of the initiative was to enhance the safety and performance of nuclear fuel under normal and accident conditions. The primary objective was to develop fuel and cladding materials that can tolerate loss of active cooling in the core for a considerably longer time than the

existing Zr-UO_2 system, while maintaining or improving performance during normal operations [15-17].

2.3. Collaboration and Research: In the years following 2011

Several companies and national laboratories were involved in the U.S. Department of Energy's ATF program. Starting with the companies involved, Westinghouse Electric Company [18] is working on developing advanced cladding materials, including coated Zr cladding, which aims to reduce oxidation and H generation in accident conditions. They are also exploring alternative fuel forms. Framatome [19] is developing Cr-coated Zr cladding and working on advanced fuel pellets, including Cr-doped UO_2 and chromia-enhanced UO_2, which exhibit better thermal conductivity compared to standard fuel. General Electric (GE) [15, 16] through its Global Nuclear Fuel (GNF) joint venture, is working on Ironclad (FeCrAl) alloy cladding, and a new coating concept known as ARMOR.

Moving forward to national labs involved in the ATF program. Idaho National Laboratory (INL) [20, 21] is a key player in the ATF program, conducting experiments and testing on ATF concepts. It hosts the Transient Reactor Test Facility, which is crucial for testing how fuels behave under simulated accident conditions.

Oak Ridge National Laboratory (ORNL) [10, 14, 17] is involved in materials testing and characterization of ATF candidates. They focused on understanding the behavior of materials under irradiation and the high-temperature environment of a reactor core. Argonne National Laboratory (ANL) [10] is involved in modeling and simulation to predict the behavior of ATF materials under various conditions, as well as testing and characterization of materials. Los Alamos National Laboratory (LANL) [4] conducts research on materials science and nuclear engineering to support the development of ATFs, including understanding the behavior of materials under high

radiation fields. Lawrence Livermore National Laboratory (LLNL) is involved in modeling and simulations, providing critical data to understand and predict the behavior of new materials under reactor conditions.

The ATF program fostered collaboration between companies, national labs, universities, and international partners. Each participant brought unique capabilities and expertise to the table, ranging from materials development and fuel fabrication to testing, modeling, and simulation.

2.4. Fuel Cladding Research

Fuel cladding is a critical component in nuclear fuel assemblies, serving as a barrier between the nuclear fuel and the reactor coolant [7, 9]. In the context of the ATF program, enhancing the performance and safety of fuel cladding, especially during severe accident conditions, is a major focus. Traditional fuel cladding is made of Zr alloys, which, while effective under normal conditions, can rapidly oxidize at high temperatures, leading to H generation and potential failure [22]. One approach within the ATF program is to apply coatings to Zr-alloy cladding to reduce oxidation. Cr coatings, for example, have been developed by Framatome [19] to reduce the rate of high-temperature oxidation. SiC [23] composite cladding is a promising alternative to Zr alloys. SiC is a ceramic material with high melting temperature, excellent chemical stability, and low neutron absorption. SiC composite cladding is expected to provide significantly improved performance during loss-of-coolant accidents due to its high-temperature stability and resistance to oxidation. FeCrAl alloys [17, 24-29] have been developed as an alternative cladding material. This alloy, also being developed by GE through GNF, has shown excellent oxidation resistance and mechanical strength at high temperatures. The alloy aims to provide a more robust cladding option compared to traditional Zr alloys.

2.5. First In-Reactor Tests

The first in-reactor tests for ATF concepts were carried out as part of the DOE ATF program. The first in-reactor tests involved installing Lead Test Assemblies (LTAs) containing ATF concepts into operating commercial nuclear reactors. This step was crucial out as it allowed researchers to evaluate the performance of new fuel and cladding materials under actual reactor conditions.

In 2013, the French fuel vendor Framatome [30] announced the first insertion of Cr-coated fuel rods into the Calvert Cliffs Nuclear Power Plant in Maryland, USA. This test aimed to evaluate the performance of Cr-coated Zr cladding, which is intended to provide better oxidation resistance compared to traditional Zr cladding.

In 2018, Southern Nuclear Operating Company, in collaboration with GNF [31], installed IronClad and ARMOR lead test rods at its Hatch Nuclear Power Plant in Georgia, USA. IronClad is a FeCrAl alloy cladding designed for better oxidation resistance. While ARMOR is, a coating applied to standard Zr cladding to improve its high-temperature performance.

In the same year, the U.S. utility Tennessee Valley Authority (TVA), in collaboration with Westinghouse and Framatome [18], installed LTAs with advanced cladding materials and doped fuel pellets into the Watts Bar Nuclear Plant Unit 2 reactor in Tennessee, USA. These tests were intended to evaluate various ATF concepts, including coated Zr cladding and advanced fuel pellet designs.

These first in-reactor tests of ATF concepts were critical milestones in the development and deployment of accident-tolerant fuels by evaluating these new materials and fuel designs under real-world conditions.

3. FeCrAl Cladding Concept

FeCrAl alloys [32-35] have been used in industrial applications where high-temperature oxidation resistance is needed. FeCrAl alloys have a unique ability to form a protective oxide layer, which shields the material from detrimental environmental conditions, particularly at elevated temperatures. This characteristic has positioned FeCrAl alloys as indispensable in a myriad of industrial applications such as heating elements, furnace components, aerospace components and nuclear reactor structural materials [36-38].

3.1. GNF FeCrAl Alloys

FeCrAl alloys are composed of Fe, Cr, and Al, along with small amounts of other elements to achieve specific properties [39, 40]. There are several commercially available variants, but the focus of U.S. research and development programs is primarily on creating a nuclear grade version that is resistant to oxidation. In contrast, Japanese research is centered on Oxide Dispersion Strengthened (ODS) FeCrAl alloys.

GNF is evaluating three types of alloys: C26M, developed by ORNL; Kanthal APMT, produced by the Kanthal company; and MA956, which is commercially available. C26M consists primarily of 12 wt.% Cr, 6 wt.% Al, and 2 wt.% Mo, with the remainder being Fe. It is fabricated using conventional melting methods. Kanthal APMT is a commercially available alloy produced through ODS powder metallurgy, boasting a higher Cr content (22 wt.%) and a finer grain structure. Notably, this alloy is the subject of the studies presented in this document, with its higher Cr content significantly improving corrosion resistance in comparison to other FeCrAl alloys. MA956 is another commercially available ODS FeCrAl alloy, with a composition of 22 wt.% Cr, 6 wt.% Al, plus minor alloying elements, and is manufactured by mechanical alloying [39, 40].

3.2. FeCrAl Design

FeCrAl alloys possess a fully ferritic (body-centered cubic, BCC), structure and typically do not undergo phase transformations between the liquidus temperature and room temperature [33, 34]. Cr additions enhance corrosion resistance by forming chromia layer under normal conditions. In contrast, Al additions bolster resistance to oxidation at high temperatures by creating an Al-oxide layer under extreme conditions. Moreover, Cr stabilizes the Al layer in high-temperature steam [24, 28, 29].

It is vital to strike a balance between Cr and Al contents for both surface protection and controlling material properties. Excessive Cr content can lead to embrittlement due to the precipitation of Cr-rich brittle phase. Incorporating small quantities of Y can enhance the oxidation resistance of the alloy. ODS variants tend to exhibit higher strength and increased resistance to deformation at high temperatures due to the dispersion of fine oxide particles [40-42]. At ORNL, alloying additions of Mo and Nb have been employed to bolster alloy strength. Mo fortifies the alloy through solid-solution hardening, while Nb enhances strength through precipitate strengthening [43, 44].

4. Alloy 14YWT

Alloy 14YWT is a nanostructured ferritic alloy (NFA) that has garnered attention for its remarkable properties, such as high-temperature strength, and superior radiation tolerance [45]. It is an alloy that comprises Fe as the base element, enriched with W, Ti, and Y, with a composition primarily developed for nuclear applications [46-48].

Alloy 14YWT was developed as a part of the advanced materials development efforts by ORNL in the United States [49]. The inception of this alloy traces back to the late 20th and early 21st centuries when there was an increasing demand for materials that can withstand the harsh

environments found in advanced nuclear reactors [45]. Traditional materials like stainless steel suffered from degradation when exposed to high levels of radiation, leading to a quest for novel materials. 14YWT emerged as a potential candidate, with its unique microstructure characterized by a high density of nanoscale Y-Ti-O-enriched clusters, which played a crucial role in imparting the desired properties [8, 50].

One of the potential applications of alloy 14YWT is in the nuclear industry, particularly for the structural components in advanced nuclear reactors [4]. Its radiation resistance makes it highly suitable for such applications, where materials are subjected to extreme radiation fields. This is especially pertinent in Generation IV nuclear reactors and fusion reactors where service conditions are much harsher compared to the current generations. Apart from nuclear applications, alloy 14YWT's high-temperature strength make it a promising candidate for the aerospace and aviation industries [51-54]. Components in aircraft engines, for instance, require materials that can withstand high temperatures and stress.

The unique microstructure of 14YWT that imparts its desirable properties also presents challenges in terms of fabrication and formability [53, 55-58]. Traditional fabrication methods may not be appropriate, and new techniques must be developed. The incorporation of elements such as Y and W makes this alloy more expensive compared to traditional structural materials. This could limit its adoption in industries that are highly cost sensitive. In addition, scaling the production of 14YWT for large-scale applications is a challenge. Research and development are required for establishing manufacturing processes that can produce this alloy in large quantities without compromising its properties.

There is a limited amount of long-term data available regarding the behavior of alloy 14YWT under prolonged exposure to extreme conditions. More research and testing are needed to

fully understand its performance and reliability. In conclusion, Alloy 14YWT is a highly promising material with exceptional properties that make it suitable for applications in demanding environments such as the nuclear industry, aerospace, and automotive industries. However, challenges such as fabrication, cost, and scaling need to be addressed for this material to realize its full potential and see widespread adoption.

5. Carbide Precipitates in Steels

Steels are fundamentally alloys of Fe and C, with C concentration typically ranging from less than 0.03% in low C steels to over 2% in high C steels [59, 60]. In addition to C, steels can contain other alloying elements such as Cr, Ni, Mo, W, and V, which serve to enhance properties like hardness, toughness, and resistance to corrosion and wear.

In steels, C can exist either in solution within the Fe matrix, forming a solid solution called austenite or ferrite (depending on the temperature), or it can precipitate out of the solution as carbides [60-62]. These carbides can be either Fe-based (Fe_3C, also known as cementite), or based on other alloying elements present in the steel. Under certain temperature and time conditions, carbide precipitates, specifically $M_{23}C_6$, can form [59, 62]. This typically occurs during the tempering heat treatment process, which is carried out after hardening to reduce the brittleness of the steel. During this process, the C that was in solution in the austenite phase can precipitate out as carbides, thereby enhancing the steel's toughness. $M_{23}C_6$ carbides are the most predominant precipitates [59, 60] where 'M' refers to the carbide-forming element, primarily Cr, but other metallic elements like Fe, Mo, and Ni can partially substitute for Cr. $M_{23}C_6$ has a face-centered cubic (FCC) crystal structure, with a lattice parameter approximately three times larger than that of the austenite matrix [63]. The size, distribution, and type of $M_{23}C_6$ precipitates can greatly influence the steel's mechanical properties [60]. For instance, fine and evenly distributed $M_{23}C_6$

can enhance the hardness and strength of the steel, whereas larger and unevenly distributed $M_{23}C_6$ can decrease its toughness. Moreover, some types of $M_{23}C_6$ carbides (like those of Cr, W, and V) are more stable and harder than Fe carbides, which is why steels containing these carbides are often used in applications requiring high wear resistance [64]. However, not all carbides are beneficial. For instance, in certain stainless steels, the formation of $Cr_{23}C_6$ at grain boundaries can lead to a phenomenon known as sensitization, which significantly undermines the steel's corrosion resistance [62].

Researchers reported that the presence of $M_{23}C_6$ carbides within the matrix and grain boundaries could enhance high temperature creep strength by restricting dislocation movement and making grain boundary sliding more difficult [65]. Nonetheless, due to their relatively high coarsening rates, $M_{23}C_6$ carbides can lose their strengthening effect over time, making them less attractive for high-temperature applications. Furthermore, $M_{23}C_6$ carbides can negatively affect corrosion resistance, ductility, and toughness, which is why elements like N and Nb [66] added to austenitic stainless steels suppress the formation of $M_{23}C_6$ carbides, either by reducing C solubility or by forming more stable carbo-nitrides.

6. Creep

Creep is a phenomenon that occurs in materials where they deform over time under the influence of a constant or sustained stress [9, 67, 68]. This deformation is usually plastic, meaning it is permanent and the material does not return to its original shape once the stress is removed. Creep is especially significant when the material is subjected to high temperatures, typically around 0.4 to 0.5 times its melting temperature.

The underlying mechanisms of creep can include not only the movement of dislocations but also the diffusion of vacancies or atoms. Creep is generally more prominent at high

temperatures because the diffusion of vacancies occurs at a much faster rate. However, it's important to note that some materials can experience creep even at room temperature or below.

Creep as a phenomenon was observed several centuries ago, but it gained technological relevance primarily in the 20th century with the boom in industrialization. The need to develop steam engines, generators, and jet engine blades, which operate at high temperatures, necessitated the creation of heat-resistant materials capable of maintaining their integrity over extended periods. This sparked focused research in the field of creep, a pursuit that continues to this day to meet the evolving demands of industrial advancement [68-70].

6.1. Creep curve

A creep curve is a graphical representation of the phenomenon of creep, which is the tendency of a solid material to deform under the influence of a constant stress, usually at high temperature. The curve typically plots strain against time for a material under a constant applied stress and temperature [9].A typical creep curve given in (Fig. 1.1) features three main stages or regions. The initial stage known as primary creep (or transient creep), where the strain rate decreases with time. The material is starting to deform under the applied stress, and various mechanisms such as work hardening, or strain hardening occur. The second stage is the secondary creep (or steady-state creep), where the strain rate becomes almost constant over time. It is the longest stage of the creep curve. The balance between the work hardening and recovery (or softening) mechanisms is achieved, leading to a constant rate of deformation [68-70].

The third and final stage is the tertiary creep (or accelerated creep), where the strain rate rapidly increases until failure. This stage is characterized by damage accumulation, such as grain boundary separation, cavitation, and the initiation and growth of internal cracks. The material eventually fails at the end of this stage. It is important to note that not all materials exhibit all three

stages. For some materials under certain conditions, they may go from primary directly to tertiary creep, or remain in the secondary creep stage for a prolonged period until the removal of the stress [68-70].

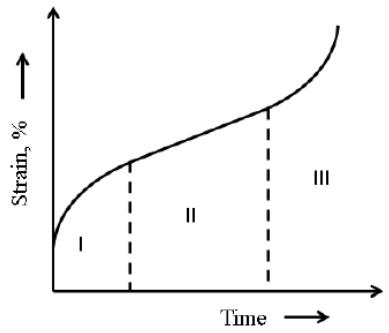

Figure 1.1. A typical creep curve with three stages marked as (I) primary creep (II) secondary or steady state creep and (III) tertiary creep.

The rate of deformation, or strain, increases with both increasing stress and increasing temperature as shown in (Fig. 1.2). Thus, components subjected to high temperatures and pressures, such as jet engine parts, steam turbine blades, or structural components in nuclear power plants, can suffer from creep deformation, affecting their lifespan and reliability. The strain accumulated in materials in the steady state creep regime is a significant fraction of the creep fracture strain, which is usually the case. Temperature and stress variations of the steady state creep regime are of great interest to comprehend the underlying creep mechanisms such as dislocation creep and diffusional creep [68-70].

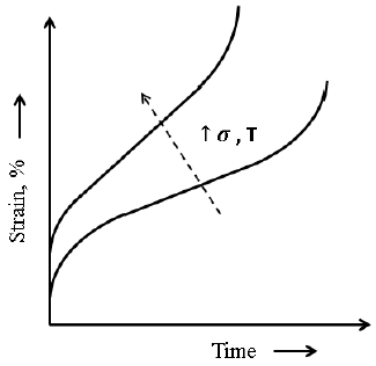

Figure 1.2. The steady state creep rate increases as stress and temperature increase.

6.2. Mechanisms of creep

This section delves into the intricate mechanisms underlying the phenomenon of creep. A thorough understanding of creep mechanisms is not only central to material science and engineering but also critical to the design and longevity of numerous industrial components. From dislocation movement to atomic diffusion, various processes can drive creep behavior [65, 67, 71-73]. A general equation representing the steady state creep rate controlled by any of the creep mechanisms stated as follows in the form of BMD equation (1),

$$\dot{\varepsilon} = A\left(\frac{DEb}{kT}\right)\left(\frac{b}{d}\right)^{p}\left(\frac{\sigma}{E}\right)^{n} \tag{1.1}$$

where $\dot{\varepsilon}$ is the steady state creep rate, D the diffusion coefficient that characterizes a particular creep mechanism, E the elastic modulus, b the Burger's vector, k the Boltzmann Constant, T the temperature, d the grain size, σ the applied shear stress, A the pre-factor, p the inverse grain size exponent and n the stress exponent. The parameters n, p, D and A vary depending on the underlying creep mechanism(s).

6.2.1. Nabarro-Herring creep

The Nabarro-Herring Creep, named after Frank Nabarro and Anthony Herring, is a diffusion-based mechanism for the creep of crystalline materials. Nabarro and Herring proposed the concept independently in the 1940s. Nabarro proposed a creep mechanism, in which lattice diffusion controls the dominant strain rate. Around the same time, Anthony Herring, an Australian-born physicist working in the United States, independently arrived at a similar concept [74].

In the N-H creep mechanism, atoms migrate through the crystal lattice from areas of high stress to areas of lower stress (Fig. 1.3). This atomic migration, or diffusion, results in plastic deformation over time, or creep. N-H creep is especially relevant in materials subjected to high temperatures and low stresses, and in materials with small grains, as the rate of creep is directly proportional to the grain size. Nabarro and Herring derived an equation of state for the deformation with N-H creep as the dominant mechanism, equation (1.2),

$$\dot{\varepsilon}_{NH} = 12\left(\frac{D_l E b}{kT}\right)\left(\frac{b}{d}\right)^2\left(\frac{\sigma}{E}\right)^1 \tag{1.2}$$

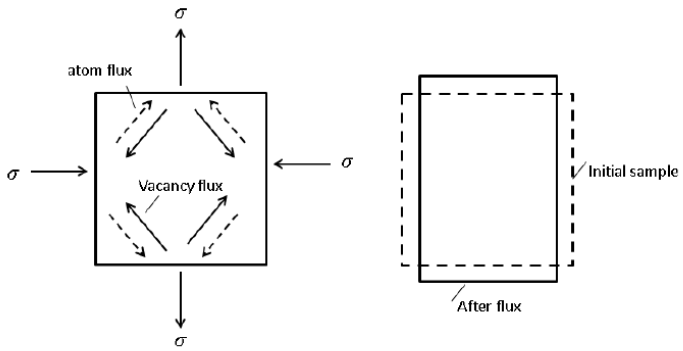

Figure 1.3. Schematic diagram depicting the process of N-H creep in single grain.

6.2.2. Coble creep

The Coble creep mechanism named after Robert L. Coble; an American material scientist renowned for his seminal work on the creep deformation of crystalline materials. Coble first proposed this mechanism in 1963 as a model for the creep of polycrystalline materials. In the Coble creep model, grain boundary diffusion determined the creep strain rate, as opposed to lattice diffusion, which governs the Nabarro-Herring creep mechanism. This means that atoms migrate along the grain boundaries under a stress gradient, leading to plastic deformation over time [9, 68].

Coble's work helped explain the observed creep behavior of fine-grained materials, especially ceramics and some metals, under low temperatures and low stresses. The rate of Coble creep is inversely proportional to the cube of the grain size (d), distinguishing it from Nabarro-Herring creep, which shows a d^{-2} dependence. Therefore, materials with smaller grain sizes are more prone to Coble creep. The equation of state for Coble creep derived by following a similar methodology as in N-H creep is,

$$\dot{\varepsilon}_C = A_C\left(\frac{D_g E b}{kT}\right)\left(\frac{b}{d}\right)^3\left(\frac{\sigma}{E}\right)^1 \tag{1.3}$$

where D_g is grain boundary diffusivity. The value of A_c was determined to be 148 by Coble, later modified to be ~50 by Dorn. As seen from equation (1.3), Coble creep exhibits a stress exponent of one like that of N-H creep. However, the activation energy for Coble creep is equivalent to that for the grain boundary diffusion. As a result, Coble creep becomes important at lower temperatures than N-H creep.

6.2.3. Harper-Dorn creep

Harper-Dorn creep is a mechanism of creep deformation named after its discoverers, James K. Harper, and John Dorn, who first observed it in the 1950s. This creep mechanism is unique because it occurs at relatively low stresses and high temperatures but does not show a strong

dependency on the grain size of the material, unlike the other well-established creep mechanisms like N-H creep and Coble creep [75].

Harper and Dorn observed this peculiar creep behavior while studying Al. They noticed that under certain conditions of low stress and elevated temperature, the strain rate was almost independent of the grain size and was proportional to the applied stress. This was contrary to N-H or Coble creep, where the strain rate was sensitive to the grain size. The mechanistic understanding behind Harper-Dorn creep is not as well-established as that of other creep mechanisms. Some theories propose that it may involve a high density of mobile dislocations within the grains, which enables deformation under low stresses.

6.2.4. Grain boundary sliding mechanism.

Grain boundary sliding (GBS) as a mechanism for creep deformation has been recognized for well over a century. The concept initially emerged in the late 19th century when scientists began to explore the internal structure of metals. They noted the polycrystalline nature of metals, composed of many small grains separated by interfaces known as grain boundaries [76].

In the early 20th century, Samuel E. Beilby, a British scientist, provided the first evidence of GBS in his experiments, which showed that metals subjected to high temperatures and pressures, the grains within them slide past each other. He noticed this phenomenon as part of his studies on the burnishing of metals. However, the broad recognition of GBS as a significant creep mechanism only came in the 1940s and 1950s. Research during this time began to highlight that under certain conditions (specifically, high temperatures and relatively low stresses); grain boundary sliding could contribute significantly to plastic deformation.

The study of GBS has helped scientists understand that the grain size influences the creep behavior of a material. When subjected to stress, grain boundaries can slide, causing the material

to deform. This is particularly noticeable when the grain sizes are small, and the temperatures are high. For certain materials, GBS is the primary creep deformation mechanism. The sliding could be concentrated at the boundary (pure GBS) or could occur at a narrow zone around the boundary (Zone GBS). Another classification of GBS is based on the mechanism by which the sliding proceeds during creep is sliding accommodated by diffusion of atoms along the boundary (Lifshitz GBS) and sliding carried out by glide and climb of dislocations (Rachinger GBS).

A well-known model is derived by Ashby and Verral [73] for the GBS accommodated through diffusion of atoms, according to which the sliding would result in grain switching thus producing strain in materials (Fig. 1.4). The constitutive equation has a stress exponent of one, which is like the diffusional creep mechanisms such as Coble creep and N-H creep. However, the key distinction relevant to the topological nature of the process is that unlike other diffusional creep mechanisms, grain boundary diffusion-controlled deformation does not result in any significant alteration in grain size with the increase in strain.

Numerous models have been put forward to elucidate (GBS) facilitated by the glide and climb of dislocations. Langdon's model for Rachinger GBS is one of the well-known examples [77]. This model presumes that GBS begins with the glide of dislocations at the grain boundary, a process obstructed by obstacles like grain boundary triple junctions, as depicted in (Fig. 1.5). Such a scenario triggers high stress concentrations at the triple junctions, thus further inducing lattice dislocations to glide through the grain until they encounter a barrier like a grain boundary or sub-grain boundary. As a result, the speed at which the leading lattice dislocations recover through the climb process controls the GBS rate. This mechanism of GBS is like that proposed earlier by Ball and Huchison. Based on this mechanism, a unified equation was derived for describing GBS in high temperature creep ($d>\lambda$) as well as superplastic conditions ($d<\lambda$), equation (1.4).

$$\dot{\varepsilon} = 2\left(\frac{D_{gb}Eb}{kT}\right)\left(\frac{b}{d}\right)^2\left(\frac{\sigma}{E}\right)^2 \tag{1.4}$$

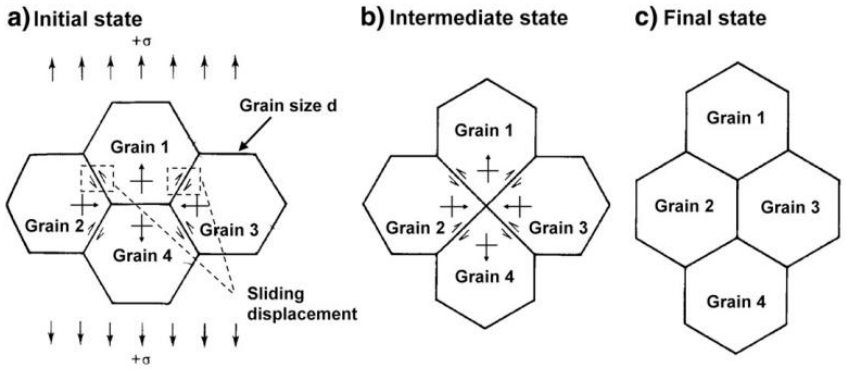

Figure 1.4. Schematic of a grain-switching event. Relative grain-boundary sliding produces a strain (c) without a change in grain shape (compared (a) with (c)). However, the intermediate step (b) of the process is associated with an increased grain-boundary area [77].

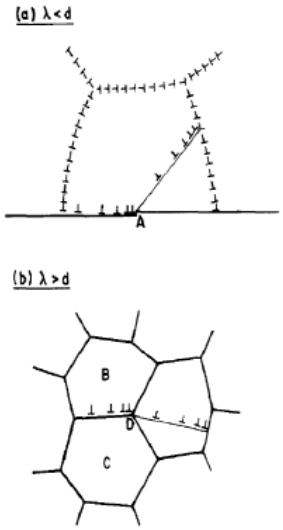

Figure 1.5. Rachinger sliding mechanism in materials with (a) $\lambda < d$ and (b) $\lambda > d$, where λ and d the sub-grain size and grain size [77].

6.2.5. Viscous-glide creep mechanism

Viscous glide creep [67], also sometimes referred to as dislocation-glide creep, emerged as a concept in the mid-20th century when scientists began to understand the role of dislocations in the deformation of crystalline materials. The development of electron microscopy in the 1930s and 1940s allowed for the direct observation of dislocations, giving rise to the field of dislocation theory, and helping us understand how dislocations interact with each other and the crystal lattice.

The concept of viscous glide creep [78] was refined and popularized in the 1950s and 1960s by the work of scientists like Michael E. Kassner [68] and others. It became a significant component in our understanding of creep deformation, especially in the context of lower-temperature deformation mechanisms. Viscous glide creep occurs when dislocations, move or 'glide' through the crystal lattice under an applied stress. This movement is resisted by a viscous drag force due to the interaction of the dislocations with the lattice and with other dislocations. The result is a time-dependent deformation, or creep, which continues as long as the stress is applied. The viscous glide creep is most significant at temperatures below about half the absolute melting temperature of the material. At higher temperatures, other creep mechanisms like dislocation climb or diffusional flow become more prominent.

Weertman [79, 80] first developed a model for the viscous-glide creep in which the velocity of dislocations was assumed to be linearly proportional to the stress acting on them. The creep rate equation based on Weertman model in the form of the BMD state equation is,

$$\frac{\dot{\varepsilon} \mathrm{kT}}{DEb} = 6\left(\frac{\sigma}{E}\right)^3 \tag{1.5}$$

In this model, Weertman [79, 80] does not detail the potential mechanisms that could be responsible for the viscous drag of dislocations. However, Poirier [72] provides a list of several mechanisms that could potentially slow down the glide velocity of dislocations. These include the

segregation of solute atoms at dislocation cores to alleviate their stress field, known as Cottrell's atmosphere [71], and the chemical interaction between solutes and the stacking fault ribbon of dislocations, which could reduce the overall stacking fault energy, referred to as the Suzuki effect [81]. Other possibilities are the disruption of short-range order due to the motion of dislocations, known as Fisher's mechanism [82], and local ordering of solute atoms in the stress field of dislocations, known as the Snoek mechanism [83].

According to the solute drag mechanism [84], solute atoms congregate at the dislocation core, effectively immobilizing the dislocations. This has been exemplified in certain alloy systems by observing the variation in creep rate with applied stress. At lower temperatures, if the applied stress exceeds the force needed to break the solute-dislocation bond, the dislocations are expected to move unhindered by the solute atoms. Yet at higher temperatures, solute atoms can diffuse through the lattice and re-lock the dislocations if their movement rate is slower than the diffusion rate of the solute atoms, provided the applied stress is low enough. This leads to a situation where dislocations drag solute atoms along during the glide process. However, with sufficient stress, this lock can be broken, facilitating a quicker glide process. Consequently, at higher stress levels, creep controlled by dislocation climb becomes the dominant rate-controlling factor, as evidenced in various systems.

6.2.6. Dislocation-climb creep mechanism

The dislocation-climb creep mechanism was first conceived in the mid-20th century, following the advent of dislocation theory in the 1930s and the development of transmission electron microscopy, which allowed for the direct observation of dislocations. The concept of dislocation climb was formulated by several scientists, most notably John E. Burke and David Turnbull [85].

They postulated that dislocation climb could provide a means for plastic deformation in crystalline materials at elevated temperatures where vacancies become mobile. Their hypothesis was eventually supported by numerous experimental observations and has become a cornerstone of high-temperature deformation theory. Scientifically, dislocation climb is a mechanism of plastic deformation in crystals. It occurs when an edge dislocation moves perpendicular to its slip plane under the influence of an applied stress. This motion, unlike the case of dislocation glide, is not constrained by the crystal lattice's slip systems [79]. Dislocation climb is facilitated by the diffusion of vacancies in the crystal lattice. At elevated temperatures, vacancies become mobile and can migrate to the region of a dislocation. When a vacancy reaches an edge dislocation, it can be absorbed into the extra half-plane of atoms that forms the dislocation, effectively allowing the dislocation to move or 'climb' to an adjacent plane.

In terms of its contribution to creep, dislocation climb allows materials to deform at lower stress levels than would be possible with dislocation glide alone. The rate of this deformation is dependent on the rate of vacancy diffusion, which in turn is highly temperature dependent. As a result, dislocation climb is generally more prominent at high temperatures, typically above about half the absolute melting temperature of the material [67].

Weertman [80] devised a model to establish a constitutive equation, encapsulating creep rates in materials subjected to deformation controlled by dislocation climb. This model, known as the pillbox model, assumes that there are M number of operative dislocation sources per unit volume. The generated dislocations from these sources are posited to glide for a distance L before climbing up or down to annihilate with dislocations approaching on parallel planes, with the climbing height being denoted as h. As illustrated in (Fig. 1.6), each dislocation source continually generates a set number of dislocation loops on the glide plane. Once the foremost dislocation is

annihilated, another dislocation is discharged from the source. Based on these initial conditions, Weertman derived the following relation for the creep rate:

$$\dot{\varepsilon} = \alpha \left(\frac{D_l}{b^{3.5} M^{0.5}}\right) \left(\frac{\sigma}{G}\right)^{4.5} \left(\frac{G\Omega}{kT}\right) \tag{1.6}$$

where G is the shear modulus, Ω is the atomic volume, is a constant whose values are in the range $0.015 < \alpha < 0.33$.

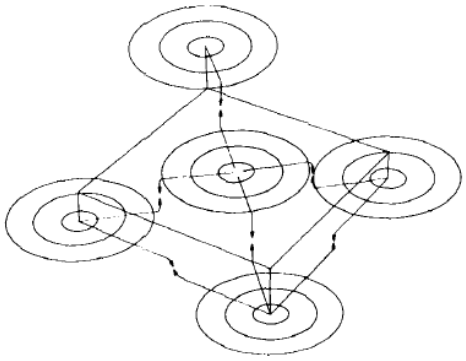

Figure 1.6. Creation and annihilation of dislocation loops assumed in the Pillbox model [80].

7. Creep in precipitation-hardened alloys

The change in solid solubility with temperature in alloys can result in the formation of fine second phase particles of varying types and sizes within the matrix, often referred to as precipitates. These precipitates act as effective barriers to the movement of dislocations even at elevated temperatures, subsequently enhancing the creep properties of the material. The characteristics of these particles, including their volume fraction, size, shape, crystal structure, and coherency, are critical in determining the extent of strength increase in the material [68].

At low temperatures, dislocations bypass the particles encountered within its glide plane either by shearing particles or by Orowan looping between particles. However, during high-temperature

creep deformation, diffusional mass transport becomes significant, and the process of dislocations bypassing the particles through climbing becomes crucial in precipitation-strengthened alloys. The creep characteristics for these alloys are defined by high stress exponents (>7), even when the stresses and temperature are within the power law regime, substantially higher activation energy for creep compared to self-diffusion, and a microstructure marked by interactions between dislocations and precipitates [9].

The influence of particle strengthening on creep is depicted in (Fig. 1.7), where the modulus compensated stress is plotted against the normalized steady-state creep-rate. To justify the high values of apparent stress exponent or apparent activation energy for creep based on currently known creep mechanisms, the concept of threshold stress or back stress has been frequently invoked in the context of precipitation-strengthened alloys [86]. The threshold stress is linked with the particle bypass mechanism. Hence, the steady-state or minimum creep rate is articulated in terms of the effective stress, as opposed to the applied stress. Here, the effective stress represents the difference between the applied and the threshold stresses. Provided that the activation energy for self-diffusion is in play during creep, the BMD equation (equation (7)), used for dislocation creep, can be adjusted to express the creep rate in precipitation-strengthened alloys as follows:

$$\dot{\varepsilon} = \mathrm{A}_c \left(\frac{D_O E b}{kT}\right) exp\left(\frac{-Q}{RT}\right) \left(\frac{\sigma_a - \sigma_{th}}{E}\right)^n \tag{1.7}$$

In this context, the values for the stress exponent, *n*, fall within the range of power-law creep. This suggests that the creep process in precipitation-strengthened alloys is closely tied to those in single phase systems. Equation (7) has been frequently used to find the operating creep mechanism(s) in precipitation-hardened alloys. The values for the threshold stresses are approximated using the linear extrapolation method. The selected value for the true stress

exponent, *n*, must both satisfy the highest correlation coefficient of the linear fit and correspond with the activation energy for a specific creep mechanism [87, 88].

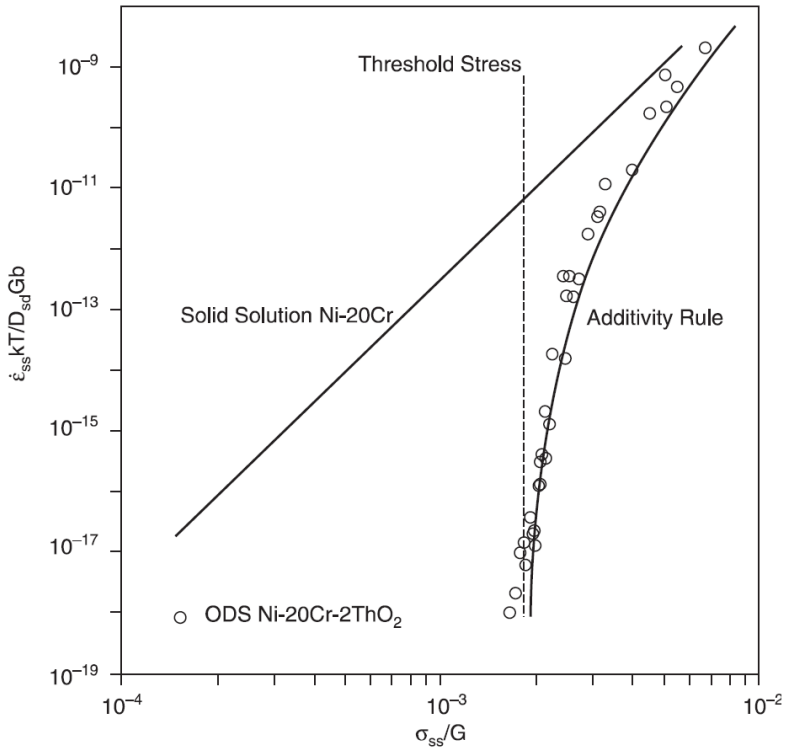

Figure 1.7. The normalized steady-state creep-rate versus modulus compensated stress showing the effect of particle strengthening on creep rate [68].

7.1. Theoretical approaches to the threshold stress and associated mechanisms

The threshold stress emerges from the stress exerted on the dislocations by the precipitates during glide and climb processes. Multiple mechanisms have been proposed to theoretically calculate the threshold stress, factoring in the volume fraction, size, and type of precipitates, as well as the nature of interaction between dislocations and precipitates [68]. Fig. 1.8 portrays various mechanisms by which a dislocation can bypass second-phase particles during creep deformation [89]. The corresponding formulae for the threshold stress for different dislocation bypassing mechanisms are summarized in Table 1.1. In all models, the threshold stress values are found to be inversely proportional to the mean inter-particle spacing.

The athermal process of dislocation bypassing particles by forming loops around them has been reported to occur during creep deformation. However, the threshold stress is usually found to be lower than the Orowan stress required for bowing around precipitates, and the Orowan mechanism seems to be operative at high stresses. Ashby developed a model based on the Orowan mechanism but factoring in the mutual interaction between the bowed-out segments, which reduces the magnitude of the Orowan stress, typically by a factor between 0.5 and 0.7 [68].

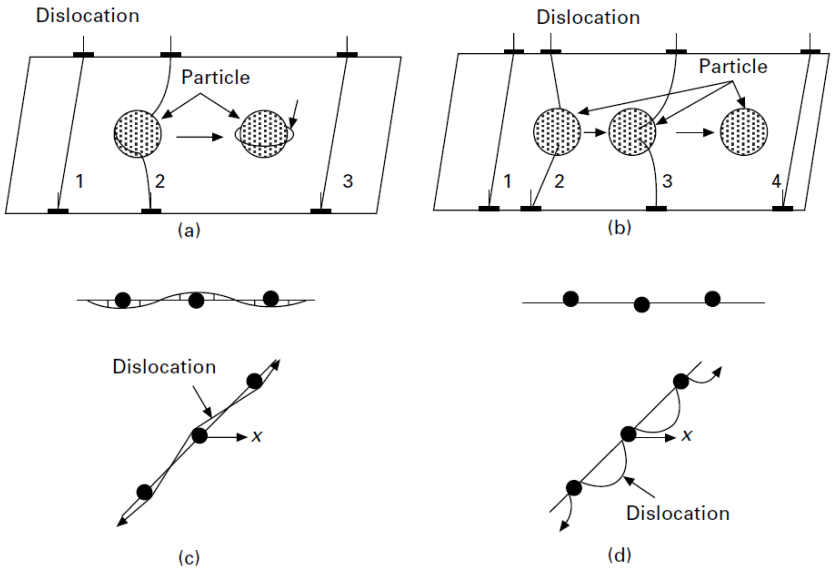

Figure 1.8. Schematic of different mechanisms by which dislocation can surmount second phased particles during creep deformation. (a) Orowan mechanisms, (b) Srolovitz's mechanism, (c) general climb mechanism and (d) local climb mechanism [89].

Furthermore, the process of dislocations bypassing particles by climbing over them has later been considered, which involves diffusional mass transport. This mechanism demands a detailed analysis of the nature of the interaction between dislocations and precipitates. The climb of dislocations around a group of precipitates can be categorized into two broad terms: namely, local climb and general climb. In local climb, only the segment of the dislocation in the particle-matrix interface climbs while the dislocation segments between particles remain on their slip plane.

The threshold stress arises from the increase in the dislocation segment due to climb within the particle-matrix interface, which compensates for this increment in dislocation length. For general climb, the entire dislocation climbs out of its glide plane, which requires a smaller increase in the total length compared to that of the local climb [9, 68].

Srolovitz et al. [90] developed a model based on the attractive interaction at the interface between the particle and dislocation. In this model, a relaxation of the dislocation core that leads to the pinning of dislocation gives rise to the threshold stress for creep. Local climb of the dislocation over a precipitate is more dominant than the general climb in Srolovitz's mechanism. Arzt and Wilkinson [91] also contemplated the attractive interaction between dislocations and spherical particles; however, in their model, the threshold stress arises from the dislocation's detachment from the particle after climbing, irrespective of whether the type of climb is local or general.

Unlike other models, Arzt and Wilkinson [91] demonstrated that the particle size is not crucial for determining the threshold stress while the mean inter-particle spacing is important. Furthermore, Evans and Knowles [92] offered a threshold stress based on the increasing length of dislocation, which is weakly dependent on the applied stress while being strongly dependent on the ratio of the particle size to mean inter-particle spacing. Mishra et al. [93] have also proposed a model for the threshold stress based on the attractive dislocation-particle interaction where the local climb process involves the dissociation of lattice dislocations into interfacial dislocations when they enter the matrix-particle interface.

It is worth noting that the threshold stress values evaluated from the aforementioned models are not fully consistent with the threshold stresses determined experimentally, suggesting a further understanding of creep in precipitation-hardened alloys is required. Additionally, the models have

only considered the particles within grains; however, the presence of second phases along grain boundaries may also occur in precipitation-hardened alloys and inhibit the diffusional creep and GBS. The precipitates at grain boundaries may affect the ease of grain boundaries as vacancy sources and sinks, potentially resulting in an additional back stress [94].

Table 1.1. Theoretical models for the threshold stress in precipitation-hardened alloys.

σ_{Th}(MPa)	Model	Ref.
$\frac{0.8MGb}{\lambda}$	Orowan bowing around precipitates	[89]
$\frac{MGb}{2\pi(1-\nu)\lambda}(\ln(2)+\ln(\frac{r}{r_o}))$	Ashby's model	[95]
$\frac{8\Gamma r}{3\lambda b}\sqrt{\{r^2+[\frac{4\Gamma}{\sigma_a b}sin^{-1}(\frac{\sigma_a b\lambda}{8\Gamma})}$	Evans and Knowles	[92]
$\frac{MGb}{\lambda}\sqrt{1-k^2}$	Detachment mechanism	[91]
$MGC\frac{B}{\lambda}\exp(B\frac{r}{\lambda})$	Dislocation dissociation	[93]
$\frac{MGb}{2\pi(1-\nu)\lambda}[\frac{\pi^2}{12}+\ln\left(\frac{r}{r_o}\right)]$	Srolovitz's mechanism	[90]

G shear modulus, $M\sim3$ (Taylor factor), $\nu\sim0.3$ (Poisson's ratio), r average radius of the particles, $r_o\sim b$ (dislocation core radius), λ inter-particle spacing, Γ dislocation line energy, $C\sim0.002$ and $B\sim20$ constant for Mishra model and $k\sim0.3$ constant for Arzt model.

8. Motivation

The necessity to design efficient and sustainable energy systems has never been more critical. As global power demand surges, alternative energy sources, such as nuclear energy, have proven to be an effective solution for tackling growing energy needs while simultaneously minimizing environmental impact. However, the safety and performance of nuclear reactors are inextricably linked to the materials used in their construction, especially those exposed to extreme operating conditions. The two novel alloys, APMT and 14YWT-NFA1, considered in this study offer promising characteristics for such challenging applications, yet an in-depth understanding of their high-temperature mechanical properties is still lacking.

APMT alloy emerges as a potential cladding material for Light Water Reactors (LWRs). This proposal is based on its ability to endure the rigors of LWR operations, particularly under accident scenarios. The resilience of cladding materials is a critical aspect of reactor safety since cladding prevents the release of radioactive fission products into the cooling medium. However, the material's response under high-temperature conditions - a common attribute of accident situations - is still inadequately understood. Therefore, a detailed study of the APMT alloy's high-temperature mechanical properties, particularly its creep behavior, is crucial.

Similarly, the 14YWT-NFA1 alloy is a leading candidate for usage in future fusion reactors. These cutting-edge energy systems will operate under unprecedentedly high temperatures and intense neutron radiation, posing a significant challenge for materials selection. Fusion reactors necessitate materials that exhibit superior mechanical properties at high temperatures, withstanding both thermal and irradiation-induced stresses. In this context, a comprehensive understanding of the high-temperature creep properties of the 14YWT-NFA1 alloy is paramount,

as this characteristic can significantly impact the material's operational longevity and the overall reactor's safety and efficiency.

Moreover, despite the different operational environments of light water and fusion reactors, common material property trends can inform broader themes in high-temperature nuclear materials science. The study of these two alloys will illuminate the underlying mechanisms driving their mechanical performance, contributing to the ongoing development of advanced materials for nuclear applications.

The intention of this study, therefore, is to fill the knowledge gaps in our understanding of the high-temperature mechanical properties of APMT and 14YWT-NFA1 alloys', with an emphasis on creep behavior. By doing so, the findings will not only enhance our comprehension of these alloys but also establish a foundation for their successful implementation in next-generation nuclear reactors, thus paving the way for safer and more efficient nuclear power production.

2. Materials and Experimental Methods

Various experimental tools were employed to achieve the objectives of this research. Specifically, creep testing, transmission electron microscopy, scanning electron microscopy and electron backscatter diffraction are used to characterize the creep behavior and microstructures of two different types of alloys: high Cr-containing alloys (APMT) and nano-structured ferritic alloys (14YWT-NFA1). This chapter offers detailed information about the alloys used in this study, as well as the procedures related to both mechanical and characterization testing.

1. Materials

1.1. Advanced Powder Metallurgy Tubing (APMT)

The tested APMT was received in the form of a 12 mm thick hot rolled plate of high Cr-containing FeCrAl alloy (APMT), provided by the Kanthal company. Rectangular cross-section specimens were machined using Wire EDM (Electrical Discharge Machining). These rectangular flat specimens feature a 20 mm gauge section with a cross-section of 2 mm×3.94 mm and holes in the two grip sections to ensure precise alignment during testing (Fig. 2.1). The composition of APMT alloy can be found in Table 2.1.

Table 2.1.Elemental composition (wt.%) of APMT alloy used in this work.

Elements	Fe	Cr	Al	Mo	C	Si	Mn	Y	Zr
wt. %	Balance	21.250	4.860	2.990	0.036	0.34	0.18	0.17	0.11

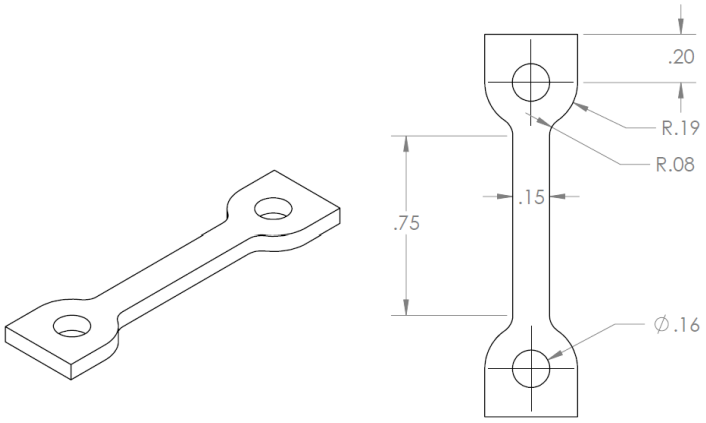

Figure 2.1. APMT creep specimen geometry and dimensions used in this study.

1.2. Nano-Structured Ferritic Alloy (14YWT-NFA1)

It is important to note that there exist nearly 12 distinct 14YWT ingots, each exhibiting varying performance levels depending on the fabrication parameters and conditions. The specific ingot utilized in this research is referred to as 14YWT-NFA1. The 14YWT-NFA1 utilized in this research was fabricated via mechanical alloying (MA). This method involved adding Y directly to the melt prior to gas atomization and maintaining control over the O levels in the powders. Pre-alloyed powder was crafted through Argon (Ar) gas atomization. These pre-alloyed powders were then ball milled for 40 hours in an Ar gas environment. The ball-milled powder was then employed in the production of two extrusions of the nanostructured ferritic alloy. Approximately 2.25 kg of ball milled powder was placed into two cans, which were then degassed at 400ºC and subsequently sealed. The cans were heated at 850ºC for 2 hours and extruded through a 63.5 mm x 30.5 mm rectangular die, resulting in extruded bars. These bars were then annealed at 1000ºC for 1 hour in high vacuum. Test specimens were machined in the form of rectangular cross-section using Wire EDM (Electrical Discharge Machining). These rectangular flat specimens feature a 10 mm gauge section with a cross-section of 1.25 mm×3 mm and two alignment holes in the gripping section to

ensure precise alignment during testing (Fig. 2.2). The composition of the 14YWT-NFA1 alloy can be found in Table 2.2.

Table 2.2. Elemental composition (wt.%) of 14YWT-NFA1 alloy used in this work.

Elements	Fe	Cr	W	Y	Ti
wt. %	Balance	14	3	0.2	0.4

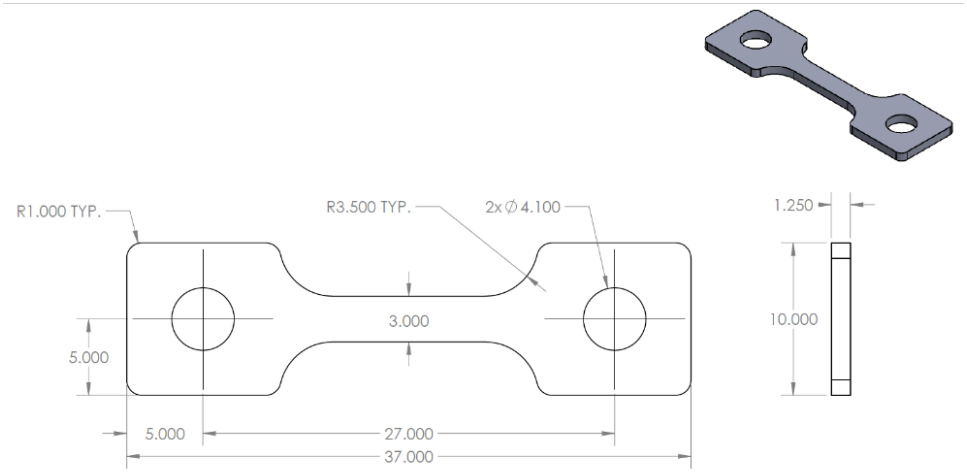

Figure 2.2. 14YWT-NFA1 creep specimen geometry and dimensions in inch used in this study.

2. Microstructural Characterization

The microstructure characterization was carried out before and after the creep tests. Initially, specimens were extracted from the as-received samples to examine the original microstructure. Specimens were cut using diamond saw along the transverse direction. The cross-section cuts were mounted on a stub with epoxy resin for grinding and polishing. The specimens were then ground using SiC papers of increasing fineness, up to 1200 grit, to eliminate surface irregularities or damage. Polishing continued with 0.1 µm alumina-based suspensions until a mirror-like surface was achieved. The specimens were etched with Nital etchant (5% nitric acid in ethanol by volume)

for one minute to expose the FeCrAl alloys' microstructure, followed by thorough rinsing in an ultrasonic bath. The FEI Verios 460L field-emission scanning electron microscope (FESEM) equipped with an Electron Back Scattering (EBSD) detector was employed to analyze grain size distribution, grain boundaries, and Kernel Average Misorientation (KAM). Furthermore, the ThermoFisher Quanta 3D FEG/SEM-FIB (Scanning Electron Microscope - Focused Ion Beam) was utilized to prepare TEM (Transmission Electron Microscope) samples. TEM characterization was performed using the Talos F200X G2, operating at 200 kV and equipped with an Energy Dispersive Spectrometry detector, to investigate the microstructure, dislocation activity, and secondary phases. X-ray diffraction (XRD) analysis was performed to investigate the crystallographic phases present in the material and to determine the lattice constants. The XRD measurements were carried out using a PANalytical Empyrean X-ray diffractometer equipped with a Cu Kα radiation source (wavelength = 1.5406 Å) at a voltage of 40 kV and a current of 30 mA.

3. Creep Testing

Uniaxial creep experiments were performed employing a typical creep tester following ASTM E8 and ASTM E139 testing standards (Fig. 2.3). A 20:1 lever arm was utilized to administer the load. The test frame featured a triple-zone furnace with a temperature control device, thereby enabling individual temperature regulation across the three zones. Two k-type thermocouples, attached to the gage section of the specimens, were used to capture temperature readings, ensuring temperature stability of ±1 ºC for the entire duration of the experiment. The specimen's extension was measured with a Linear Variable Differential Transformer (LVDT), which was calibrated before each experiment. The LVDT, fastened securely onto the specimen using a high-temperature extensometer and specially fabricated grips for rectangular specimens, assured accurate measurements. Pre-test preparation involved mechanically polishing the specimens with 1200 grit

to remove the soft recast layer caused by the wire EDM machining. The specimens were then given a 30-minute soak in air environment at the targeted temperature, ensuring a uniform temperature distribution across the specimen. The load application process was incremental, commencing from a low-stress level until it reached the steady-state region, validated through strain rate versus time analysis. The load was then increased to the next pre-set stress level, repeating this process in a stepwise manner. At the completion of the test, the load was withdrawn, the temperature control unit was turned off, and the furnace was opened and cooled using forced air. This process aimed to maintain the microstructure in its tested state.

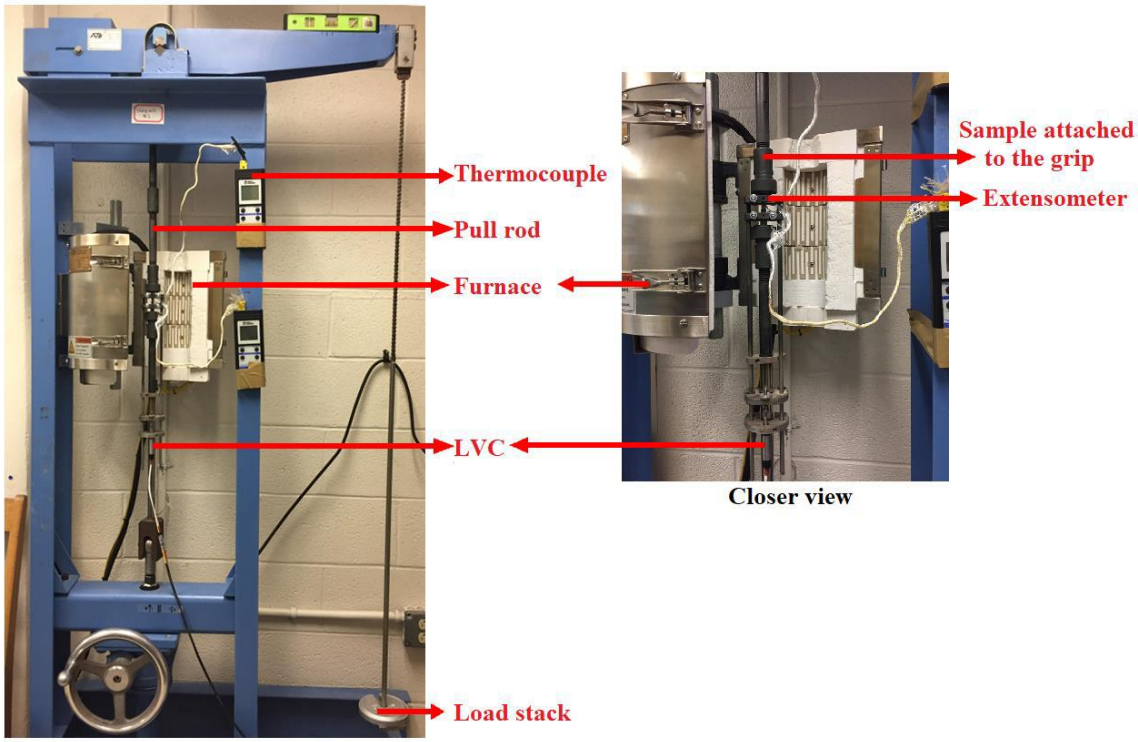

Figure 2.3. Experimental setup showing lever-arm creep tester components (left) and a closer view (right) showing the sample, extensometer, and gripping system.

3. Simulation Methods: Molecular Dynamics

1. Introduction

Molecular dynamics (MD) simulations have become a crucial tool in many fields of science and engineering. They are especially significant in materials development, as they provide detailed insight into atomic and molecular interactions, enabling us to design and optimize new materials [96]. The primary concept of MD simulations is the numerical integration of Newton's equations of motion for a system of interacting particles. By accounting for the forces between atoms and molecules, we can predict how a system will evolve over time under certain conditions. This approach allows us to model and simulate many dynamic behaviors and properties, from the conformational changes of biological macromolecules to the structural transformations in solid-state materials [97].

In the field of material development, MD simulations are indispensable for understanding the microscopic structure and behavior of materials. They can offer insights into the material's properties, like strength, ductility, or how it might respond to external forces or conditions such as temperature changes or mechanical stress. They can also help us identify the mechanisms that govern phase transformations, predict new structures or phases, or even design new materials with tailor-made properties. The simulation of these behaviors helps scientists and engineers reduce the trial-and-error of laboratory experiments, and thereby accelerate the process of materials design and discovery [98].

The typical timescales in MD simulations are in the range of picoseconds to nanoseconds, which can model processes such as molecular vibrations (Fig. 3.1). The length scales typically encompass tens to millions of atoms or molecules, depending on the computational resources available [99].

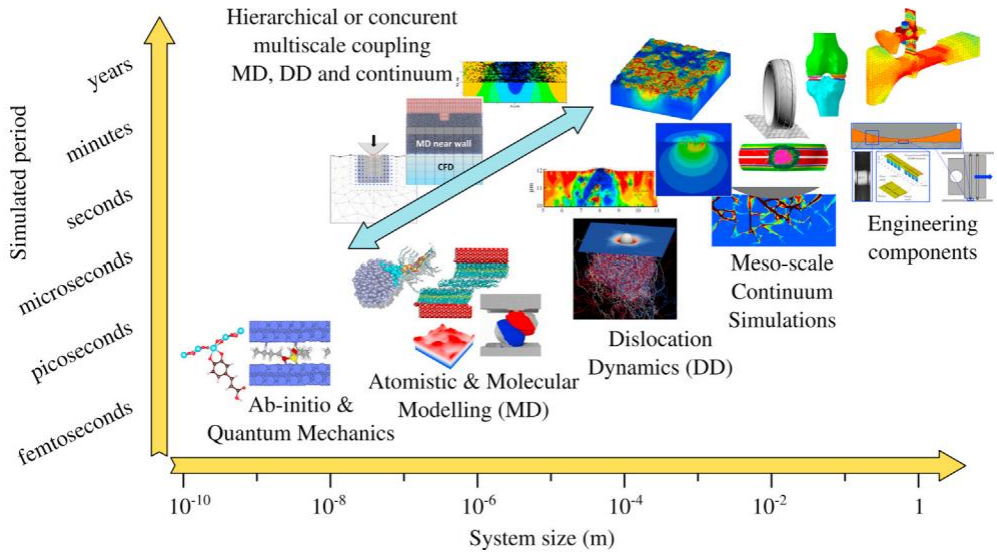

Figure 3.1. A time-versus. length-scales map of models developed in tribology highlighting the intrinsic link between multiscale/physics that needs to be captured to provide predictive tools for engineering applications [99].

2. Classical Mechanics

Classical mechanics is one of the pillars of physics, describing the motion of macroscopic objects from projectiles to parts of machinery, as well as astronomical objects like spacecraft, planets, stars, and galaxies. Underpinning this fundamental field are Newton's three laws of motion, which are simple yet profound equations that accurately predict the behavior of moving objects under a wide range of conditions [100]. Classical mechanics makes a critical assumption that the behavior of objects can be predicted exactly if their initial states and the forces acting on them are known. This assumption, along with Newton's laws, makes it possible to mathematically model the movement and interactions of objects over time.

In the context of molecular dynamics (MD), classical mechanics takes center stage. MD simulations essentially use the principles of classical mechanics to model the behavior of atoms and molecules. Each atom in a system is considered a particle, and Newton's laws are applied to this particle to predict its movement based on the forces it experiences from other nearby atoms. While quantum mechanics more accurately describes the behavior of atoms and molecules, the complexity and computational intensity of quantum calculations make it impractical for systems of more than a few particles. Classical mechanics, in contrast, provides a good enough approximation for many purposes and allows us to simulate systems with billions of atoms, a necessity for studying complex biological systems or materials science [101].Hence, the simplicity and computational efficiency of classical mechanics become essential to the world of MD simulations, enabling us to computationally investigate the dynamic behavior of complex molecular systems over time. Classical mechanics, therefore, serves as the theoretical cornerstone that makes MD simulations possible and practical.

3. Statistical Mechanics

At its core, statistical mechanics provides a bridge between the microscopic behavior of individual atoms and molecules and the macroscopic properties observed in real-world materials. In an MD simulation, statistical mechanics is employed to calculate macroscopic quantities, such as pressure, or temperature from the microscopic states of the system. These microscopic states are represented by the positions and velocities of all the atoms, which are evolved over time according to Newton's equations of motion [100, 102].

By repeatedly sampling these microscopic states, an MD simulation generates an ensemble of states that corresponds to a particular set of macroscopic conditions, such as those defined by the NVE, NVT, or NPT ensembles discussed later in this section (Fig. 3.2). From this ensemble,

averages of various properties can be calculated to give a statistically meaningful description of the system's behavior. Therefore, statistical mechanics is an essential tool in the analysis and interpretation of MD simulations, grounding the microscopic dynamics in macroscopic observables [103, 104].

The selection of appropriate thermodynamic ensembles, which maintain constant sets of physical variables, is crucial for emulating specific experimental conditions. Among the commonly utilized ensembles, the Microcanonical or NVE ensemble, which maintains constant number of particles (N), volume (V), and energy (E), thereby replicating an isolated system. Alternatively, there's the Canonical or NVT ensemble, which keeps the number of particles (N), volume (V), and temperature (T) constant. This ensemble is designed to simulate a system in thermal equilibrium with its surroundings at a fixed temperature.

Finally, the Isothermal-Isobaric or NPT ensemble is another common choice, in which the number of particles (N), pressure (P), and temperature (T) are held constant. This ensemble is frequently used to mirror real-world experimental conditions, as it represents a system in contact with a heat bath at a constant temperature and under a constant external pressure. The choice among these ensembles depends on the specifics of the system under study and the experimental conditions to be simulated.

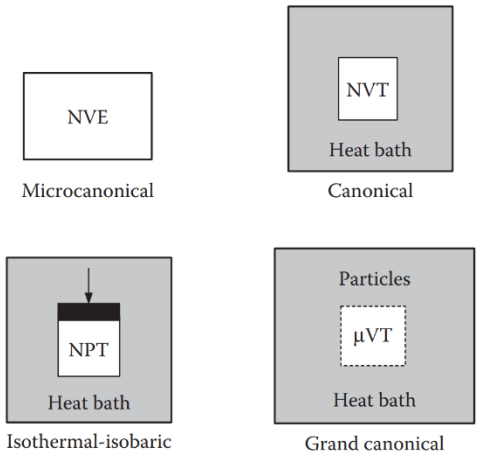

Figure 3.2. Schematics of four ensembles adopted in MD [100].

4. Interatomic Potential

In the world of Molecular Dynamics (MD), the trajectory of every atom hinges upon the forces it experiences due to the presence of other atoms. The central component that governs these interactions is the interatomic potential, also known as the potential energy function. The accurate depiction of interatomic potentials is crucial in MD simulations as they essentially dictate how atoms interact with each other, influencing everything from basic atom-atom collisions to the formation of complex structures [100, 105]. At the heart of interatomic potential lies the understanding that atoms tend to arrange themselves to minimize their potential energy. Interatomic potential describes the potential energy of a system of atoms as a function of their positions. The force between any two atoms is then determined by the gradient of this potential energy with respect to the atomic positions.

Interatomic potential plays a pivotal role in MD simulations. They inform the forces experienced by atoms, which are then used to solve Newton's equations of motion. By updating these forces at each step, the simulation models how the system evolves over time. The choice of potential can significantly influence the results of an MD simulation. Therefore, it is vital to use a

potential that is appropriate for the system and conditions under study. There's always a trade-off between accuracy and computational cost, and the choice of the potential often depends on the specific requirements of the simulation.

Interatomic potential comes in a variety of forms. The Lennard-Jones potential is a simple and widely used model. The Embedded Atom Method, on the other hand, is specifically crafted for metallic systems. The Morse potential allows for independent adjustment of potential well parameters, while the Buckingham potential is often used for ionic materials. Stillinger-Weber and Tersoff potentials consider more complex many-body interactions. Each potential has been developed to balance computational efficiency and accuracy for specific types of materials and conditions, thus influencing the outcomes of molecular dynamics simulations.

4.1. Embedded atom method potentials

The Embedded Atom Method (EAM) potential is a unique interatomic potential that has proven to be particularly effective for simulations of metallic systems. Unlike simpler potentials, the EAM potential accounts for the electronic structure of metals and the way in which an atom's behavior is influenced by the electron density from its neighboring atoms [105]. In the EAM model, the total energy of a system is composed of two parts: a pairwise interaction terms like those found in simpler potentials, and an 'embedding' term that represents the energy cost of placing an atom into the electron cloud produced by its neighbors. This extra degree of complexity allows the EAM potential to capture key properties of metals more accurately than other potentials [106-108].

$$U_{EAM} = \sum U(r) + \sum F(\rho)$$

where $F(\rho)$ is the embedding energy function and $U(r)$ is the pair potential function.

5. Solutions for Newton’s equations of motion

Solving Newton's equations of motion is a fundamental step in molecular dynamics (MD) simulations. This process facilitates the prediction of the future positions and velocities of atoms based on the forces acting upon them, which are calculated from the chosen interatomic potential. The solutions to these equations enable the tracking of the temporal evolution of a system at the atomic level. Although various algorithms exist for numerically solving Newton's equations, they all share the common goal of providing accurate and stable predictions of atomic trajectories over the simulation timescale. These solutions underpin our understanding of the dynamic behaviors and interactions within a system, thereby making them a cornerstone of MD simulations [97, 101, 102, 109].

5.1. Verlet Algorithm

The Verlet algorithm is a widely used method in molecular dynamics (MD) simulations for numerically integrating Newton's equations of motion. It provides an efficient and accurate means to predict the future positions of particles based on their current positions, velocities, and the forces acting upon them. The strength of the Verlet algorithm lies in its simplicity and stability. It uses information about an atom's current and previous positions, and the forces acting upon it, to calculate the atom's position at the next time step. This algorithm stands out due to its conservation of energy over long simulation times, which is crucial for MD simulations. However, one drawback is that the Verlet algorithm does not directly provide velocities, which are often required for calculating kinetic energy or temperature. These quantities can be computed from position data, but this adds an extra computational step.

5.2. Velocity Verlet Algorithm

Building on the foundations of the original Verlet algorithm, the Velocity Verlet algorithm emerged as an extension that elegantly resolves the lack of direct velocity calculation in the original method. Like its predecessor, Velocity Verlet provides a numerically stable and efficient solution to Newton's equations of motion in molecular dynamics (MD) simulations. The Velocity Verlet algorithm still calculates new positions based on current positions and forces, but it also explicitly calculates velocities. This algorithm executes this in a two-step process. The first step predicts the positions and half of the velocities, and the second step completes the velocity calculations after the force evaluation. By including the velocity term explicitly, the Velocity Verlet algorithm makes calculating kinetic energy and temperature more straightforward, enhancing its utility in MD simulations. Therefore, it not only retains the energy conservation benefits of the original Verlet method but also adds direct velocity computation, making it a highly advantageous tool for MD simulations.

5.3. Predictor-Corrector Algorithm

This method offers an improvement on the traditional Verlet and Velocity Verlet algorithms, by taking an initial guess (or 'prediction') at a system's future state, and then refining this guess with a 'correction' step. The Predictor-Corrector approach first uses the system's current state to predict the positions and velocities at the next time step. It then computes the forces acting on the atoms at this predicted state. These newly calculated forces are used to correct the initially predicted positions and velocities, providing a more accurate representation of the system's future state.

This algorithm has the advantage of being highly stable and accurate over long simulation times, like the Verlet and Velocity-Verlet methods. However, it also incorporates an iterative

refinement process that can improve the precision of the simulation, especially when the forces acting on the atoms change rapidly. As such, the Predictor-Corrector method offers another valuable tool in the toolkit of MD simulations, providing a sophisticated balance of stability, accuracy, and refinement.

6. Simulations

A typical MD simulation commences with the system initialization, where the initial positions and velocities of all atoms are determined, often in accordance with a Maxwell-Boltzmann distribution corresponding to a given temperature. Subsequently, a suitable interatomic potential, such as the Lennard-Jones, Embedded Atom Method, or others, is selected to govern the interactions between the atoms. Following these initial setup steps, the next phase involves using one of the numerical integration algorithms we discussed, such as the Verlet, Velocity Verlet, or Predictor-Corrector algorithms. These methods are employed to solve Newton's equations of motion, thereby advancing the system from its current state to the next by calculating the future positions and velocities of the atoms.

Once the system is advanced, the forces on each atom are recalculated based on the updated positions, using the previously chosen interatomic potential. This process is repeated for many iterations, or 'time steps', and the atomic positions and velocities are recorded at regular intervals. Lastly, the generated data is analyzed to determine the properties of interest, such as diffusion coefficients, structural properties, or reaction rates. The repeated iteration of these steps allows the system to evolve over time and enables the simulation to capture the dynamic behavior of atoms and molecules.

6.1. Periodic Boundary Conditions

The concept of Periodic Boundary Conditions (PBC) is another crucial aspect of Molecular Dynamics (MD) simulations, fitting neatly into the scheme we've discussed so far. PBC are used to mimic an infinite system while only simulating a small, representative part of it, known as a unit cell [100]. In practice, this means that when a particle crosses one boundary of the unit cell, it reenters from the opposite boundary, giving the illusion of an endless, repeating system. This technique is particularly useful for studying bulk properties of materials, as it minimizes edge effects that would otherwise dominate in small systems. Once the positions and velocities of atoms are updated using the selected interatomic potential and integration algorithm, the implementation of PBC ensures that the system remains effectively constant in size. This allows for the continuous and seamless progression of the MD simulation, providing more representative and realistic results of the infinite system under study.

4. Uniaxial Creep Behavior of High Cr-Containing, Dispersion-Strengthened APMT Alloy

1. Introduction

This chapter aims to provide a study of the creep behavior of APMT under stresses and temperatures relevant to the accident-tolerant fuel requirements.

2. Experimental Results

2.1. Microstructural Characterization of the As-Received Material

The primary phase in the as-received specimens is ferritic phase, which consists of fine, randomly oriented, and elongated grains. The grain size ranges from 1 to 20 μm, with an average grain size of approximately 4 μm. Some of the ferritic grain boundaries are decorated by pre-existing fine precipitates (Fig. 4.1). Fig. 4.2 shows the TEM-EDS elemental maps revealing that these precipitates were (Cr, Mo)-rich. These particles were identified using TEM diffraction pattern to be $M_{23}C_6$ carbides with face center cubic structure and 0.106 nm lattice constant, where M stands for metals (Cr, Mo). Fig. 4.3 containing Bright field TEM image at intermediate magnification clearly shows high dislocation density. However, no sign of retained strain was found from the X-ray diffraction analysis.

2.1. Uniaxial Creep Properties

The uniaxial creep results of APMT alloys tested at four different temperatures (575°C, 600°C, 625°C, and 650°C) and stress ranges from 50 MPa to 320 MPa exhibited different behaviors depending on the applied temperature and stress levels. A typical creep curve for an APMT specimen tested at 650°C and 50 MPa is shown in (Fig. 4.4). The creep curve starts with a

primary creep region characterized by an exponential-like function with a decreasing slope with time due to dislocation hardening.

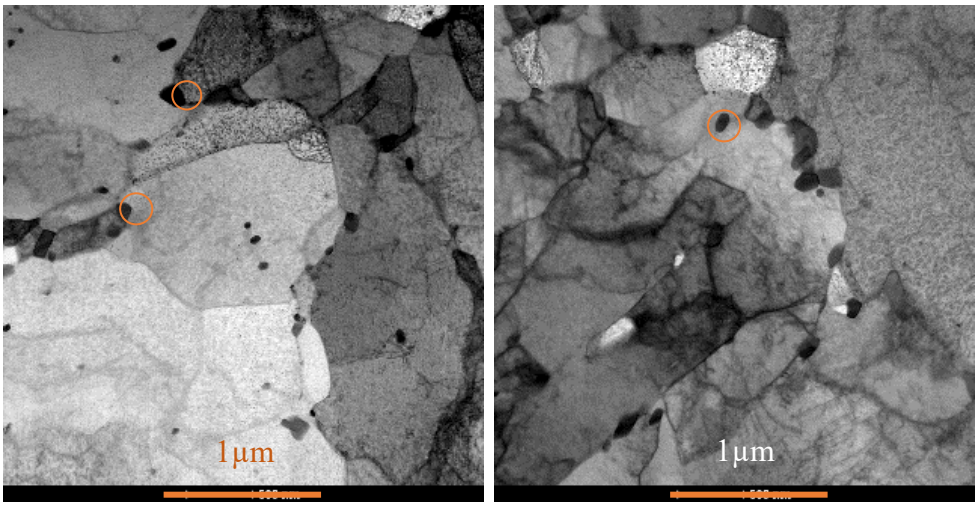

Figure 4.1. BF-TEM images of APMT revealing the grain structure and precipitate-rich grain boundaries at two different locations. Circles enclose some of the grain boundary precipitates.

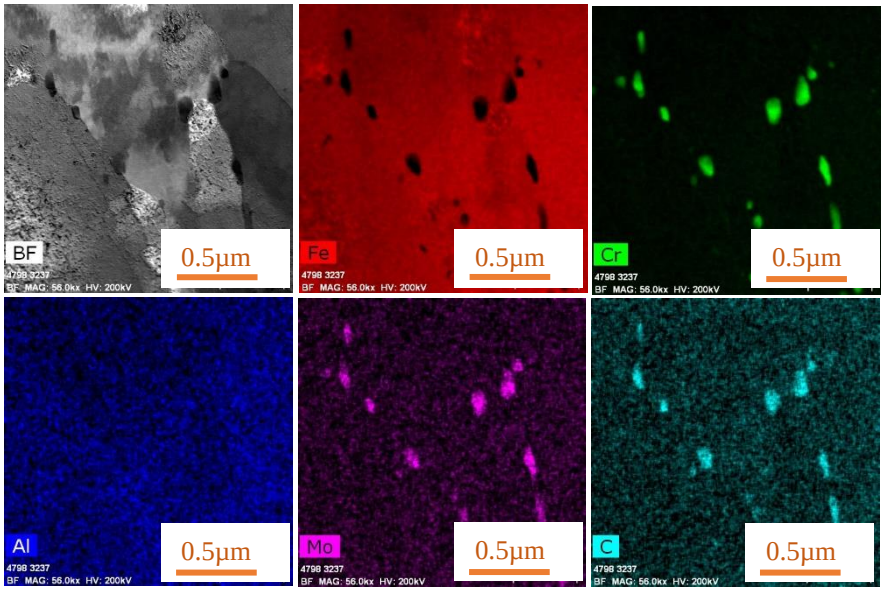

Figure 4.2. TEM-EDS elemental maps of APMT revealing Cr, Mo rich precipitates.

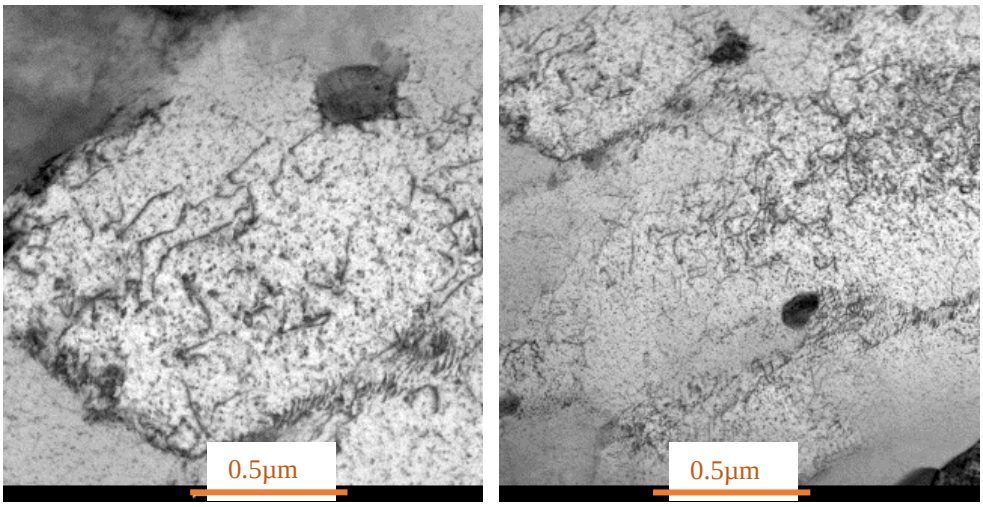

Figure 4.3. BF-TEM characterization of as-received APMT alloy, displaying distinct dislocation densities at two separate locations. The images show a high density of dislocations in the as-received specimen.

Eventually, the creep curve becomes linear with time, representing steady-state creep or the minimum creep rate in this constant load test, where the rate of dislocation recovery is balanced with the strain-hardening rate. Fig. 4.5 shows the change of the strain rate with time, decreasing in the primary creep region until the minimum creep region is reached.

Fig. 4.6 shows the steady state creep rates ($\dot{\varepsilon}_{ss}$) at test temperatures as a function of the applied stress in a double logarithmic plot. Norton's law ($\dot{\varepsilon} = A\sigma^n$) was used to present the results, where *n* (the slope of the curve) is the creep stress exponent. The curves can be divided into three regions, (low stress region I, intermediate stress region II and high stress region III). The first region, at low stresses, has a slope (n_I) = 2.8. The second region, at intermediate stresses, has a slope (n_{II}) ~ 7.45. The third region, at high stresses, has a high stress exponent (n_{III}) with an average value of 14.4. In Fig. 4.7, a power law relation has been used to relate the creep strain rate ($\dot{\varepsilon}_{ss}$) to the test temperature and activation energy (Q):

$$\dot{\varepsilon} = A\sigma^n \exp\left(-\frac{Q}{RT}\right) \tag{4.1}$$

where A is a constant, n is the creep stress exponent, Q is the activation energy for the specific deformation mechanism dominating at the region from which the data points are selected, R is the universal gas constant, and T is the test temperature.

Three different stresses were selected for the Arrhenius plot in (Fig. 4.7), one at each region in (Fig. 4.6), ($\sigma_I = 90\ MPa, \sigma_{II} = 130\ MPa, \sigma_{III} = 245\ MPa$), to show the change in the activation energy between each region. The first region at low stresses, has an activation energy (Q_I) of 252.7 kJ/mol. The second region at intermediate stresses, has an activation energy (Q_{II}) of 576 kJ/mol. The third region, at high stresses has a high activation energy (Q_{III}) of 737.97±18.7 kJ/mol.

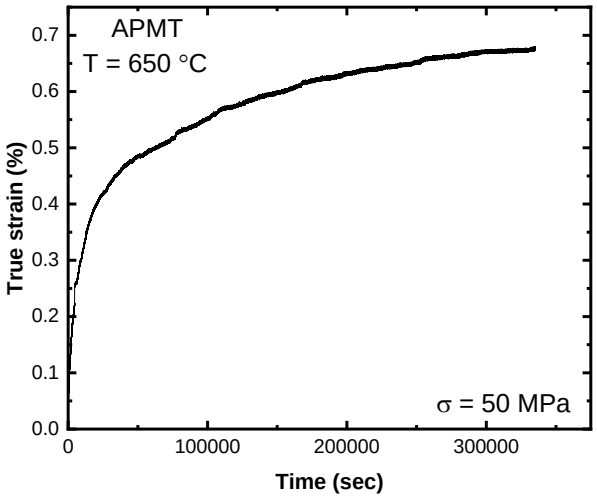

Figure 4.4. Uniaxial creep curve of APMT at 650°C and 50 MPa. The curve starts with a primary creep region, where the strain rate decreases with time until a steady state creep region is reached.

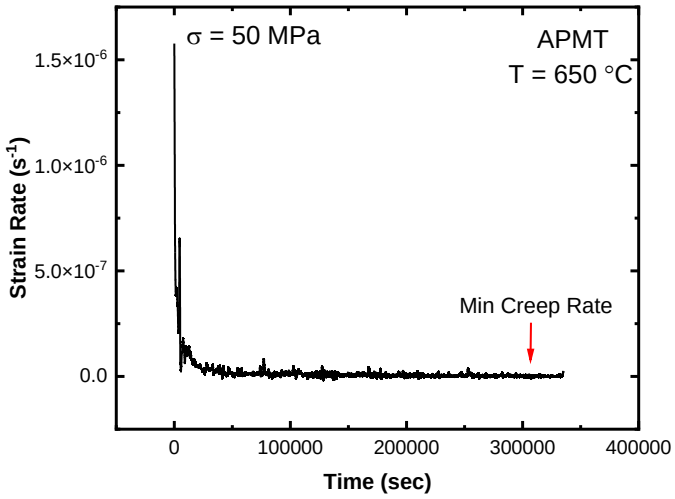

Figure 4.5. Strain rate versus time for Fig. 4.4 depicting the steady-state or minimum creep-rate at 650°C and 50 MPa.

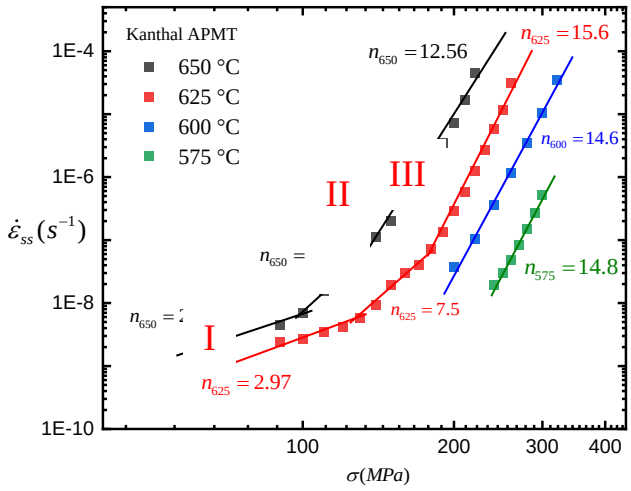

Figure 4.6. Double logarithmic plots of strain rate versus stress for APMT Alloy at various temperatures (575°C, 600°C, 625°C, and 650°C). The 625°C, and 650°C curves can be segmented into three linear regions with different slopes starting with an average n = 2.8 at low stresses, 7.45 at intermediate stresses and 14.4 at high stresses.

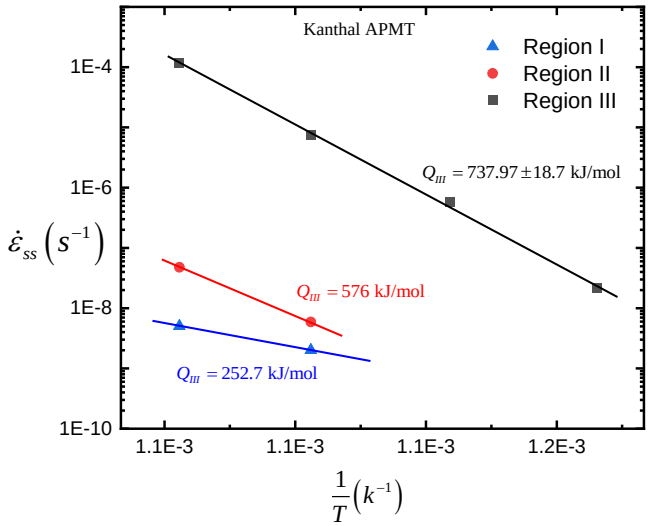

Figure 4.7. Arrhenius plots of strain rate versus (1/*T*) for APMT Alloy at the three regions. The activation energy at each of the three regions is different indicating different deformation mechanisms.

The creep results reveal an interesting creep behavior with a transition between three distinct regions with a high stress exponent for all the temperatures at high stresses. The creep parameters *n* and *Q* can be employed to identify the dominant creep mechanism. In the first region, the stress exponent is n_I~2.8 and the activation energy is $Q_I = 252.7\ kJ/mol$ suggest that dislocation viscous glide is the rate-controlling creep deformation mechanism at low stresses.

In the second region, the stress exponent is n_{II}~7.45 and the activation energy is $Q_{II} = 576\ kJ/mol$. Both (Q_{II}&n_{II}) exceed those associated with known mechanisms, particularly noteworthy is the elevated activation energy. This suggests an influence of fine precipitates on dislocation climb. The presence of Y dispersoids within the alloy grains could potentially explain the elevated activation energy in the second region, which surpasses the self-diffusion activation energy in FeCrAl system. The intermediate region, however, is too constrained to enable robust quantitative analysis. To achieve a more comprehensive understanding, further data points gathered at varying temperatures are needed.

In the third region, the stress exponent n_{III}~14.4 and the activation energy is $Q_{III} = 737.97 \pm 18.7\ kJ/mol.$ Both (Q_{III}&n_{III}) are higher than any known deformation mechanism. Ennis et al. [110] and others [25, 70, 111-114] have attributed the high stress exponent and high activation energy to precipitates acting as dislocation barriers. To overcome these precipitates, part of the applied stress is needed to increase the dislocation line length, referred to as threshold stress. The high stress exponent necessitates considering the threshold stress approach [68] to clarify the creep mechanism based on the characteristics of known creep mechanisms. An alternative approach involves conducting in-situ TEM creep testing and monitoring dislocation activity for a better understanding of the creep deformation behavior.

Table 4.1. Parametric dependencies of different creep mechanisms [20, 21].

Mechanism	*Q*	*n*
Coble	Q_{GB}	1
Nabarro-Herring	Q_L	1
Harper-Dorn	Q_L	1
Viscous glide	Q_S	3
Dislocations Climb	Q_L	4-7
Grain boundary sliding	Q_{GB}	2

Activation energies: Lattice diffusion (Q_L), Solute diffusion (Q_S), Grain boundary diffusion (Q_{GB})

2.2. Transitions in Deformation Mechanisms

The transitions between creep deformation mechanisms as stress or temperature increases have been widely reported in the literature [115], initially proposed by Murty [116-119] and later confirmed by Langdon and his colleagues in various alloys [120]. These transitions are observable in the APMT-alloy creep results, which display different regions reflecting changes in deformation mechanisms with increasing stress at a temperature. At low stresses, deformation is governed by dislocation glide. In the APMT results, the first transitional stress values are $6 \times 10^{-4}E$, where E is modulus of elasticity, at 650 °C and $8.3 \times 10^{-4}E$ at 625 °C. Before reaching these stress levels, dislocations glide in their respective slip planes while dragging solute atoms. Once the applied stress is sufficient for dislocations to unlock from solutes, the material starts to behave like a pure metal with dislocation climb becoming the controlling mechanism.

The second transitional stress values in the APMT results, where dislocations begin to climb over large precipitates, are $8 \times 10^{-4}E$ at 650 °C and $1.07 \times 10^{-3}E$ at 625 °C. At these stress levels, the applied stress provides enough energy for dislocations to increase their line length, facilitating the climbing process.

2.3. Threshold Stress Approach

Creep mechanisms for the first region was identified based on the dependency of established creep mechanisms on certain parameters. In addition, few data points exist at the middle region to identify the mechanism. However, the third regime exhibited a greater stress exponent and higher activation energy than any known mechanism. Historically, researchers have attributed these values to the presence of precipitates [9, 35, 68, 111] and used the threshold stress method to comprehend the prevailing creep mechanism, assuming the only difference is the partial consumption of applied stress to extend the dislocation line length, facilitating the climb over

precipitates. This study employed the threshold stress approach to determine the dominant creep mechanism at the upper range of examined stresses.

The approach presumes that creep deformation only occurs when the applied stress exceeds the threshold stress value. Mathematical models are employed in the threshold stress approach to describe the creep behavior of precipitation-hardened alloys. One popular model is the modified power law [121], which integrates threshold stress into the standard power law equation for steady-state creep:

$$\dot{\varepsilon} = A(\sigma - \sigma_{th})^n \exp\left(-\frac{Q}{RT}\right) \quad (4.2)$$

where $\dot{\varepsilon}$ is the creep strain rate, σ is the applied stress, σ_{th} is the threshold stress, n is the stress exponent, A is a constant, Q is the activation energy, R is the gas constant, and T is the absolute temperature. Various factors influence the threshold stress, including precipitate size and distribution, alloy composition, temperature, and prior deformation history. In the threshold analysis, the inverse of the strain rate was plotted against a range of assumed stress exponents (n = 4-7) and applied stress.

The threshold stress for each temperature was identified by extrapolating the linear curve until it intersected with zero strain rate. Following this, the threshold stress was deducted from the applied stress to ascertain the effective stress, and a new graph was plotted, considering various n values. Ultimately, by employing fitting parameters in conjunction with the recalculated n and Q values, a determination was made concerning the true stress exponent and the predominant creep mechanism.

Table 4.3 and Fig. 4.8 present the results of the threshold stress approach analysis. Fig. 4.8 illustrates the variation of activation energy with the assumed true stress exponent. As the assumed true stress exponent increases, the activation energy consistently decreases. The activation energy

at an assumed value of n = 6 closely aligns with the self-diffusion activation energy in ferritic iron [122], as indicated by the dashed blue line. Table 4.3 provides the correlation coefficient, average stress exponent and average activation energy for all assumed n values at the tested temperatures. Based on threshold analysis approach and comparing the average stress exponent, correlation coefficient and the activation energy, the rate-controlling mechanism is dislocation climb over precipitates facilitated by the increase in dislocation line length, with a true creep stress exponent (n) close to 6 and an activation energy (Q) of 252.8 ± 20.0 kJ/mol.

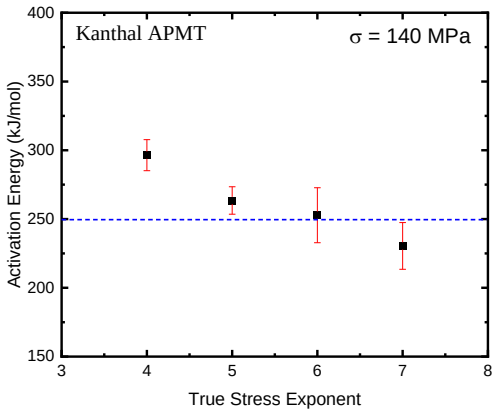

Figure 4.8. The change in the activation energy with the presumed true stress exponent. The dashed blue line represents the self-diffusion activation energy for Fe in α-Fe matrix [42].

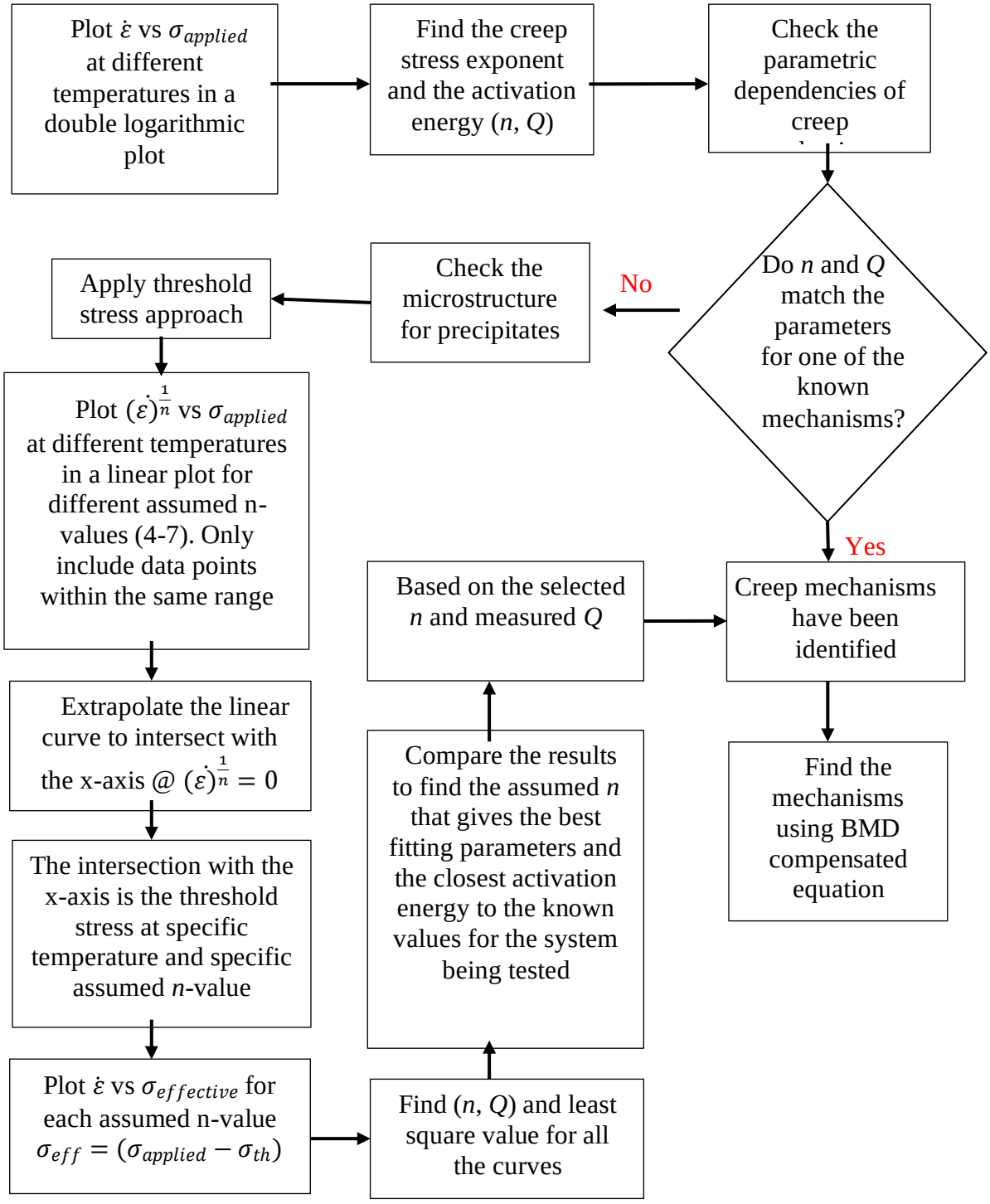

Figure 4.9. Flow chart of the threshold stress-approach analysis followed in this work.

Table 4.1. Summary of the results from the threshold-stress approach.

Assumed *n*	Temperature (°C)	Threshold (MPa)	Correlation coefficient (R^2)	Average stress exponent	Average Activation Energy (kJ/mol)
4	575	212.2	0.95	5.2 ± 1.6	296.45 ± 11.3
	600	185.5	0.99		
	625	158.7	0.99		
	650	118.6	0.99		
5	575	195.4	0.96	5.9 ± 1.5	263.5 ± 10.0
	600	168.9	0.99		
	625	145.7	0.99		
	650	105.6	0.99		
6	575	178.6	0.97	6.4 ± 1.6	252.8 ± 20.0
	600	152.1	0.99		
	625	132.6	0.99		
	650	92.4	0.99		
7	575	161.8	0.97	7.7 ± 1.2	230.5 ± 17.23
	600	135.1	0.99		
	625	119.3	0.99		
	650	79.1	0.99		

2.4. Modified Bird-Mukherjee-Dorn (BMD) Equation

The BMD equation is an extended version of the fundamental Norton equation [9, 68], allowing for comparisons between various creep mechanisms through normalized parameters. The modified BMD equation incorporating the threshold stress can be expressed by [121]:

$$\frac{\dot{\varepsilon}kT}{DEb} = A_o(\frac{\sigma-\sigma_{th}}{E})^n \tag{4.3}$$

where D is the lattice diffusivity, E is the modulus of elasticity, b is the Burgers vector, k the Boltzmann constant ($k = 1.380649 \times 10^{-23}\frac{J}{mol}$), and A_o is a dimensionless constant. The definitions for lattice diffusivity [122, 123] and elastic modulus [40] are provided below:

$$E_{APMT}(GPa) = -3.1 \times 10^{-5}T^2 - 6.15 \times 10^{-2}T + 218 \tag{4.4}$$

$$D = D_O e^{-\frac{Q}{RT}} = 5 \times 10^{-4} \times e^{-\frac{Q}{RT}} \tag{4.5}$$

where temperature is provided in units of Celsius. Fig. 4.10 depict the diffusion-compensated creep rate $\left(\frac{\dot{\varepsilon}kT}{DEb}\right)$ against the modulus-compensated effective stress $\left(\frac{\sigma-\sigma_{th}}{E}\right)$ for the low-stress regime. In the low-stress regime, the threshold stress is set to zero and the data points align along a straight line with $\text{slope} = n_I = 2.6 \cong 3$, in equation (4.6). This stress exponent indicates that the prevailing creep deformation mechanism at the lower end of the investigated stress range is the dislocation glide mechanism.

$$\ln\left(\frac{\dot{\varepsilon}kT}{DEb}\right) = \ln(A_o) + n \times ln\left(\frac{\sigma-\sigma_{th}}{E}\right) \tag{4.6}$$

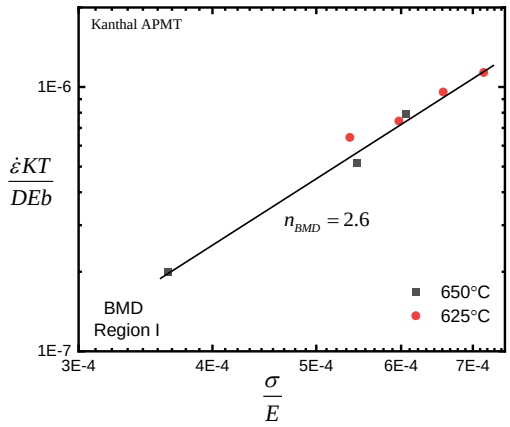

Figure 4.10. Diffusivity compensated strain rate versus elasticity compensated stress for the low stress region in (Fig 4.6). The data points align along a straight line with slope $=n_{il}=2.6\cong 3$.

In the high-stress regime, stress exponent of 6 was seen to be the appropriate one (Fig. 4.8) once threshold stress is considered. Thus, the BMD plot of the normalized strain-rate with normalized effective stress $\left(\frac{\sigma-\sigma_{th}}{E}\right)$ is shown in Fig. 4.11 that revealed R^2 (Coefficient of Determination) value to be 0.93. Thus, dislocation climb is believed to be the rate controlling mechanism such as appropriate for precipitation strengthened materials.

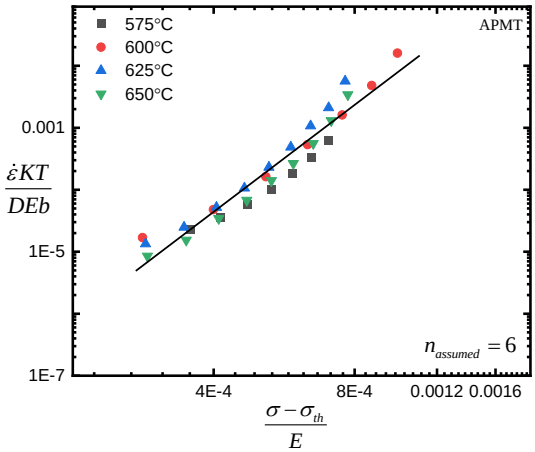

Figure 4.11. The modified BMD plot for the high stress region in (Fig. 4.6) using normalized effective stress exhibiting stress exponent 6 corresponding to dislocation climb over precipitates.

2.5. Post-Test Characterization

Fig. 4.12 shows the microstructure of the creep tested APMT alloy specimen at 625 °C, as observed through TEM images, revealing several noteworthy features. Firstly, the density of dislocations near the grain boundaries is higher than in the as-received specimen, suggesting an increase in dislocation activity close to the grain boundary area during creep. Moreover, the Y distribution is uniform across the tested area, with no signs of segregation or formation of Y-rich secondary phases (Fig. 4.13b). This uniformity indicates the stability of Y dispersoids throughout the creep test.

Bowing of dislocations is frequently observed in the images (Fig. 4.14), which could be indicative of an increase in dislocation line length to bypass precipitates. This phenomenon suggests that the dislocations are adapting to overcome obstacles in the microstructure. The BF-TEM images in (Fig. 4.15) also reveal that some regions of the creep-tested specimen are free of precipitates, while others exhibit carbide precipitates at the grain boundaries. Lastly, the morphology and size of the precipitates appear to be relatively unchanged before and after testing. This observation suggests that the precipitates have remained stable during the creep test at 625°C, maintaining their role in strengthening the alloy throughout the test duration.

Cr-containing alloys are prone to microstructural alterations when subjected to high temperatures and stresses for extended duration. The primary driving force behind these changes is not well understood, and ongoing investigations aim to unravel the thermodynamics and kinetics that drive the formation of Cr-rich α′ second phase in Cr-containing alloys. Wen et al. [124] observed the emergence of Cr-carbide precipitates at grain boundaries in Kanthal-D, a precipitation-strengthened FeCrAl alloy with the same Cr content as APMT. Isik et al. [125]

reported the formation of Mo-rich particles near $M_{23}C_6$ grain boundary carbides in 12% Cr ferritic steel, which occurred during aging and creep testing at 550 °C and 120 MPa.

Although carbides were detected in this study using TEM techniques, there were no significant differences between the microstructure of the creep-tested specimens and the as-received specimens. And there were no indications of Y segregation. This observation suggests APMT microstructure's stability during prolonged creep test periods. However, none of the tests reached fracture, leaving the impact of microstructural features on the creep rupture behavior in APMT an open research topic.

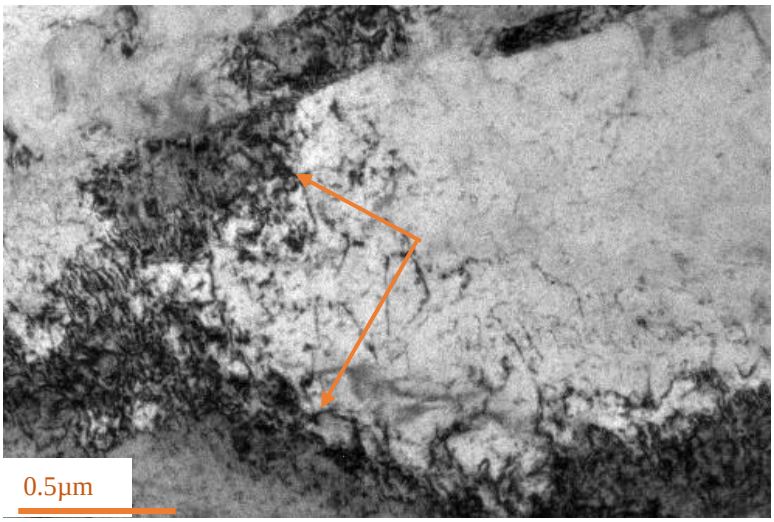

Figure 4.12. High magnification BF-TEM image of dislocations near the grain boundaries. The arrow points towards regions with high density of grain boundary dislocations, which might be pinned by grain boundary precipitates during the creep deformation.

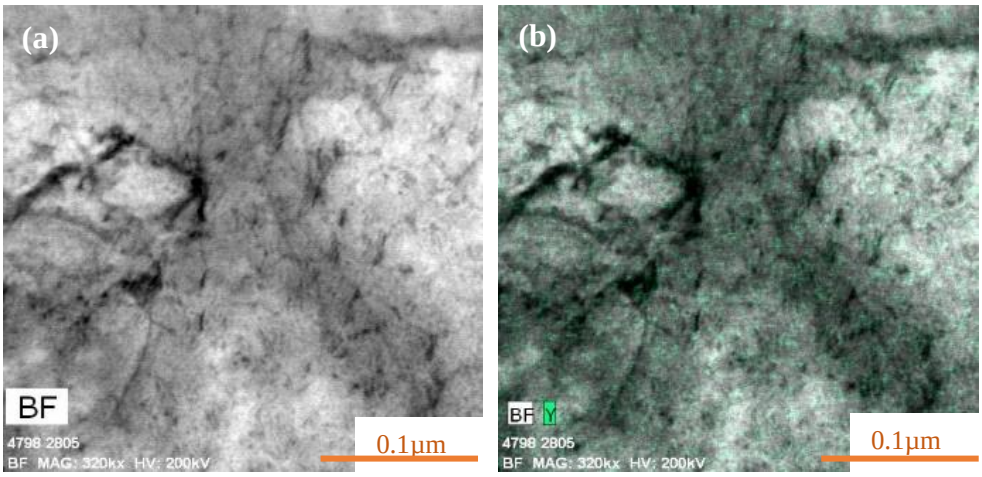

Figure 4.13. Bright field TEM images before (a) and after (b) creep test at 625°C depicting uniform distribution of Y.

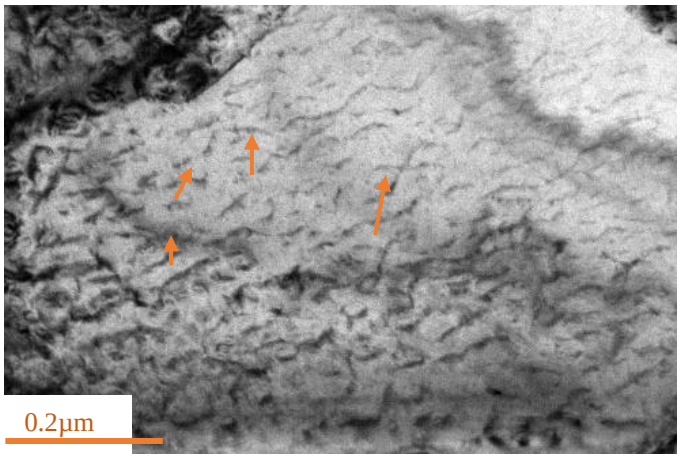

Figure 4.14. High magnification BF-TEM image depicting the bowing of dislocations inside the grains. The arrows point towards dislocations lines.

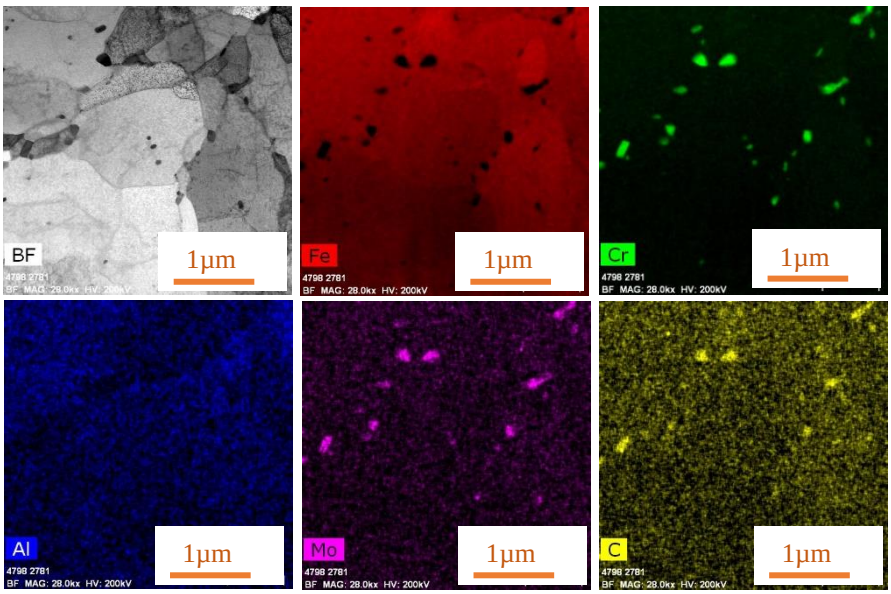

Figure 4.15. Intermediate magnification BF-TEM image and STEM-EDS elemental maps showing second phase precipitates ($M_{23}C_6$ Carbides) distribution in APMT crept specimen at 625˚C. No signs of Al segregation or precipitation in the matrix.

5. Creep Behavior of 14YWT Alloy (A Microstructural Examination and the Role of Precipitates)

1. Introduction

The 14YWT alloy, a nanostructured ferritic alloy (NFA), has garnered significant interest due to its promising high-temperature performance and radiation resistance which are crucial characteristics for nuclear energy applications [9, 55, 126-130]. This alloy, a product of collaborative development in the early 2000s by researchers from the University of California, Santa Barbara, Los Alamos National Laboratory, and Oak Ridge National Laboratory, exhibits an exceptional combination of properties [45, 49, 126, 131] due to its fine grain structure, high nanoscale oxide particle density, and an iron-based matrix with a nominal 14 wt.% Cr. The "14" in the alloy's name is due to the Cr content, and the addition of Y, W, and Ti, denoted by "Y," "W," and "T," respectively.

The precise addition of these elements and thorough processing lead to the formation of nanoscale oxide particles and clusters, giving the alloy its distinctive properties. Given the critical need for materials capable of withstanding the severe environment in fusion reactors, such as high temperatures, pressures, and radiation [58], the 14YWT alloy has shown potential in meeting these stringent demands due to its high strength, toughness, and radiation resistance [49]. The process of nuclear fusion – the fusion of two or more atomic nuclei into a heavier nucleus releasing significant energy – offers an avenue for abundant, safe, and clean energy production [7, 9, 16, 17, 24, 28]. However, the realization of fusion energy demands innovative solutions to numerous challenges, chief among them being the development of suitable materials. To this end, the 14YWT alloy, with its remarkable properties, has emerged as a promising candidate for fusion energy applications.

Before we proceed, it is important to note that a total of 12 different ingots (heats) of 14YWT have been fabricated thus far [49]. One of the primary characteristics of nanostructured materials is their dependence on the fabrication history, which directly influences their properties. Consequently, exploring the properties of each ingot is essential for comprehending the intricate relationship between fabrication, microstructure, and resulting properties.

Moving forward, we turn our attention to the unique microstructure of 14YWT alloy, a significant factor that determines its distinct properties and behavior under various stress conditions. Miller et al. [132] demonstrated that the mechanical alloying of finely pre-alloyed (Fe-12.3 wt% Cr-3% W-0.39% Ti) metal and Y powders leads to the production of oxide dispersion-strengthened (ODS) ferritic alloys, exhibiting significantly enhanced mechanical properties at high temperatures. Insights from atom probe tomography (APT) suggested that these augmented high-temperature mechanical properties are associated with the existence of extremely stable Ti, Y, and O-enriched particles with a 2-4 nm diameter. These ultra-fine particles remained stable during extended creep experiments lasting over 14,000 hours at 800°C and even during annealing at temperatures reaching up to 1300°C [47, 48]. The concentrations of Y and O in the ferrite matrix were substantially higher than the equilibrium levels. The findings might be tied to the interactions between O-Ti, O-W, O-Y, and O-Cr solute atoms, which could potentially affect solute diffusion [132].

Bentley et al. [45] demonstrated that extrusion conducted at 850°C led to a bimodal grain distribution with areas typically larger than 10 μm containing either 1-2 μm (large) grains or 100-200 nm (small) grains. The characterization indicated the presence of nanoclusters (NC) in the areas with small grains. These grain boundaries were densely decorated with clusters and exhibited an enrichment in Cr. Although no NC were identified within the large-grained areas, a sparse

concentration of Ti-rich oxide particles, typically larger than 20 nm, was found just as in the small-grained regions. The study also highlighted considerable W inter-granular segregation within the small-grained regions.

Miller et al. [47] carried out an APT analysis, which unveiled that ODS 14YWT ferritic alloys, in their as-extruded state, comprise a high count of NC, enriched with Ti, Y, and O, at the nanometer scale. Remarkably, these NC showed extreme resilience against coarsening, even at temperatures reaching 1000°C or higher. In a separate study, Miller et al. [48] explored the importance of Y addition in stabilizing coherent NCs. Without Y, the formation of a TiO2 oxide phase becomes possible. Conversely, an excess of Y can lead to the emergence of a Y-Ti-O oxide. Consequently, the recipe for stable NCs involves a well-distributed Y content with a higher proportion of Ti to Y.

On a different note, Bhattacharyya et al. [128] discovered that the world of nano-features (NFs) is diverse. His findings suggest that there is not just one type of NF; instead, there is a "zoo" of NFs, even within a single alloy. Cunningham et al. [133] conducted research into how changes in O levels impact 14YWT NFA that contain a high concentration of Y–Ti–O NFs. This investigation employed techniques such as TEM, APT, and small-angle neutron scattering (SANS). The alloy that had the least amount of O contained the fewest and most substantial NFs. An increase in micro-hardness with higher O content correlated with a proportional increase in the NF volume fraction and variations in the grain size. Their study assessed the impact of bulk O content, which varied from 0.07 to 0.25 wt.%, on the NFs in three 14YWT NFAs that otherwise had comparable compositions and manufacturing processes. The findings revealed that O significantly influences the NFs, the balance of the microstructures, and mechanical properties. This was partly attributed to O's effect on the composition and size of the dispersion strengthening

oxides. It was also noted that excessive O could be detrimental to NFAs, leading to the formation of larger scale precipitates which may compromise ductility and toughness. Therefore, maintaining a balance between Y, O, and Ti is crucial for the quality of the NFAs.

Cunningham et al. [134] suggest that a ratio of 0.2 wt.% Y, 0.4 wt.% Ti, and 0.15 wt.% O might be close to optimal for creating a high quantity of NFs. Miller et al. [135] reported the observation of three unique groups of precipitates: Ti(N,O,C) with sizes between 20–50 nm, Y2Ti2O7/Y2TiO5 with diameters of 5–10 nm, and Ti,Y,O-enriched NCs with diameters of 1–4 nm. The primary locations of the first two groups were along the grain boundaries, often accompanied by Cr, W, and C segregation. A concentrated population of NCs was noted within the grain structure as well as along the grain boundaries.

Tan et al. [58] revealed the presence of small particle strings within the microstructure. In certain regions of the microstructure, groups of larger grains were observed. These grains were typically elongated along the axis of extrusion and likely originated from a single ball-milled particle. The particle strings also tended to align along the extrusion direction. Multiple Ti-rich phases, including the Ti-rich oxide, TiO2, and Ti(O, C, N) particles, were identified in 14YWT ingots. The microstructural investigation demonstrated a clear bimodal grain size in the FCRD-NFA1 (ingot notation) sample [58]. While the texture might partly contribute to the appearance of larger grains, other factors could also be at play. For instance, it is possible that the Y is not evenly distributed throughout the ball-milled powders at the microscopic level, as suggested earlier. Pal et al. [136] highlighted the presence of nano-oxides (NOs), specifically Y-Ti-O, at the nanoscale. These were distributed mainly within sub-micron-sized grains and were accompanied by a high dislocation density. Eftink et al. [130], on the other hand, discovered that the grains in a 14YWT

sample measured between 10-50 μm at their smallest and were stretched in the longitudinal direction.

Previous researchers have examined the creep behavior of various ingots of 14YWT alloy. Hayashi et al. [137] assessed the microstructures and creep attributes of the ODS 14YWT alloy, taking into account the variations resulting from annealing at 1000℃ for different durations. Despite significant grain-coarsening, the minimum creep rate shows relative indifference to the change in grain size. The creep strength is credited to highly stable Ti-rich NC, which seem to anchor the original primary grains and pose robust barriers to dislocation movement within the large, anomalously grown grains. Schneibel et al. [8] investigated and found that the creep rate at 800℃ is slower than the rate anticipated for diffusional creep. Potential explanations for this include the high coverage of NC, enrichment of Cr and W at the grain boundaries, and the suppression of self-diffusion. The stress exponent reduces from a value of 35 at high stress levels to a substantially smaller value, roughly around 1 at lower stress levels. High stress exponents are characteristic of dislocation creep in ODS materials.

Susila et al. [53] carried out research on the compression creep properties of a nanostructured ferritic ODS alloy (Fe–12Cr–2W–0.5Y2O3 in wt.%), which was synthesized via mechanical alloying and vacuum hot pressing. A specific focus was placed on investigating the impact of the initial Y particle size on the microstructure and creep properties. The creep tests were performed at a constant strain rate, leading to stress alterations during the test that could potentially reach a constant value if the microstructure remained stable. Susila et al. [53] revealed that the Ti-containing ODS alloys with more refined dispersoids demonstrated superior creep resistance when tested at 800℃ and 900℃. Further examination of the stress exponents indicated that dislocation creep was the predominant deformation mechanism at 800℃ and 900℃. The observed stress

exponent (*n*) values ranged from 9 to 15 for the ODS alloys. Significantly, it was found that the creep resistance of 14YWT was markedly superior to that of the Fe-12Cr-2W based alloys. This can be explained by the fact that the addition of Ti resulted in the creation of NCs of Y–Ti–O of 2–4 nm in size.

Singh et al. [52] explored the grain boundary (GB) diffusion of Fe in nanocluster-strengthened ferritic steel (Fe–14Cr–3W–0.4Ti–0.25Y2O3 in wt.%). They discovered that the GB self-diffusion coefficient for 14YWT only diverges from that of α-Fe. This observation acknowledges that the grain boundaries of 14YWT are composed of NC and that W and Cr are segregated. Nevertheless, the creep rate of 14YWT at 800℃, where stress and strain rate bear a near-proportional relationship, is roughly eight orders of magnitude less than what is predicted for Coble creep. This implies a significant impediment to Coble creep in 14YWT. The hindrance is attributed to the GB diffusion being significantly slower in 14YWT than in α-Fe. The NC serve as a barricade against GB sliding, thus constraining diffusional creep. Kim et al. [138] conducted an analysis of the stress relaxation behavior at elevated temperatures, which varied from 600 to 1000℃. To evaluate the strain rate sensitivity of the alloys, the load drop-time curves were transformed into stress-strain rate curves. The activation energy of 14YWT was found to fluctuate between 260 and 405 kJ/mol within the temperature range of 600 to 800℃.

Brandes et al. [139] studied the creep behaviors of 14YWT across a spectrum of temperatures and stresses. The stress exponent was noted to fluctuate non-linearly with the applied stress, decreasing as stress decreased, and nearing unity at lower stress levels. Studies using TEM revealed that glide dislocations are drawn towards and secured by NC within the nanoscale grains. TEM findings suggest that the microstructure remains stable during creep and that dislocation

glide is the principal deformation mechanism. The observed interactions between dislocations and NC confirm that the gliding dislocations are easily ensnared by the fine scale particles.

Hoelzer et al. [49] summarized the results of tests conducted at Oak Ridge National Lab (ORNL), in which three samples were produced and tested in a constant stress setting at stress levels of 300, 250, and 200 MPa at a temperature of 800℃. A single specimen was also employed for the time-to-failure creep test under a constant load of 100 MPa at the same temperature. Creep curves were acquired under the same constant stress conditions at 200, 250, and 300 MPa at 800℃. The findings revealed a noticeable decline in the time to failure with an escalating stress at 800ºC. Failure time was around 10 minutes at the peak stress of 300 MPa, extending to approximately 4.75 hours at 250 MPa and further to 102 hours at the minimum stress of 200 MPa. The creep curves illustrated a quick increase in strain during the primary creep, swiftly transitioning to secondary creep in the tests using 200, 250, and 300 MPa at 800 ℃. All tests displayed secondary creep happening over brief periods, subsequently ending with failure, with virtually no sign of tertiary creep. Furthermore, all three tests culminated in the specimens failing at relatively low strain levels (below 1%). The time-to-failure creep test was halted without any specimen breakdown after 20,327 hours, equating to 2.32 years. The stress exponent (n) was calculated from the constant stress control creep tests at the previously mentioned stress levels of 200, 250 and 300 MPa at 800℃. The calculated value was n = 23.9, aligning with the threshold stress behavior for the 14YWT-SM10 heat under these specific creep test conditions.

In another study, Hoelzer et al. [140] performed Strain Rate Jump (SRJ) creep tests on axial specimens crafted from thin-walled tubes of the ODS 14YWT alloys. These SRJ creep tests were also carried out at a temperature of 800℃. The stress exponent (n) was derived from the SRJ test data. The results showcased the highest stress exponents of n = 19.8 and n = 35.0.

The present study embarks on an examination of the creep behavior of 14YWT-NFA1 (Ingot designation) alloy under various stresses, ranging from 80 MPa to 340 MPa, and at three different temperatures, namely 600°C, 625°C, and 650°C. Our investigation includes the 14YWT-NFA1 ingot, which has not undergone any prior creep studies [49]. A major object is to evaluate the creep deformation mechanism in the range of temperatures and stresses mentioned above.

2. Experimental Results

2.1. Microstructural Characterization of the as-received material

X-ray diffraction investigations revealed the notably strong (200) peak, which suggests that 14YWT-NFA1 possesses a non-random texture, meaning the crystallites are not oriented randomly and have a preferred orientation. The lattice constant for the as received 14YWT-NFA1 is measured to be 2.885 Å. The position of the (211) peak diverges from the standard peak position, which could potentially be due to residual stress. Secondary electron backscatter diffraction was utilized to study the grain structure of the as-received 14YWT-NFA1 materials as shown in (Fig. 5.1). Consistent with prior microstructural characterizations conducted on the same ingot [49], the microstructure consisted of strings of larger grains enveloped by intermediate-sized grains indicating a bimodal grain size structure. In the specimens subjected to characterization, the strings were observed to be distributed randomly across the scanned area. Moreover, it was evident that nano-voids were present at the grain boundaries (Fig. 5.2). In some instances, these nano-voids were sizable enough to form a small micro-crack along the grain boundaries. However, no cracks were observed within the grains in any of the tested specimens.

All the images derived from secondary electron backscatter diffraction, regardless of their location, showed bright second-phase precipitates at the grain boundaries. The brightness in the backscatter images indicates that these precipitates are rich in heavy elements. To identify the

precipitates, further SEM-EDS analyses were performed. As displayed in (Fig. 5.3), the precipitates are heavily enriched with W with no other elements segregating close to W-rich precipitates. Upon analysis of the microstructure of the same ingot in earlier studies [8], it was observed that the precipitates were predominantly enriched with Cr, instead of being W-rich as shown in this study.

The BF-TEM images of the as-received specimens (Fig. 5.4) show grains with a high density of dislocations coexisting alongside clean grains. This phenomenon could potentially be attributed to the heterogeneous distribution of precipitates among the grains. Specifically, certain grains may remain devoid of precipitates, and within these grains, the rate of dislocation annihilation is expected to be significantly higher compared to that in grains populated with precipitates. Consequently, this accelerated dislocation annihilation process could result in the formation of clean grains. The W-rich precipitates are depicted as black spots in the BF-TEM images provided in (Fig. 5.4). Remarkably, some of the W-rich precipitates observed were found to be of comparable size to the existing grains within the material.

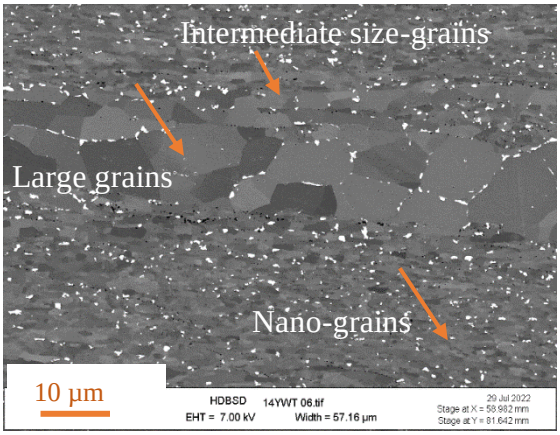

Figure 5.1. Secondary Electron Backscatter Diffraction (BSD) image showing bimodal grain structure with a string of large grains within the nano-grain matrix.

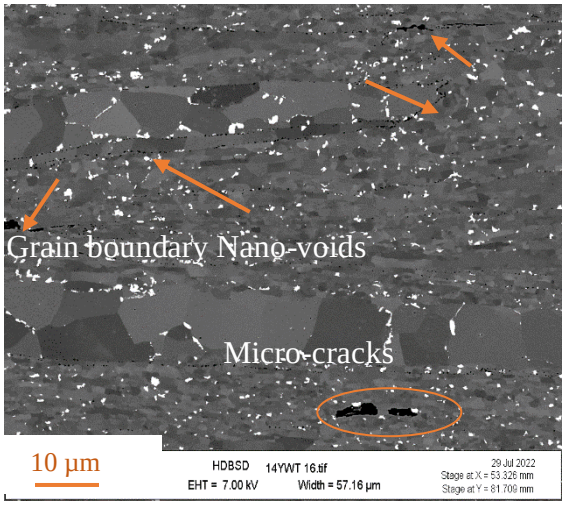

Figure 5.2. BSD image showing nano-voids at the grain boundaries along with micro-cracks.

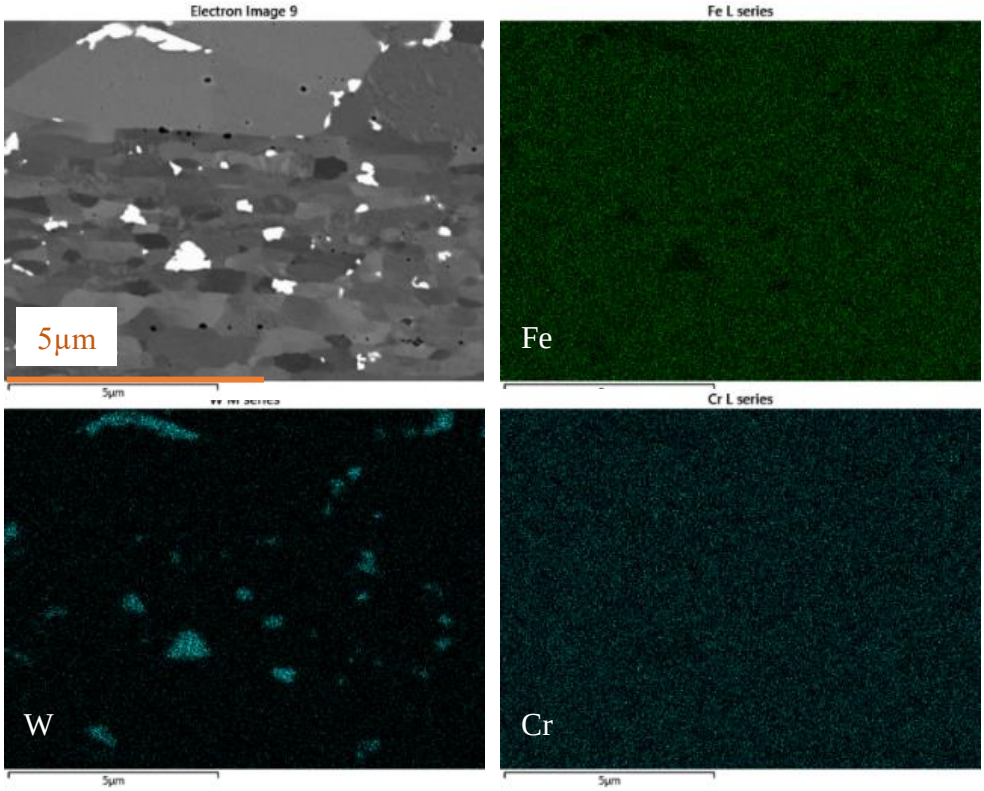

Figure 5.3. Scanning Electron Microscopy-Energy Dispersive X-ray Spectroscopy (SEM-EDS) elemental maps for Fe, W, and Cr. W SEM-EDS maps show W secondary phases.

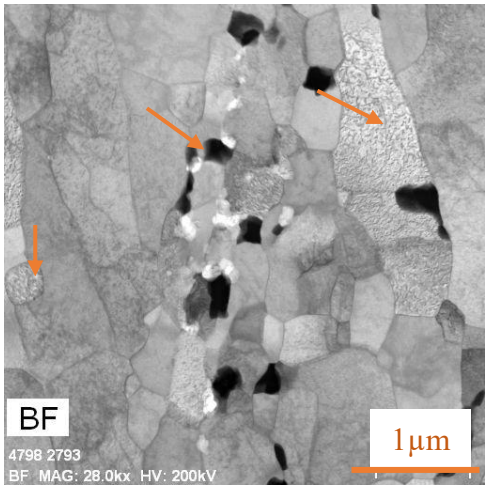

Figure 5.4. BF-TEM image for the grain structure of the as-received specimen fabricated from 14YWT-NFA1 ingot. The arrows point towards grains with high dislocation density and W-precipitates. The black spots represent the W-precipitates.

2.2. Uniaxial Creep Properties

A typical example of creep curves from a 14YWT-NFA1 sample tested at 650°C under three different stress conditions can be seen in (Fig. 5.5). The creep curves in Fig. 5.5a, c, and e commence with a primary creep area defined by an exponential-like function with a slope decreasing over time due to dislocation hardening. Over time, the curve transitions to a linear pattern, indicating steady-state creep ($\dot{\varepsilon}_{ss}$) or a minimum creep rate during this constant load test, wherein the rate of dislocation recovery is equal to the strain-hardening rate. Fig. 5.5b, d, and f illustrate the decreasing strain rate with time in the primary creep region until the minimum/steady-state creep area is attained. Fig. 5.5e and f demonstrate the variation of strain and strain rate versus time at 340 MPa and 650°C.

The curve can be divided into three sections based on the change in strain rate with time. The first segment corresponds to the primary creep area, marked by decreasing strain rate. The second segment corresponds to the minimum creep rate, and the third segment relates to the tertiary creep area marked by a rapidly increasing strain rate. Fig. 5.6 displays the steady-state creep rates

($\dot{\varepsilon}_{ss}$) versus the applied stress on a double logarithmic plot. Norton's Law ($\dot{\varepsilon} = A\sigma^n$) can be used to represent the results, where *n*, the slope of the curve, is the creep stress exponent. At low stress region, the slope of the curves at the three temperatures are close to unity while it increases in the high stress region to ~15. A power-law relation is used to connect the creep strain rate ($\dot{\varepsilon}_{ss}$) to the applied stress (σ) along with the Arrhenius function of the test temperature with activation energy, *Q*, as shown in Eqn. 5.1 and Fig. 5.7,

$$\dot{\varepsilon} = A\sigma^n \exp\left(-\frac{Q}{RT}\right) \tag{5.1}$$

where, *A* is a constant, *n* represents the creep stress exponent, and *Q* is the activation energy for the specific deformation mechanism dominating in the region from which the data points are drawn. *R* signifies the universal gas constant and *T* is the test temperature [9]. Two separate stresses were chosen for the Arrhenius plot, one in the region where *n* is close to 1 and the other stress is within the region where *n* is close to 15, to illustrate the change in activation energy with the change in the stress exponent. Fig. 5.7 presents an Arrhenius plot of the steady-state strain rate against the reciprocal of the absolute temperature. The first region at low stresses has a slope (n_I) nearly equal to 1 and an activation energy (Q_I) of 244.58±29.56 kJ/mol while the second region at higher stresses has an average slope (n_{II}) around 15 with an activation energy (Q_{II}) of 388.56 kJ/mol.

The parameters *n* and *Q* can be utilized to pinpoint the prevailing creep mechanism. In the low stress region, the stress exponent n_I is approximately 1, and the activation energy $Q_I = 244.58 \pm 29.56\ kJ/mol$ identifiable with the activation energy for self-diffusion of Fe points to Nabarro-Herring creep being the mechanism primarily responsible for the creep deformation. This is in line with previous creep studies performed using different 14YWT ingots [8, 53, 54, 137, 139-141].

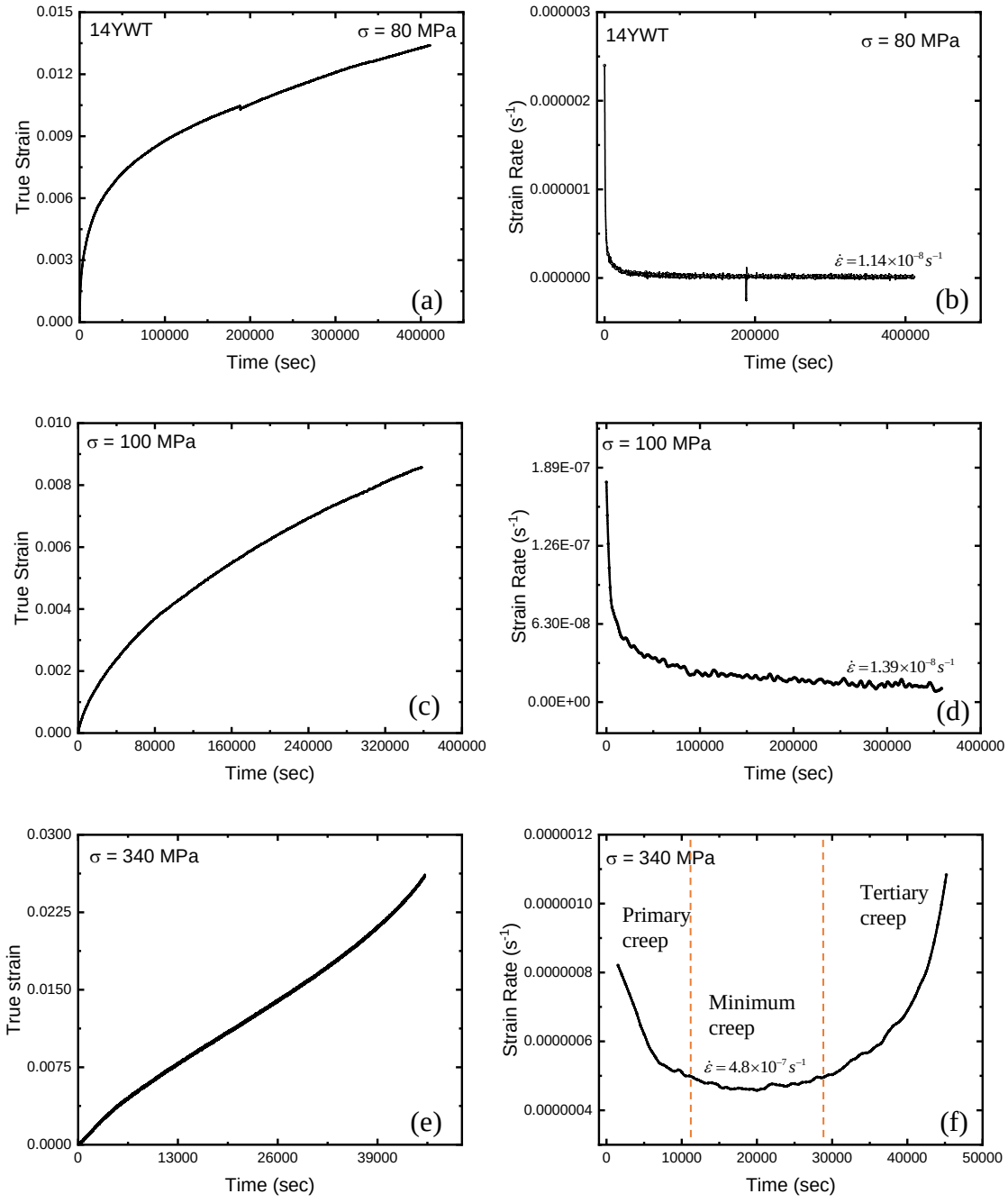

Figure 5.5. 14YWT Alloy true creep strain and strain rate versus time at three different stress conditions at 650°C. (a, c, e) curves show true strain versus time while (b, d, f) depict the derivative of the true strain curve with time.

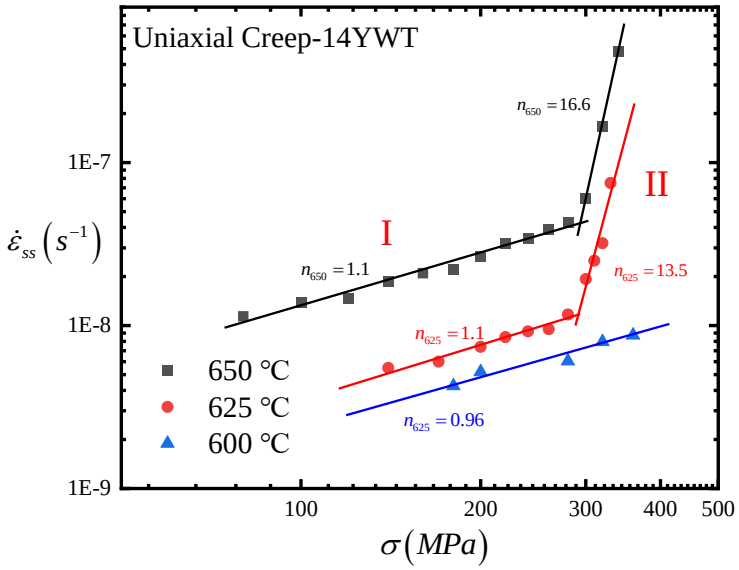

Figure 5.6. Double logarithmic plot of strain rate versus stress for 14YWT Alloy at three different temperatures (600°C, 625°C, and 650°C).

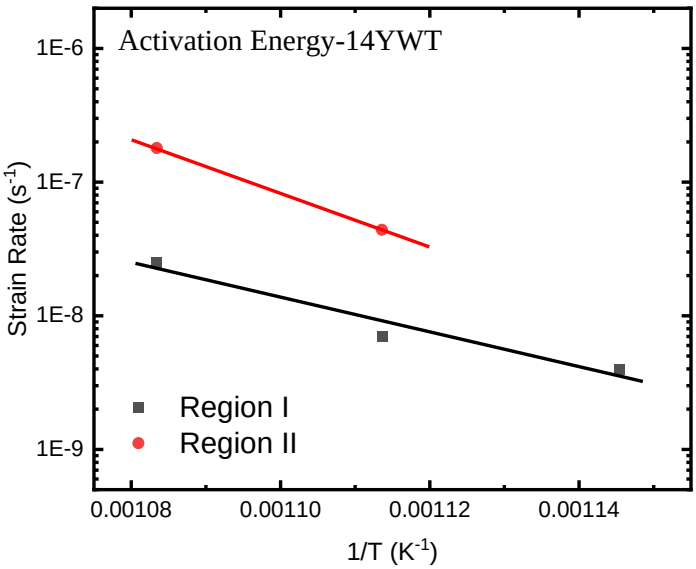

Figure 5.7. Arrhenius plot of strain rate versus (1/*T*) for 14YWT Alloy in the two stress exponent regions shown in Fig 6. Two activation energies were calculated. In region I, the activation energy (*Q*) is close to 244.58±29.56 kJ/mol. In region II, the activation energy (*Q*) is 388.56 kJ/mol.

The observed behavior is in accordance with the understanding that the stress fields originating from the high-volume fraction of grain boundaries exert influence on the dislocation sources. Furthermore, the configuration of the grain boundaries acts as an impediment to the motion of dislocations. This impedance is attributable to the presence of precipitates within the grain boundaries, which serve as obstacles to dislocation movement [9, 68].

In contrast, the second region exhibits a stress exponent n_{II} of around 15 and an activation energy Q_{II} of 388.56 kJ/mol. These values (Q_{II} and n_{II}) exceed those of any known deformation mechanisms (Table 4.2). The high stress exponent and high activation energy can be attributed to the role of precipitates as dislocation barriers. No high stress exponent was observed at 600℃ up to stresses close to the yield stress. To better understand this high-stress exponent, the threshold stress approach might provide insights into the creep mechanism, based on the characteristics of known creep mechanisms. However, this requires additional data points at varying temperatures. An alternative approach could involve carrying out in-situ TEM creep testing and monitoring dislocation activity to gain a deeper understanding of the creep deformation behavior. Table 5.1 outlines the proposed creep mechanisms for 14YWT alloy within the temperature and stress ranges tested in this study.

Table 5.1. Summary of the proposed creep mechanism for 14YWT-NFA1.

	Region I	Region II
Stress Exponent (n)	1	15
Activation Energy (Q) (kJ/mol)	244.58 ± 29.56	388.56
Mechanism	Nabarro-Herring	Climb over precipitates

2.3. Post-Test Characterization

Fig. 5.8a shows a BF-TEM image that displays the grain structure of a 14YWT-NFA1 alloy, which has undergone a creep test at 625°C. This TEM image exposes several interesting characteristics. Firstly, the tested specimen exhibits an elevated number of grains possessing a high dislocation density, in comparison to the as-received specimen. Additionally, precipitates along the grain boundaries are observed after the test, with no evidence of enlargement or dissolution compared to the as-received state. This suggests that the precipitates have withstood the creep test at 625°C, thereby continuously contributing to the alloy's strengthening throughout the duration of the test. The arrows in (Fig. 5.8a) indicate grains with a high dislocation density and dark-colored inter-granular precipitates.

A more magnified BF-TEM image of a grain with a high density of dislocations is provided in (5. 8b) with the arrow pointing towards dislocations, which might be pinned by fine precipitates distributed within the grain. To further examine the elemental distribution across the grain boundaries and within the grains themselves, additional TEM-EDS characterization has been performed that revealed the existence of two types of precipitates. Fig. 5.9 shows Y-Ti-O rich precipitates located along the grain boundaries. Interestingly, Y was found not only to create relatively larger precipitates along grain boundaries, but also to form much smaller precipitates within the grains. Fig. 5.10 shows W- rich precipitates that are larger compared to the Y-Ti-O rich precipitates. W-rich precipitates are large enough to form their own grains. However, like the Y-Ti-O rich precipitates, the W-rich precipitates were only found along the grain boundaries.

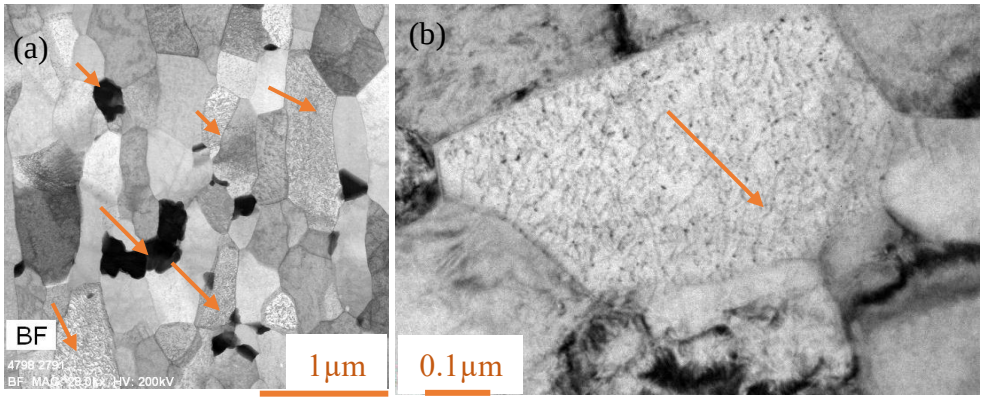

Figure 5.8. (a) Intermediate magnification BF-TEM images of grains with high dislocation densities and dark precipitates at the grain boundaries. (b) High magnification BF-TEM of one of the grains with the high density of dislocations.

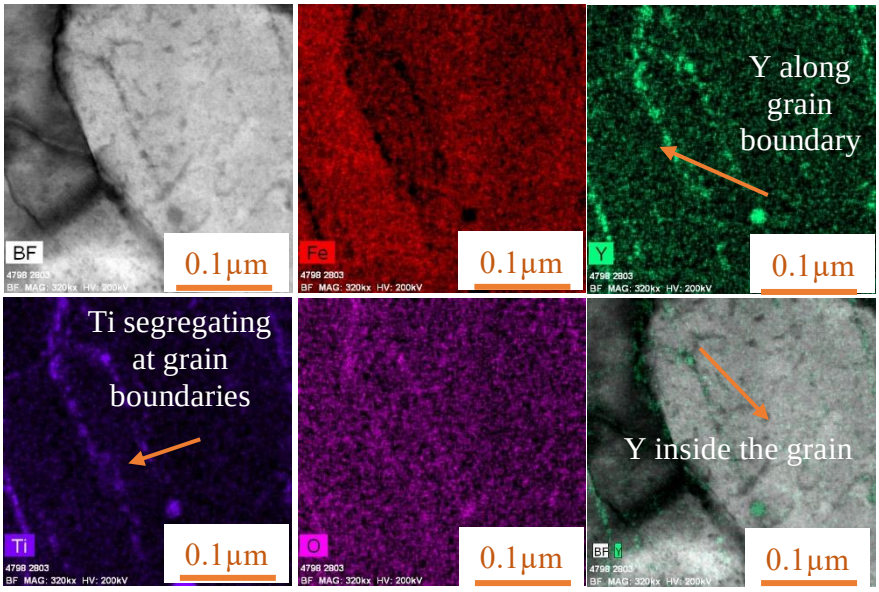

Figure 5.9. High magnification BF-TEM image and STEM-EDS elemental maps showing Y-Ti-O rich precipitates along the grain boundaries. Along with grain boundary Y-Ti-O precipitates, the BF image with the Y SEM-EDS map shows that Y is also present with the grains as well.

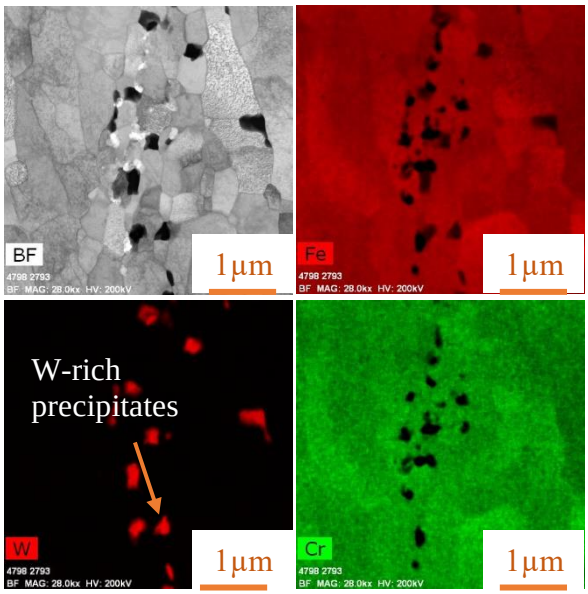

Figure 5.10. Low magnification BF-TEM image and STEM-EDS elemental maps showing W-rich precipitates along the grain boundaries with larger sizes compared to the Y-Ti-O precipitates in the previous figure. Some of the W-precipitates are as large as small grains.

One of the central observations from the BF-TEM images is the remarkable stability of the grain structure even when subjected to high-stress creep testing over extended periods. This stability could be attributed to the precipitates along the grain boundaries that potentially impede any significant grain growth. A particular characteristic noted is the presence of two distinct types of precipitates: W-rich precipitates and Y-Ti-O rich precipitates. Interestingly, these two types of precipitates never appeared concurrently on the same grain boundary, or even in proximity within all examined regions. This may hint towards the impact of specific microstructural conditions on their formation and distribution. Furthermore, the results from the TEM-EDS mapping for W in post-creep specimen exhibited concentrated localizations only at the precipitates. This observation brings into question the solubility of W in the given matrix and could lead to questions regarding the fabrication process and possible compositional variations within the same ingot. An additional point of note is the size difference between the two types of precipitates: the W-rich precipitates

were observed to be larger than the Y-Ti-O precipitates. This variation in precipitate size may influence the overall creep behavior of the alloy, potentially offering an area for further investigation.

The findings of this study regarding the microstructure of 14YWT-NFA1 reveal a similarity with previously investigated 14YWT ingots, particularly in the context of the presence of Y-Ti-O precipitates. Nevertheless, a notable distinction was observed in the behavior of W. In contrast to prior studies [45],where W was found to segregate as a coexisting element within grain boundary precipitates and was soluble within the grain matrix, in the current investigation, W was observed to segregate exclusively as large W-rich precipitates, which were spatially isolated without the accompaniment of other precipitates in their vicinity. Additionally, no trace of W was observed within the grains themselves.

6. Atomic scale investigations of melting point and the effect of Cr and Al content on the tensile properties of FeCrAl system

1. Introduction

As pointed out earlier, multiscale modeling and simulation is an efficient way to complement experiments and in-reactor testing for a better understanding of FeCrAl [142]. Molecular dynamics has proven to be a valuable tool that can provide insight into fundamental properties and elucidate critical mechanisms of materials [143-148]. Despite the interest in FeCrAl, relatively little work has been performed on the atomistic scale. There are currently only two interatomic potentials available for the FeCrAl system. Liu et al. [108] developed the first interatomic potential for the FeCrAl system in 2019, which predicted the phase stability region for FeCrAl ferrite alloys. However, this potential had some shortcomings related to the defect and thermodynamic properties of FeCrAl alloys. To address these, Liao et al. [106] developed the most recent interatomic potential in 2020, which accurately captures microstructural changes in FeCrAl under various conditions, including irradiation. Due to its recent development, only a few studies have used the Liao potential, mainly focusing on radiation damage [42, 149, 150], creep [150-152], and dislocation mechanics [149, 153, 154]. There are two studies which focused on the mechanical properties of FeCrAl alloys. Dai et al. [41] explored the effects of Cr and Al concentration and radiation defects on the elastic properties of FeCrAl alloy, while Ye et al. [155] studied the uniaxial tensile property of the single-crystal FeCrAl system. No studies have investigated the influence of Cr and Al content on the mechanical properties of FeCrAl.

This study uses molecular dynamics simulations to address the lack of knowledge on the impact of FeCrAl composition on its mechanical properties. An extensive validation of the chosen interatomic potential is performed, verifying the reproducibility of the previously reported results,

and determining the melting point. Subsequently, a series of tensile tests are performed to analyze related mechanical properties for a variety of compositions. The results highlight the significant impact of strain rate and temperature on the prediction of the alloy's ultimate tensile strength.

2. Methodology

In the present research, we employed the Large-scale Atomic/Molecular Massively Parallel Simulator (LAMMPS) for molecular dynamics (MD) simulations [156]. LAMMPS is an open-source code that supports classical molecular dynamics simulations, and it is renowned for its ability to scale across numerous processors. The backbone of molecular dynamics simulations lies in the careful selection of interatomic potentials, which are critical in defining the interactions between atoms. Further details are elaborated in Chapter Three. The precision of the computational experiment results is directly influenced by the quality of these interatomic potentials. In metallic systems, the Embedded Atom Method (EAM) formalism serves as one of the most common descriptors, encapsulating not only pair interactions but also accounting for the impact of the surrounding electron density [105]. In the case of the FeCrAl ternary system, only two EAM interatomic potentials are known – Liu et al. [108] EAM potential and Liao et al. [106] EAM potential. Liu et al. EAM potential exhibited certain shortcomings in capturing defects and thermodynamic properties of FeCrAl alloys. For instance, it underestimated the formation energies of vacancies and the stacking fault energy compared to values obtained from *ab initio* calculations in pure Al. To address the limitations of the Liu et al. potential, Liao et al. developed a new potential aiming to accurately depict the microstructural features in FeCrAl under various conditions, including irradiation, a critical characteristic of the nuclear environment. In the present study, the Liao EAM potential was utilized to capture the detailed atomistic interactions and

behavior. A version of the interatomic file, designed to be compatible with the LAMMPS software, was procured directly from the original authors of the Liao EAM potential.

Simulations of lattice parameter and ground-state energy were conducted using two distinct approaches. The initial approach made use of an NPT ensemble with a Nose-Hoover thermostat and barostat to enable system relaxation at 300 K and find the relaxed lattice parameter. The canonical ensemble (NVT) was employed in the second approach, where simulations were carried out at different lattice parameters. The single-phase method [157] utilized for simulations of melting phenomena began from a rectangular parallelepiped supercell (28.4 Å × 28.4 Å × 28.4 Å) with periodic boundary conditions and containing 2,000 atoms. This computational experiment can be divided into two steps, heating, and cooling. The supercell was first relaxed at 300 K in an NPT ensemble to regulate temperature and pressure. After reaching equilibrium, the system was heated by increasing the temperature from 300 K to 2500 K (far beyond the estimated melting point) over 4 ns with a heating rate of 5.5×10^{11} K/s, after which the system was equilibrated at 2500 K. Finally, the supercell temperature was decreased over 25 ns with a cooling rate of 8.8×10^{10} K/s from 2500 K to 300 K. The simulation time for the cooling process is much longer than heating process to achieve a cooling rate lower than the critical cooling rate required for the crystallization process [157, 158]. The two-phase method [157] utilized for simulations of melting phenomena began with an initial crystalline FeCrAl supercell in rectangular parallelepiped (56.8 Å × 56.8 Å × 113.6 Å) with periodic boundary conditions containing 32,000 atoms. The supercell is geometrically divided into two imaginary regions with the same volume and number of atoms along the Z axis: the upper and lower regions. The whole supercell is first equilibrated in an NPT ensemble at 1350 K. The 1350 K temperature was chosen as it is close to, but below, the expected melting temperature. Then, the upper region was heated to 2100 K, a temperature higher than the

superheating temperature to ensure melting, while the lower region was kept at 1350 K. Finally, the whole supercell was allowed to equilibrate under a microcanonical ensemble (NVE) for 4 ns. The final equilibration process is long enough to ensure a completely equilibrated state.

The simulations of tensile tests on the FeCrAl alloy were executed with different compositions, temperatures, and strain rates. The system was first relaxed using the NPT ensemble at a target temperature and zero pressure. Following relaxation, the initial cell lengths were stored for future strain calculations. Then, the simulation entered the tensile testing phase, in which the system was maintained at the test temperature using the NVT ensemble, and deformation was applied in the z-direction at different strain rates. To post-process the simulation results, various analysis tools available in Ovito were employed [159] including the Common Neighbor Analysis (CNA) algorithm. The CNA algorithm was utilized to investigate the local atomic environment within the simulated system. Defect mechanics analysis techniques were employed to examine the structural deviations and identify defect sites within the simulation data. To study dislocations and their influence on the material's mechanical behavior, Ovito's dislocation analysis (DXA) [159] tools were utilized. The MD simulations were performed on the Henry2 and RDFMG high-performance computing clusters at North Carolina State University.

3. Results

3.1. Interatomic Potential Validation

To ensure an accurate implementation of the interatomic potential for complex phenomena, it must first be validated against pre-computed quantities, and then utilized to compare against known thermophysical properties, which may not have been yet determined with the interatomic potential. Thus, lattice parameters and melting temperature are determined and compared with empirical data gathered from experimental techniques, notably X-ray diffraction (XRD) tests.

Through this comparative analysis, we aimed to ascertain the accuracy and dependability of the Liao potential in representing the structural properties and thermodynamic characteristics of the FeCrAl alloy. By establishing a solid foundation for further simulations and analyses, we ensure that our investigations are built on a reliable and validated model.

3.1.1. Lattice Constant

In nature, a crystal in equilibrium is in the lowest energy configuration known as ground state. This low-energy state defines the lattice geometry and the positions of atoms within the crystal structure. The crystal geometry and lattice parameter can be identified using characterization techniques like x-ray diffraction. However, the exact locations of atoms are unknown at the start of the simulations. Starting with assigning locations of atoms based on the known phase of the material being evaluated, we can find the lowest energy configuration and the equilibrium lattice parameter. This is achieved by adjusting the atomic positions and lattice parameter until an energy minimum is found.

Fe22Cr6Al has an iron ferrite matrix and is thus in the body-centered cubic (bcc) crystal structure. Fig. 6.1 shows the relationship between the cohesive energy and the bcc lattice parameter at 300 K, obtained via NVT simulations. From the figure, it is observed that at lower lattice parameter values ($a < 2.5$), the cohesive energy exhibits decreasing trend until it reaches a minimum value denoting the ground state energy. The decay of the repulsive forces between atoms primarily causes this decrease. Beyond this point, as the lattice parameter further increases, the cohesive energy again shows an upward trend, signifying an enhancement in the attractive forces between the central atom and its surroundings. This variation in cohesive energy with lattice parameter delineates an equilibrium geometry identified by the lattice parameter corresponding to the minimum value of the cohesive energy. This value is consequently referred to as the

equilibrium lattice parameter. In our molecular dynamic simulations, the derived equilibrium lattice parameter value was found to be 2.84 Å. Comparatively, X-ray diffraction experiments conducted independently (part of this work) provided a lattice parameter measurement of 2.87 Å, a value very close to that obtained from our simulations. A significant point to consider here is that our molecular dynamics simulations were conducted on a pristine ternary system, devoid of minor elements or Mo atoms, which might influence the lattice parameter. Therefore, their absence could partially account for the minor discrepancy observed between the lattice parameter values obtained from X-ray diffraction experiments and those derived from our molecular dynamic simulations utilizing the Liao et al. potential. The agreement between the calculated lattice parameter using Liao et al.'s interatomic potential and the measured parameter using XRD demonstrates the accuracy and reliability of the interatomic potential in predicting structural properties of the FeCrAl system.

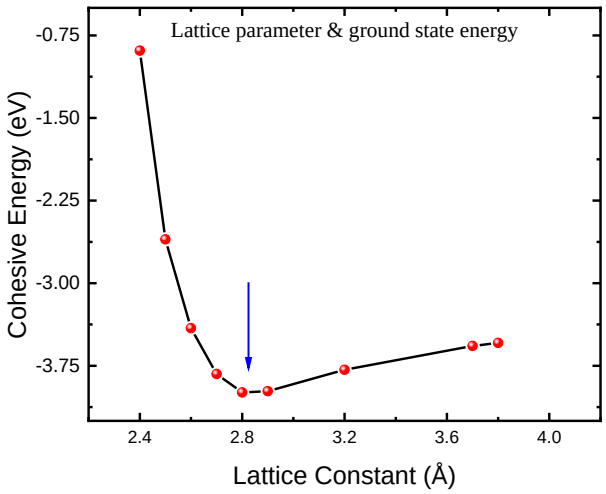

Figure 6.1. Variation of the cohesive energy with the lattice parameter in the FeCrAl system at 300 K. The blue arrow points towards the minimum point in the curve, which corresponds to the equilibrium lattice constant. At this point, the repulsion and attraction forces are balanced, and zero net force is acting on the atoms.

3.1.2. Melting Temperature

The following section covers the evaluation of the melting temperature of Fe22Cr6Al using molecular dynamics simulations. Two distinct techniques were implemented, the modified single-phase method and the two-phase method (solid/liquid Interface method). By utilizing both techniques, the melting temperature was used to verify the quality of Liao et al. potential, reproduce an important thermodynamic property and compare with experimental results.

The modified single-phase method used in molecular dynamics simulations for determining the melting point involves gradually heating a system from a solid phase to a liquid phase until it melts, and then use the equation derived by Belonoshko et al. [158] to find the melting temperature. The key parameter is the super-heating temperature or mechanical melting temperature, where a sudden change in the volume/energy occurs when a solid is heated. As there are no interfaces or defects which play a key role in the melting process, the acquired temperature is considered the mechanical melting temperature. This method is straightforward and conceptually simple, making it easy to implement. Fig. 6.2 presents the variation in the potential energy of a supercell system as a function of the increasing temperature. An abrupt step is noticeable around 2,000 K, marking the superheating point of the system. This is the point at which the system undergoes a complete phase transition, from the solid to the liquid phase.

In addition to the potential energy, (Fig. 6.3) provides an insightful portrayal of the radial distribution function at various temperatures, ranging from nearly 500 K to 2500 K. As per the analysis of (Fig. 6.3), it can be observed that the second peak, noticeable at lower temperatures, gradually diminishes and eventually disappears in all the curves beyond the superheating temperature of 2,000 K. This disappearance of the second peak in the radial distribution function is a reliable indicator of the melting process, confirming the solid-to-liquid phase transition

ascertained in (Fig. 6.1). We adopted a relation based on critical superheating as proposed by Belonoshko et al. [158], formulated as,

$$\frac{\mathrm{T}_{superheating}}{\mathrm{T}_{melting}} = \frac{\ln(2)}{3} + 1 \tag{6.1}$$

$$\frac{\ln(2)}{3} + 1 = \frac{2000\ \mathrm{K}}{\mathrm{T}_{melting}} \tag{6.2}$$

By employing this equation, the melting temperature from the modified single-phase method is approximately 1,624 K. This calculated temperature is less than the thermodynamic melting temperature, 1773 K, with an associated error margin of 8.4%.

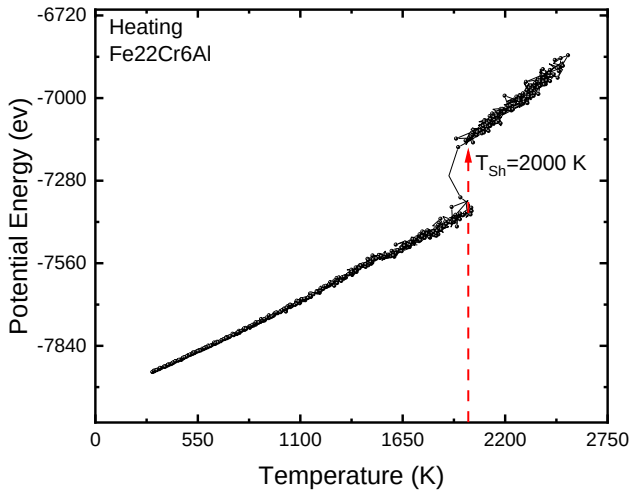

Figure 6.2. Change in potential energy with temperature in a single-phase method simulation for melting temperature determination with a notable superheating temperature around 2,000 K.

To obtain a more accurate prediction of melting point in FeCrAl, the two-phase interfacial method or solid/liquid interface method is employed. The two-phase method is based on the understanding that the boundary between the solid and liquid phases can be perceived as a defect [160] that serves as a nucleation location, reducing the critical energy necessary for the melting process to occur.

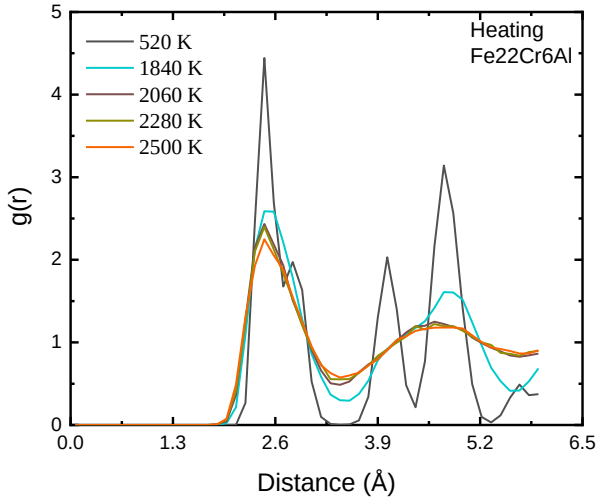

Figure 6.3. Radial Distribution Functions (RDF) at various temperatures for FeCrAl system during heating simulations in a single-phase method to determine the melting temperature. The second peak vanishes at temperatures higher than 2,000 K, which indicates a complete liquid phase.

Based on the definition of the melting temperature [160], if the solid/liquid structure completely develops into the liquid state then the temperature is higher than the melting point, and, in contrast, lower than the melting point. If the liquid/solid structure can stably exist, the temperature corresponds to the melting point.

Fig. 6.4 provides a visual representation of the progression of the two-phase melting simulation captured at three different time steps. The visualization was facilitated by the application of common neighbor analysis tools in the Ovito software [159]. Fig. 6.4a depicts the entire supercell, displaying bcc structure in a state of equilibrium at 1,350 K. After achieving this equilibrium, the lower half remained at the initial temperature of 1,350 K, whereas the upper half experienced heating up to 2,100 K (Fig. 6.4b). The resultant visualization validates the formation of a complete liquid phase in the heated upper half of the supercell. Following the NVE equilibration step, part of the lower solid phase underwent melting due to the elevated system

temperature; however, the supercell still exhibited coexisting liquid and solid phases, demonstrating the unique melting temperature features (Fig. 6.4c).

In an alternative simulation run, the temperature in the lower region was elevated to 1,450 K resulting in an average system temperature of approximately 1,900 K. At this elevated temperature, the entire system underwent a phase transition to a liquid state by the conclusion of the final NVE equilibration step. This observation substantiates that the melting temperature of the system is 1,850 K. The determination of melting temperature using this two-phase method (1850 K) aligns remarkably well with the experimental melting temperature, exhibiting a mere 4.3% error margin. This harmony validates the efficacy of using the Liao potential for predicting melting temperature. Moreover, it corroborates the stability and precision of Liao potential when exposed to elevated temperatures.

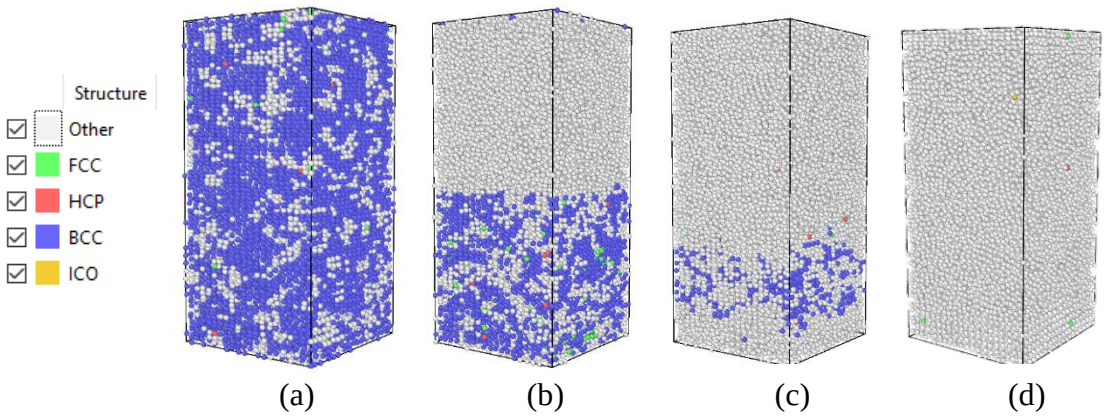

Figure 6.4. OVITO visualization of two-phase method for melting temperature calculations in FeCrAl system. (a) Depicts the supercell at equilibrium at 1,350 K; (b) Highlights the upper region at a melted state of 2,100 K and lower region at 1,350 K; (c) Shows the equilibrated final supercell at 1,850 K and (d) Shows the equilibrated final supercell at 1,900 K.

3.2. Tensile Testing

3.2.1. Sensitivity to system size

First, we performed supercell size convergence studies to ascertain the impact of the number of atoms within the simulation on the derived tensile properties. The parameters varied across a spectrum, from a modest 48k atoms up to an extensive half-million atom count, thus facilitating an understanding of the effects of atom count on computational tensile tests. Fig. 6.5 shows the engineering stress-strain curve obtained under a strain rate of 0.1 Ps^{-1}. As evident from the figure, the resultant curves generated from varying atom counts exhibit effectively no differences. This observation underscores a vital finding that the number of atoms within the defined range does not have a significant effect on the resulting stress-strain characteristics of the computational model at the stated strain rate.

To ascertain the robustness of our results, we replicated the same tests under a reduced strain rate, specifically at 0.0001 Ps^{-1}. This step was undertaken to capture any subtle variations induced by the change in the kinetics of the system. Fig. 6.6 represents the engineering stress-strain curves obtained at this lower strain rate. Once again, the curves across different atom counts were almost identical, reaffirming our previous conclusions. However, we observed minor deviations in the fracture strain, which could be attributed to the varying atom count and possibly different kinetics under the slower strain rate. Notably, the stress-strain curve representing the largest atom count in our study, the 584k atoms, was prematurely truncated before the onset of failure due to computational limitations. These constraints emphasize the need to strike a balance between accuracy and computational feasibility when selecting the appropriate atom count for future simulations. All subsequent calculations are performed using a 162k atom supercell.

3.2.2. Effect of Strain Rate and Temperature

Molecular dynamics simulations were conducted on a supercell of Fe22Cr6Al composition with 162k atoms to probe the effect of varying strain rates and temperatures on the ultimate tensile strength (UTS). The strain rates spanned a broad range from 10^{-5} to 0.1 Ps^{-1}, and the temperature varied from 500 K to 1000 K. The initial exploration focused on assessing the influence of strain rate on the UTS at a constant temperature of 500 K. Fig. 6.7 portrays a computational tensile test conducted using the stated supercell at a strain rate of 0.001 Ps^{-1} and 500 K. The color spectrum of the supercell reflects the shear strain internal to the cell, with a yellow hue intensifying as shear strain increases.

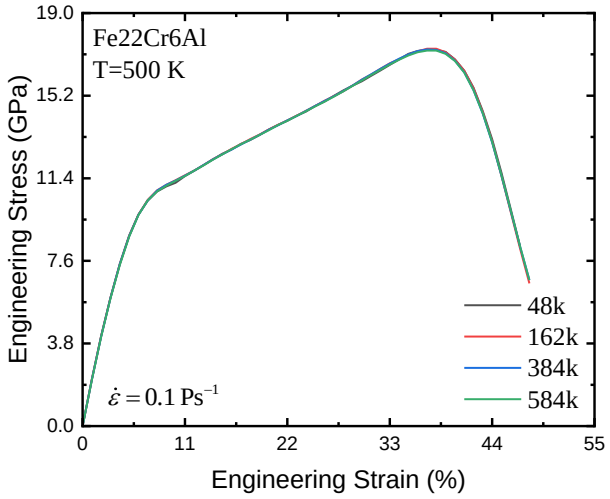

Figure 6.5. Engineering stress-strain curve of Fe22Cr6Al system at 500 K with different atom counts, under a strain rate of 0.1 Ps^{-1}, illustrating identical stress-strain curve at all atom counts.

As strain continues, Fig. 6.7 demonstrates the emergence of voids at the center of the supercell and the eventual fracture behavior, characterized by a dimpled fracture surface, indicative of ductile fracture. Fig. 6.8 provides a visual comparison of the engineering stress-strain curves obtained at different strain rates at 500 K.

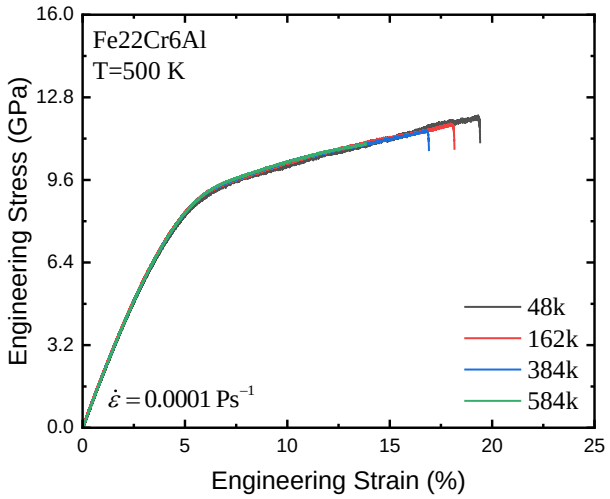

Figure 6.6. Engineering stress-strain curve of Fe22Cr6Al system at 500 K with different atom counts, under a strain rate of 0.0001 Ps^{-1}, illustrating identical mechanical response despite the atom count except for the final fracture strain.

A clear correlation between the UTS and the strain rate is depicted in (Fig. 6.9), presenting two distinct linear regions with different slopes. The slope represents the strain rate sensitivity of the system at the test temperature, mainly influenced by dislocations. The change in slope suggests a variation in dislocation density/activity between low and high strain rates. At low strain rates, dislocations have more time to annihilate or relax into energetically favorable states. Conversely, at high strain rates, dislocations have less time to annihilate, leading to a higher likelihood of survival and increased density. This increased density of dislocations contributes to a higher strain rate sensitivity.

Two distinct deformation mechanisms were identified during these tests. Fig. 6.10, obtained through the defect mechanics analysis algorithm in the Ovito software, shows that at the lower tested strain rates (0.00001 Ps^{-1}), small defects start forming at the initial steps within the supercell. As the engineering strain increased, these defects grew in density and size until fracture occurred. The second deformation mechanism was revealed in a 0.0001 Ps^{-1} strain rate test through

the dislocation analysis algorithm in the Ovito software, shown in (Fig. 6.11). This image displays the evolution of voids of different sizes along with dislocation lines spread across the supercell. Over time, these dislocation lines evolved into dislocation loops, which are thermodynamically more favorable.

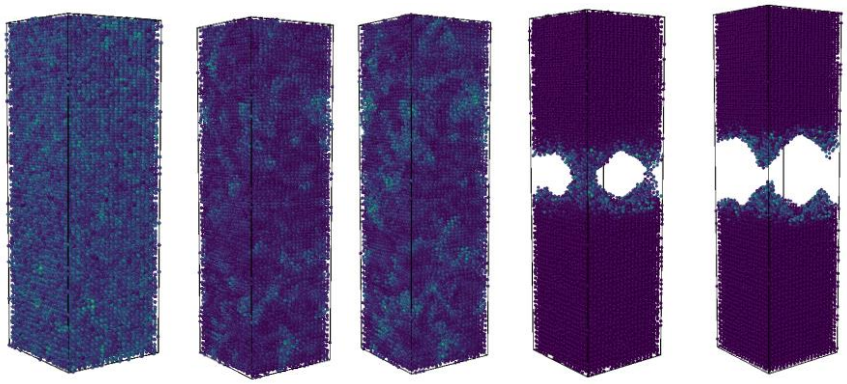

Figure 6.7. Time-stepped OVITO visualization of tensile test in FeCrAl system from initial perfect supercell to final fracture geometry, illustrating the evolution of material deformation. The final fracture surface is a dimpled like surface. The yellow hue intensifies as shear strain increases.

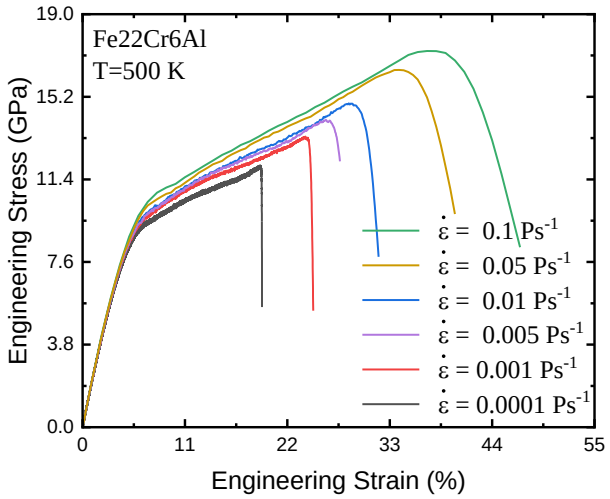

Figure 6.8. Engineering stress-strain curves for Fe22Cr6Al supercell at 500 K, demonstrating the influence of varied strain rates on deformation behavior. Increasing the strain rate increases the ultimate tensile strength.

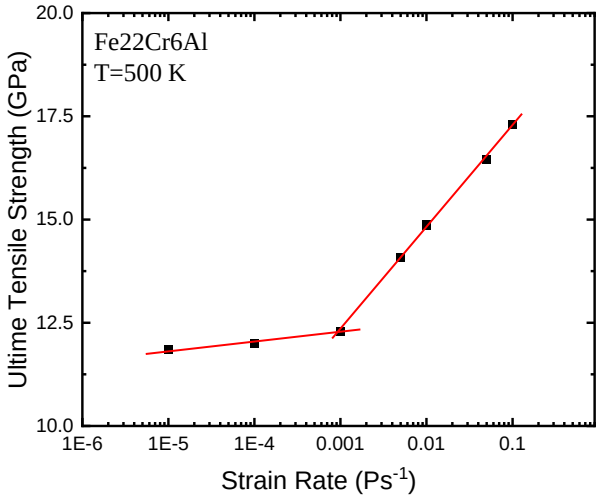

Figure 6.9. Influence of strain rate on ultimate tensile strength of Fe22Cr6Al Supercell at 500 K, illustrating the strain-rate sensitivity of the material.

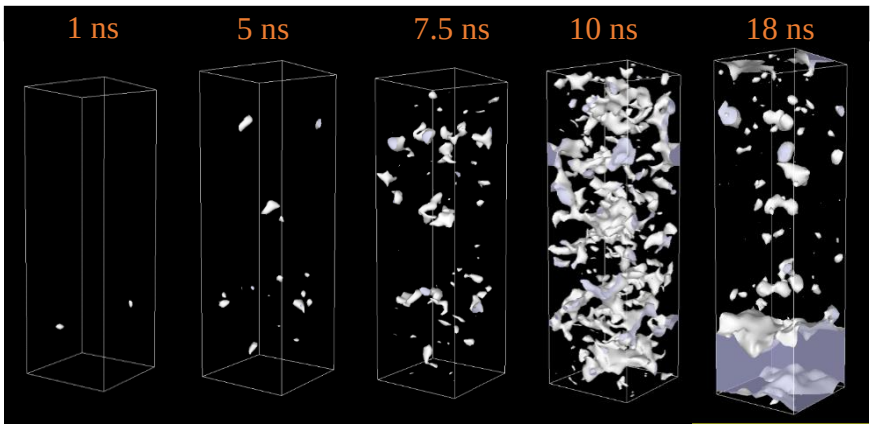

Figure 6.10. Ovito visualization of defect evolution during tensile test of Fe22Cr6Al Supercell at 500 K and 0.00001 Ps^{-1} strain rate, leveraging defects and dislocations analysis algorithm to track defects and dislocations progression over time. Starting with almost clean super cell, defects start to generate with deformation till the final fracture.

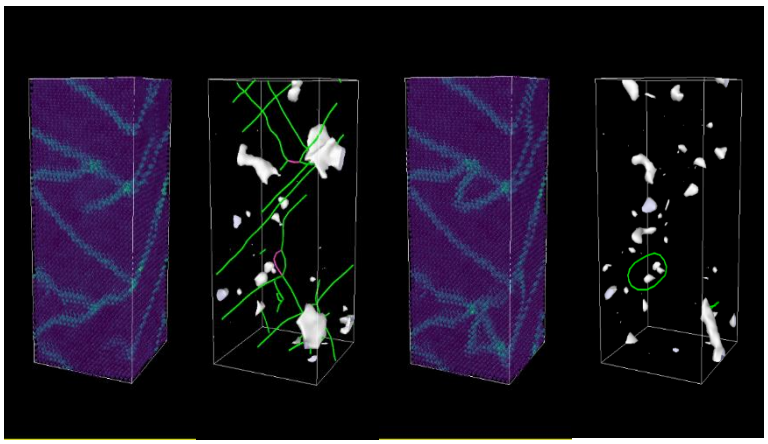

Figure 6.11. Ovito visualization of tensile test of Fe22Cr6Al supercell at 500 K and 0.0001 Ps^{-1} strain rate, utilizing defect mechanics and dislocation analysis algorithms to monitor defect evolution and dislocation formation (represented as green lines and loops).

Finally, we examined the combined effects of both strain rate and temperature on the UTS. The results of this analysis are portrayed in (Fig. 6.12), a color map illustrating how UTS changes with varying strain rates and temperatures. The map reveals extremes: the highest UTS was recorded under high strain rates and low temperatures, while the lowest UTS occurred under low strain rates and elevated temperatures. An intermediate region with intermediate UTS values exists between these two extremes.

3.2.3. Effect of Cr and Al Content

A comprehensive set of tensile molecular dynamic simulations [161-164] was performed on a single crystal supercell of FeCrAl to investigate the impact of alterations in Cr and Al content on its tensile properties. The simulations comprised 162k atoms with a strain rate of 0.001 Ps^{-1} and a temperature of 800 K. These simulations were performed across a wide range of Al content (2-8 at. %) and Cr content (12-22 at. %), aiming to understand the overlapping influence of changing Cr and Al content on the tensile attributes of the FeCrAl alloy.

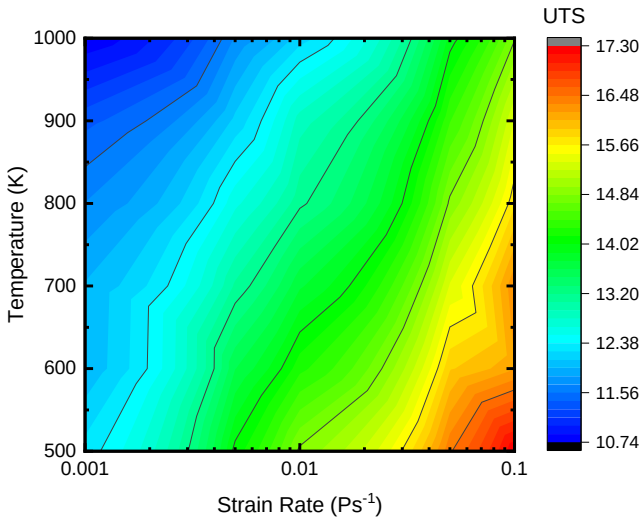

Figure 6.12. Color map illustrating the variation of ultimate tensile stress in response to changes in strain rate and temperature. The highest UTS was recorded under high strain rates and low temperatures, while the lowest UTS occurred under low strain rates and h high temperatures.

The simulation results are presented in color maps, providing an accessible visual representation of the relationships between Cr and Al content and their effect on the tensile characteristics of the supercell. The ductility was measured up to the UTS point, while stress was analyzed at 7.5% strain, which lies near the boundary of the elastic and plastic regions. Fig. 6.13 demonstrates the variations in ductility as a function of changing Cr and Al content. It reveals a trend of declining ductility with increasing Al and Cr content.

A distinct region of high ductility emerges around 18 at. % Cr. The maximum ductility values were found in supercells with 18 at. % Cr and (2-3 at. %) Al content. An additional area of relatively high ductility is found in the context of low Cr and Al content. In addition to that, high Cr and Al combination yielded low ductility values compared to the rest of the map. Fig. 6.14 offers a closer look at how the tensile stress varies with Cr and Al content at 7.5% strain. This color map reveals that low Cr and Al content correspond to high tensile strength values compared to regions with high Cr and Al content. An intermediate region is also observed, exhibiting median

tensile strength values. Regarding the influence of Cr content on ductility at the same Al content, the color map can be divided into three regions.

The first region occurs at Al content below 4 at. %, where ductility changes substantially with increasing Cr content with a peak at 18 at. % Cr. The second/middle region lies between 4-6 at. % Al, where ductility remains constant with varying Cr content. The third region encompasses Al content beyond 6 at. %, exhibiting the lowest ductility values as Cr content increases. Fig. 6.15. presents the change in ductility with the Cr content in a 2D plot for easier visualization highlighting the maximum ductility value. Based on these findings, the range of 18 at. % Cr and 1-3 at. % Al yields the maximum ductility, while the range of 4-5 at. % Al provides intermediate and stable ductility values with changing Cr content. These results outlining the ductility trend in the FeCrAl system with varying compositions can aid in optimizing alloy composition.

The change in ductility with increasing Al content is minimal at higher Cr content (20 at. % Cr and beyond). For alloys with Cr content below 20 at. %, altering the Al content significantly affects ductility. For example, at 18 at. % Cr, increasing the Al content dramatically decreases ductility. From 15-16 at. % Cr, the change in ductility with varying Al content is nearly negligible. Fig. 6.16 presents another way to visualize the data in a 2D plot where a clear trend of decreasing ductility with increasing the Al content is observed despite the Cr content. This information is valuable for alloy design, as it allows for the study of the effect of other elements on the ductility of FeCrAl system within this range of Cr content.

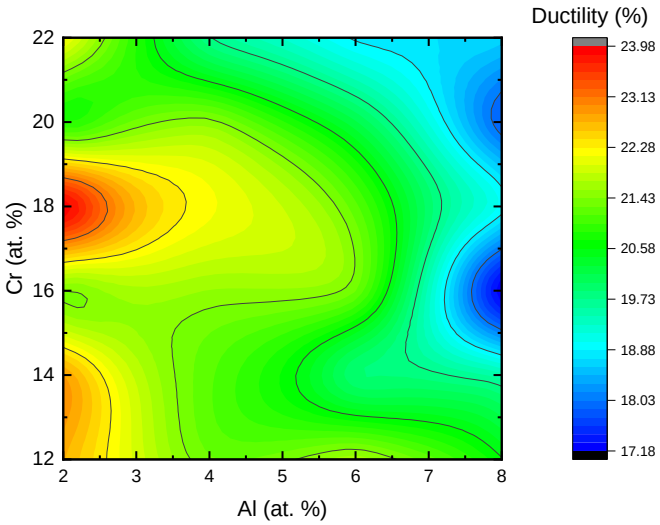

Figure 6.13. Color map depicting the variation of ductility up to ultimate tensile strength in relation to changes in Cr and Al content. It reveals a trend of declining ductility with increasing Al and Cr content with a high ductility island at 18 at. % Cr.

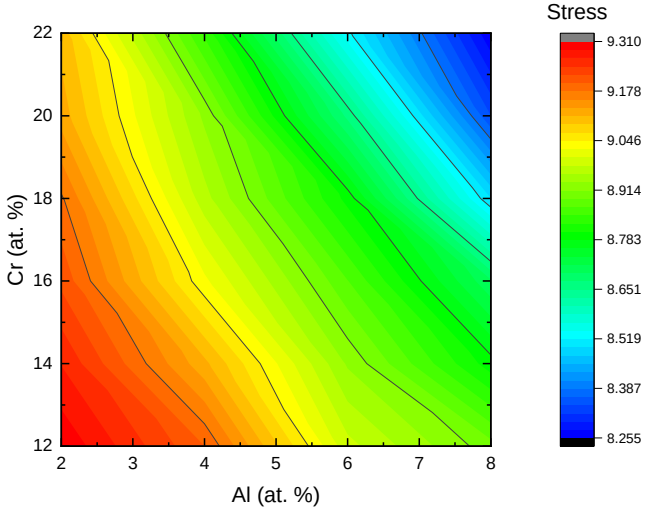

Figure 6.14. Color map demonstrating the variation of tensile strength at 7.5% engineering strain, corresponding to changes in Cr and Al content. The stress decreases with increasing the Al and Cr content.

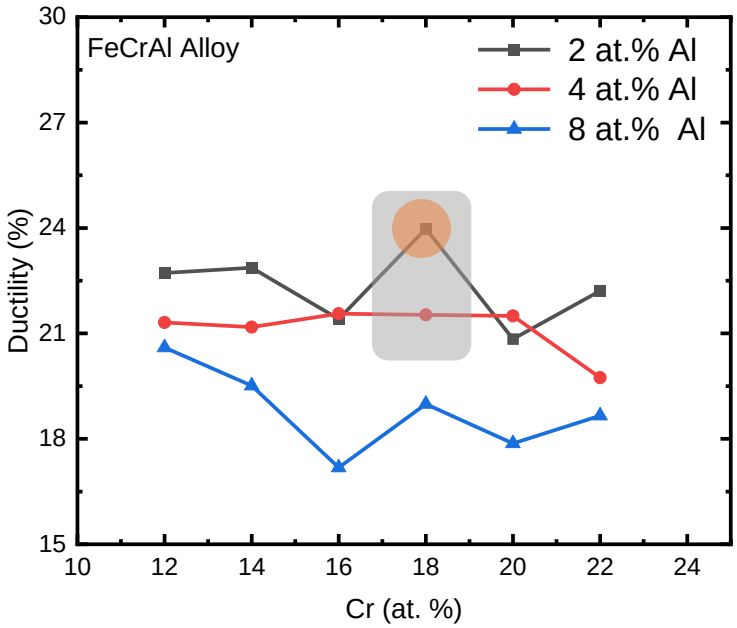

Figure 6.15. 2D plot of the change in ductility with varying Cr content with peak ductility value at 18 at. % Cr and 2 at. % Al.

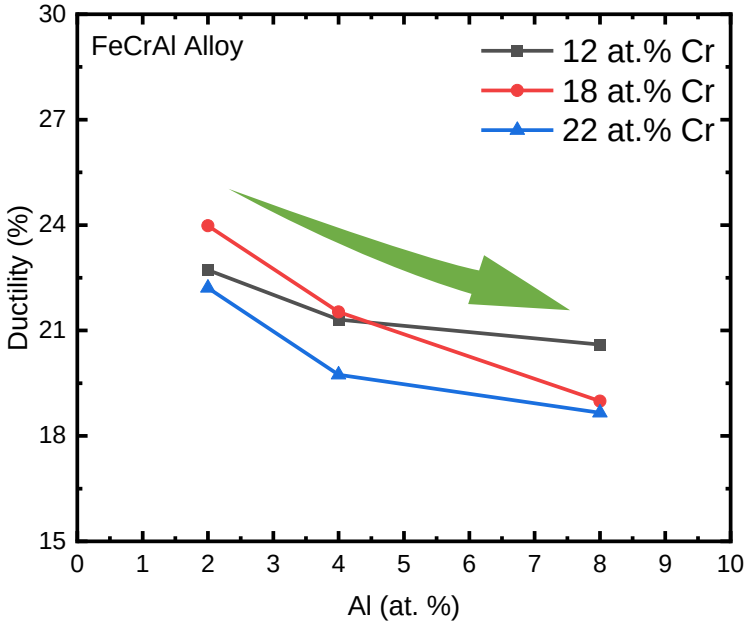

Figure 6.16. 2D plot of the change of ductility with increasing Al content in the matrix. A clear decreasing ductility trend with increasing the Al content is observed despite the Cr at. %.

Conclusions and Outlook

Conclusions

This thesis undertakes an exploration of the creep behavior and mechanical properties of high Cr-containing FeCrAl Advanced Powder Metallurgy Tubing (APMT) alloy and 14YWT alloy. The findings yield insights into the alloys' creep behavior, the underlying deformation mechanisms, the microstructures before and after creep, and the impact of alloying elements on the ductility.

APMT study investigated the creep behavior at temperatures and stresses relevant to ATF concept, which is gaining increasing importance in the field of advanced materials research. The observed creep behavior revealed a transition between three regions with a high stress-exponent region for all temperatures at high stresses. The first region was characterized by dislocation viscous glide with a stress-exponent equal to (n_I) = 2.8 and activation energy (Q_I) of 252.7 kJ/mol. The second region has a stress exponent equal to (n_{II}) ~ 7.45 and a high activation energy, (Q_{II}) of 576 kJ/mol. In addition, the third region has a high stress exponent (n_{III}) with an average of 14.4 and high activation energy (Q_{III}) of 737.97±18.7 kJ/mol.

The threshold stress approach was employed to determine the dominant creep mechanism at the upper range of the examined stresses. Based on this analysis, dislocations climb over precipitates facilitated by the increase in dislocation line length was found to be the creep rate-controlling mechanism at higher stresses, with a stress exponent of 6 and an activation energy of 252.8 ± 20.0 kJ/mol. The rate-controlling mechanism based on modified Bird-Mukherjee-Dorn (BMD) equation in APMT alloy at high stresses and the investigated temperatures was determined to be the dislocations climb with a stress exponent equal to 6.

Microstructural characterization of the APMT alloy provided preliminary evidence of the formation of (Cr, Mo)-rich carbides at the grain boundaries. The segregation observed might assist in locking the grain boundaries from sliding, thereby augmenting the overall strength of the material.

The 14YWT-NFA1 study revealed a transition between two distinct creep regions. The stress exponent n, observed to be approximately one in the low stress region, coupled with the activation energy Q = 244.58 kJ/mol, suggesting the dominance of a Nabarro-Herring lattice diffusion-controlled creep mechanism at lower stresses. In the high stress region, however, we observed a stress exponent of around 15 and an activation energy Q of 388.56 kJ/mol highlighting the role of precipitates as dislocation barriers in the high-stress conditions.

BF-TEM images revealed that the grain structure remained stable even under prolonged high-stress creep tests. This stability is potentially due to the presence of precipitates along the grain boundaries, which may hinder diffusion and consequently limit grain growth. Another observation was the existence of two distinct types of precipitates, W-rich and Y-Ti-O rich, which never co-occurred on the same grain boundary in the characterized area. The TEM-EDS maps for W after creep tests demonstrated concentrated localizations at the grain boundaries with no signs of W inside the grains. A noteworthy aspect was the observed size difference between the two types of precipitates, namely W-rich precipitates are larger than Y-Ti-O precipitates.

While the findings herein reveal that the 14YWT-NFA1 alloy exhibits substantial mechanical strength, particularly in terms of creep resistance, at elevated temperatures, there are inherent microstructural deficiencies that could potentially undermine its suitability for deployment as a nuclear structural material. The presence of voids and micro-cracks in the alloy's as-received condition introduces the risk of unpredictable and premature fracture. Therefore,

comprehensive understanding and mitigation strategies of these microstructural defects is critical for effective application of the 14YWT-NFA1 alloy in nuclear environments.

Systematic molecular dynamic investigation presented in this work analyzed the effect of varying Cr and Al content on the mechanical properties of a FeCrAl alloy. The analysis process started by verifying the reliability and accuracy of the interatomic potential used for the simulations accomplished through a series of tests, including lattice parameter calculations, and both single and two-phase melting methods.

The study then moved onto an investigation of the tensile properties of FeCrAl. The impact of the supercell size on the mechanical properties was studied, leading to the conclusion that within the investigated range, the size did not significantly alter the tensile properties of the system. A detailed investigation was conducted to understand the effects of strain rate and temperature on the UTS of the FeCrAl supercell. It was concluded that both strain rate and temperature significantly affect the UTS of the material.

Finally, a comprehensive analysis of the impact of varying the Cr and Al content on the tensile properties of the FeCrAl supercell was conducted. It was found that while the tensile strength was generally higher for lower Cr and Al content, a local compositional space with a Cr content of 18 at. % showed improved ductility, although the Al content needs to be controlled carefully as it was observed to decrease ductility with increasing content. In the light of these findings, the maximum ductility values were found in supercells with 18 at. % Cr and (2-3 at. %) Al content. However, this conclusion calls for further experimental work to substantiate these findings.

Outlook

Based on current findings, there are several areas of potential future investigation that may shed further light on the mechanics and behaviors of these alloys. In the first study on the creep behavior of APMT alloy, in-situ TEM creep testing could provide valuable real-time insights into the dislocation activity during creep deformation of the APMT alloy.

The second study on the 14YWT-NFA1 alloy has opened some avenues for further exploration. The discovery of two types of precipitates that never co-occur on the same grain boundary could indicate certain inherent limitations in the fabrication method or compositional variations within the same ingot. More detailed investigation into these precipitates could lead to enhanced understanding of their formation and their impact on the creep behavior of the alloy. Also, while the present study has revealed significant insights into the high-stress creep behavior of this alloy, a deeper exploration using the threshold stress approach could provide additional valuable information, although it necessitates more results at varied temperatures.

In the molecular dynamic simulation study, it would be beneficial to validate the findings of the molecular dynamics simulations through experimental work. Further exploration of the interplay between strain rate and temperature on the ultimate tensile strength of the FeCrAl alloy could provide more understandings of how these factors control the alloy's behavior. Moreover, while the study found that a specific composition range yielded maximum ductility, additional investigations to verify these results in real-world settings are necessary. Also, exploring the possibility of other combinations of Cr and Al, as well as the inclusion of other elements, could lead to the development of FeCrAl alloys with even better mechanical properties.

Lastly, the observed stability of the 14YWT-NFA1 alloy under prolonged high-stress conditions, potentially due to precipitates hindering grain boundary diffusion, warrants a more in-

depth examination. This could be accomplished through the study of diffusion mechanisms and the role of precipitates in other alloy systems or at different temperatures and stress conditions. Similarly, understanding how the two distinct types of precipitates interact with dislocations, and whether this interaction can be manipulated to improve mechanical properties, would be a valuable. These investigations will not only enhance the understanding of the studied alloys but may also contribute to the development of new alloys with improved performance in various applications.

References

1. Basu, D., V.W. Miroshnik, D. Basu, and V.W. Miroshnik, *Advantages of Nuclear Power*. The Political Economy of Nuclear Energy: Prospects and Retrospect, 2019: p. 7-21.
2. Zinkle, S.J. and G. Was, *Materials challenges in nuclear energy.* Acta Materialia, 2013. **61**(3): p. 735-758.
3. Cameron, I.R., *Nuclear fission reactors*. 2012: Springer Science & Business Media.
4. Ehrlich, K., *Materials research towards a fusion reactor.* Fusion Engineering and design, 2001. **56**: p. 71-82.
5. Holt, M., R.J. Campbell, and M.B. Nikitin, *Fukushima nuclear disaster*. 2012, Congressional Research Service Washington, DC, USA.
6. Little, E., *Development of radiation resistant materials for advanced nuclear power plant.* Materials Science and Technology, 2006. **22**(5): p. 491-518.
7. Chant, I. and K.L. Murty, *Structural materials issues for the next generation fission reactors.* JOM, 2010. **62**(9): p. 67-74.
8. Schneibel, J.H., C.T. Liu, M.K. Miller, M.J. Mills, P. Sarosi, M. Heilmaier, and D. Sturm, *Ultrafine-grained nanocluster-strengthened alloys with unusually high creep strength.* Scripta Materialia, 2009. **61**(8): p. 793-796.
9. Murty, K.L. and I. Charit, *An introduction to nuclear materials: fundamentals and applications*. 2013: John Wiley & Sons.
10. Zinkle, S.J., K.A. Terrani, J.C. Gehin, L.J. Ott, and L.L. Snead, *Accident tolerant fuels for LWRs: A perspective.* Journal of Nuclear Materials, 2014. **448**(1-3): p. 374-379.
11. Charit, I., *Accident tolerant nuclear fuels and cladding materials.* Jom, 2018. **70**(2): p. 173-175.

12. Chen, S.-L., X.-J. He, and C.-X. Yuan, *Recent studies on potential accident-tolerant fuel-cladding systems in light water reactors.* Nuclear Science and Techniques, 2020. **31**(3): p. 32.

13. Kurata, M., *Research and development methodology for practical use of accident tolerant fuel in light water reactors.* Nuclear Engineering and Technology, 2016. **48**(1): p. 26-32.

14. Pint, B.A., K.A. Terrani, Y. Yamamoto, and L.L. Snead, *Material selection for accident tolerant fuel cladding.* Metallurgical and Materials Transactions E, 2015. **2**: p. 190-196.

15. Rebak, R.B., *Alloy selection for accident tolerant fuel cladding in commercial light water reactors.* Metallurgical and Materials Transactions E, 2015. **2**: p. 197-207.

16. Rebak, R.B., *Accident-Tolerant Materials for Light Water Reactor Fuels*. 2020: Elsevier Science.

17. Terrani, K.A., *Accident tolerant fuel cladding development: Promise, status, and challenges.* Journal of Nuclear Materials, 2018. **501**: p. 13-30.

18. Oelrich, R., S. Ray, Z. Karoutas, P. Xu, J. Romero, H. Shah, E. Lahoda, and F. Boylan. *Overview of Westinghouse lead accident tolerant fuel program*. in *Water Reactor Fuel Performance Meeting, Czech Repunlic, September, Prague*. 2018.

19. Tang, C., M. Stueber, H.J. Seifert, and M. Steinbrueck, *Protective coatings on zirconium-based alloys as accident-tolerant fuel (ATF) claddings.* Corrosion reviews, 2017. **35**(3): p. 141-165.

20. Core, G., B. Curnutt, and C. Hale, *Accident tolerant fuels series 1 (ATF-1) irradiation testing FY 2017 status report*. 2017, Idaho National Lab.(INL), Idaho Falls, ID (United States).

21. Carmack, J., F. Goldner, S.M. Bragg-Sitton, and L.L. Snead, *Overview of the US DOE accident tolerant fuel development program*. 2013, Idaho National Lab.(INL), Idaho Falls, ID (United States).

22. Johnson, K., V. Ström, J. Wallenius, and D.A. Lopes, *Oxidation of accident tolerant fuel candidates.* Journal of Nuclear Science and Technology, 2017. **54**(3): p. 280-286.

23. Deck, C., G. Jacobsen, J. Sheeder, O. Gutierrez, J. Zhang, J. Stone, H. Khalifa, and C. Back, *Characterization of SiC–SiC composites for accident tolerant fuel cladding.* Journal of Nuclear Materials, 2015. **466**: p. 667-681.

24. Rebak, R.B., *Alloy Selection for Accident Tolerant Fuel Cladding in Commercial Light Water Reactors.* Metallurgical and Materials Transactions E, 2015. **2**(4): p. 197-207.

25. Sittiho, A., V. Tungala, I. Charit, and R.S. Mishra, *Microstructure, mechanical properties and strengthening mechanisms of friction stir welded Kanthal APMT™ steel.* Journal of Nuclear Materials, 2018. **509**: p. 435-444.

26. Copeland-Johnson, T.M., C.K.A. Nyamekye, S.K. Gill, L. Ecker, N. Bowler, E.A. Smith, and R.B. Rebak, *Characterization of Kanthal APMT and T91 oxidation at beyond design-basis accident temperatures.* Corrosion Science, 2020. **171**.

27. Qiu, B., J. Wang, Y. Deng, M. Wang, Y. Wu, and S.Z. Qiu, *A review on thermohydraulic and mechanical-physical properties of SiC, FeCrAl and Ti3SiC2 for ATF cladding.* Nuclear Engineering and Technology, 2020. **52**(1): p. 1-13.

28. Rebak, R.B., *Nuclear Applications of Oxide Dispersion Strengthened and Nano-Featured Alloys: An Introduction.* Jom, 2014. **66**(12): p. 2424-2426.

29. Rebak, R.B., M. Larsen, and Y.-J. Kim, *Characterization of oxides formed on iron-chromium-aluminum alloy in simulated light water reactor environments.* Corrosion Reviews, 2017. **35**(3): p. 177-188.

30. Vollmer, N., J. Bischoff, C. Delafoy, V. Rebeyrolle, J. Reed, and E. Schweitzer. *PROtect-The leading Accident Tolerant Fuel Program by FRAMATOME*. in *44th Annual Meeting of the Spanish Nuclear Society*. 2018.

31. Lin, Y., R. Fawcett, S. Desilva, D. Lutz, M. Yilmaz, P. Davis, R. Rand, P. Cantonwine, R. Rebak, and R. Dunavant, *Path Towards Industrialization of Enhanced Accident Tolerant Fuel.* Proceedings from TopFuel, 2018.

32. Guria, A. and I. Charit, *Observation of serrated flow in APMT™ steel.* Materials Letters, 2015. **160**: p. 55-57.

33. Jönsson, B., R. Berglund, J. Magnusson, P. Henning, and M. Hättestrand, *High Temperature Properties of a New Powder Metallurgical FeCrAl Alloy.* Materials Science Forum, 2004. **461-464**: p. 455-462.

34. Jönsson, B., Q. Lu, D. Chandrasekaran, R. Berglund, and F. Rave, *Oxidation and Creep Limited Lifetime of Kanthal APMT®, a Dispersion Strengthened FeCrAlMo Alloy Designed for Strength and Oxidation Resistance at High Temperatures.* Oxidation of Metals, 2012. **79**(1-2): p. 29-39.

35. Klueh, R.L., P.J. Maziasz, I.S. Kim, L. Heatherly, D.T. Hoelzer, N. Hashimoto, E.A. Kenik, and K. Miyahara, *Tensile and creep properties of an oxide dispersion-strengthened ferritic steel.* Journal of Nuclear Materials, 2002. **307-311**: p. 773-777.

36. Park, D.J., H.G. Kim, Y.I. Jung, J.H. Park, B.K. Choi, J.H. Yang, and Y.H. Koo, *Fabrication and mechanical properties of an oxide-dispersion-strengthened FeCrAl alloy.* Fusion Engineering and Design, 2019. **139**: p. 81-85.

37. Pimentel, G., C. Capdevila, M.J. Bartolomé, J. Chao, M. Serrano, A. García-Junceda, M. Campos, J.M. Torralba, and J. Aldazábal, *Advanced FeCrAl ODS steels for high-temperature structural applications in energy generation systems.* Revista de Metalurgia, 2012. **48**(4): p. 303-316.

38. Pint, B.A., S. Dryepondt, K.A. Unocic, and D.T. Hoelzer, *Development of ODS FeCrAl for Compatibility in Fusion and Fission Energy Applications.* Jom, 2014. **66**(12): p. 2458-2466.

39. Huang, S., E. Dolley, K. An, D. Yu, C. Crawford, M.A. Othon, I. Spinelli, M.P. Knussman, and R.B. Rebak, *Microstructure and tensile behavior of powder metallurgy FeCrAl accident tolerant fuel cladding.* Journal of Nuclear Materials, 2022. **560**: p. 153524.

40. Field, K.G., M.A. Snead, Y. Yamamoto, and K.A. Terrani, *Handbook on the Material Properties of FeCrAl Alloys for Nuclear Power Production Applications (FY18 Version: Revision 1)*. 2018, Oak Ridge National Lab.(ORNL), Oak Ridge, TN (United States).

41. Dai, H., M. Yu, Y. Dong, W. Setyawan, N. Gao, and X. Wang, *Effect of Cr and Al on Elastic Constants of FeCrAl Alloys Investigated by Molecular Dynamics Method.* Metals, 2022. **12**(4).

42. Massey, C.P., D. Zhang, S.A. Briggs, P.D. Edmondson, Y. Yamamoto, M.N. Gussev, and K.G. Field, *Deconvoluting the Effect of Chromium and Aluminum on the Radiation Response of Wrought FeCrAl Alloys After Low-Dose Neutron Irradiation.* Journal of Nuclear Materials, 2021. **549**.

43. Zhang, Y., H. Sun, H. Wang, X. Wang, X. An, and K. He, *Effects of Cr element on the crystal structure, microstructure, and mechanical properties of FeCrAl alloys.* Materials Science and Engineering: A, 2021. **826**.

44. Unocic, K.A., Y. Yamamoto, and B.A. Pint, *Effect of Al and Cr Content on Air and Steam Oxidation of FeCrAl Alloys and Commercial APMT Alloy.* Oxidation of Metals, 2017. **87**(3-4): p. 431-441.

45. Bentley, J., D.T. Hoelzer, D.W. Coffey, and K.A. Yarborough, *EFTEM and Spectrum Imaging of Mechanically Alloyed Oxide-Dispersion-Strengthened 12YWT and 14YWT Ferritic Steels.* Microscopy and Microanalysis, 2004. **10**(S02): p. 662-663.

46. Klueh, R.L., J.P. Shingledecker, R.W. Swindeman, and D.T. Hoelzer, *Oxide dispersion-strengthened steels: A comparison of some commercial and experimental alloys.* Journal of Nuclear Materials, 2005. **341**(2-3): p. 103-114.

47. Miller, M., C. Fu, C. Liu, D. Hoelzer, and K. Russell. *Nanoclustering in a MA/ODS ferritic alloy*. in *2006 19th International Vacuum Nanoelectronics Conference*. 2006. IEEE.

48. Miller, M.K., K.F. Russell, and D.T. Hoelzer, *Characterization of precipitates in MA/ODS ferritic alloys.* Journal of Nuclear Materials, 2006. **351**(1-3): p. 261-268.

49. Hoelzer, D.T., *Summary of Previous Mechanical Test Data on ODS Alloys 14YWT and OFRAC up to 1000ºC*. 2021, Oak Ridge National Lab.(ORNL), Oak Ridge, TN (United States); USDOE ….

50. Kim, J.H., T.S. Byun, and D.T. Hoelzer, *Tensile fracture characteristics of nanostructured ferritic alloy 14YWT.* Journal of Nuclear Materials, 2010. **407**(3): p. 143-150.

51. Schneibel, J.H., M. Heilmaier, W. Blum, G. Hasemann, and T. Shanmugasundaram, *Temperature dependence of the strength of fine- and ultrafine-grained materials.* Acta Materialia, 2011. **59**(3): p. 1300-1308.

52. Singh, R., J.H. Schneibel, S. Divinski, and G. Wilde, *Grain boundary diffusion of Fe in ultrafine-grained nanocluster-strengthened ferritic steel.* Acta Materialia, 2011. **59**(4): p. 1346-1353.

53. Susila, P., D. Sturm, M. Heilmaier, B.S. Murty, and V. Subramanya Sarma, *Effect of yttria particle size on the microstructure and compression creep properties of nanostructured oxide dispersion strengthened ferritic (Fe–12Cr–2W–0.5Y2O3) alloy.* Materials Science and Engineering: A, 2011. **528**(13-14): p. 4579-4584.

54. Yin, W., *Creep and high-temperature deformation in nanostructured metals and alloys*, in *Nanostructured Metals and Alloys*. 2011. p. 594-611.

55. Aydogan, E., S.A. Maloy, O. Anderoglu, C. Sun, J.G. Gigax, L. Shao, F.A. Garner, I.E. Anderson, and J.J. Lewandowski, *Effect of tube processing methods on microstructure, mechanical properties and irradiation response of 14YWT nanostructured ferritic alloys.* Acta Materialia, 2017. **134**: p. 116-127.

56. Hoelzer, D.T., K.A. Unocic, M.A. Sokolov, and T.S. Byun, *Influence of processing on the microstructure and mechanical properties of 14YWT.* Journal of Nuclear Materials, 2016. **471**: p. 251-265.

57. Tan, L., T. Graening, X. Hu, W. Zhong, Y. Yang, S.J. Zinkle, and Y. Katoh, *Effects of carbonitrides and carbides on microstructure and properties of castable nanostructured alloys.* Journal of Nuclear Materials, 2020. **540**.

58. Tan, L., D.T. Hoelzer, and J.T. Busby, *Microstructure and basic mechanical properties of the procured advanced alloys for the advanced radiation resistant materials program.* ORNL/TM-2014/439, September, 2014. **22**.

59. Lo, K.H., C.H. Shek, and J. Lai, *Recent developments in stainless steels.* Materials Science and Engineering: R: Reports, 2009. **65**(4-6): p. 39-104.

60. McGuire, M.F., *Stainless steels for design engineers*. 2008: Asm International.

61. Sourmail, T., *Precipitation in creep resistant austenitic stainless steels.* Materials science and technology, 2001. **17**(1): p. 1-14.

62. AF, P. and R. PR, *Decomposition of austenite in austenitic stainless steels.* ISIJ international, 2002. **42**(4): p. 325-327.

63. Zhou, Y., Y. Li, Y. Liu, Q. Guo, C. Liu, L. Yu, C. Li, and H. Li, *Precipitation behavior of type 347H heat-resistant austenitic steel during long-term high-temperature aging.* Journal of Materials Research, 2015. **30**(23): p. 3642-3652.

64. Marshall, P., *Austenitic stainless steels: microstructure and mechanical properties.* 1984.

65. Vodárek, V., *Creep behaviour and microstructural evolution in AISI 316LN+ Nb steels at 650 C.* Materials Science and Engineering: A, 2011. **528**(12): p. 4232-4238.

66. Adamson, J. and J. Martin. *Effect of niobium content on the steady-state creep on stabilized 20% Cr-25% Ni austenitic stainless steels*. in *Creep strength in steel and high-temperature alloys, proceedings of a meeting on creep strength in steel and high-temperature alloys organized by The Iron and Steel Institute, held at the University of Sheffield on 20-22 September 1972*. 1974.

67. Blum, W., P. Eisenlohr, and F. Breutinger, *Understanding creep—a review.* Metallurgical and Materials Transactions A, 2002. **33**: p. 291-303.

68. Kassner, M.E., *Fundamentals of creep in metals and alloys*. 2015: Butterworth-Heinemann.

69. Shrestha, T., M. Basirat, I. Charit, G.P. Potirniche, K.K. Rink, and U. Sahaym, *Creep deformation mechanisms in modified 9Cr–1Mo steel.* Journal of Nuclear Materials, 2012. **423**(1-3): p. 110-119.

70. Svoboda, J., L. Kuncicka, N. Luptakova, A. Weiser, and P. Dymacek, *Fundamental Improvement of Creep Resistance of New-Generation Nano-Oxide Strengthened Alloys via Hot Rotary Swaging Consolidation.* Materials (Basel), 2020. **13**(22).

71. Kassner, M.E. and K. Smith, *Low temperature creep plasticity*. Journal of materials research and technology, 2014. **3**(3): p. 280-288.

72. Poirier, J.-P., *Creep of crystals: high-temperature deformation processes in metals, ceramics and minerals*. 1985: Cambridge University Press.

73. Raj, R. and M. Ashby, *On grain boundary sliding and diffusional creep.* Metallurgical transactions, 1971. **2**: p. 1113-1127.

74. Owen, D.M. and T.G. Langdon, *Low stress creep behavior: An examination of Nabarro—Herring and Harper—Dorn creep.* Materials Science and Engineering: A, 1996. **216**(1-2): p. 20-29.

75. Kassner, M., P. Kumar, and W. Blum, *Harper–dorn creep*. International journal of plasticity, 2007. **23**(6): p. 980-1000.

76. Lüthy, H., R.A. White, and O.D. Sherby, *Grain boundary sliding and deformation mechanism maps.* Materials Science and Engineering, 1979. **39**(2): p. 211-216.

77. Langdon, T., *A unified approach to grain boundary sliding in creep and superplasticity.* Acta metallurgica et materialia, 1994. **42**(7): p. 2437-2443.

78. Mohamed, F.A. and T.G. Langdon, *The transition from dislocation climb to viscous glide in creep of solid solution alloys.* Acta metallurgica, 1974. **22**(6): p. 779-788.

79. Weertman, J., *Theory of steady-state creep based on dislocation climb.* Journal of Applied Physics, 1955. **26**(10): p. 1213-1217.

80. Weertman, J., *Steady-state creep through dislocation climb.* Journal of Applied Physics, 1957. **28**(3): p. 362-364.

81. Mohamed, F.A., *Incorporation of the Suzuki and the Fisher interactions in the analysis of creep behavior of solid solution alloys.* Materials Science and Engineering, 1983. **61**(2): p. 149-165.

82. Klueh, R., *Discontinuous creep in short-range order alloys.* Materials Science and Engineering, 1982. **54**(1): p. 65-80.

83. Weertman, J., *Theory of internal stress for class I high temperature creep alloys.* Acta Metallurgica, 1977. **25**(12): p. 1393-1401.

84. Jeong, H., H. Park, H. Kang, and W. Kim, *Operation of solute-drag creep in an AlCoCrFeMnNi high-entropy alloy and enhanced hot workability.* Journal of Alloys and Compounds, 2020. **824**: p. 153829.

85. Leighly, H.P., *Recrystallization and grain growth in commercial titanium*. 1952: University of Illinois at Urbana-Champaign.

86. Marquis, E.A. and D.C. Dunand, *Model for creep threshold stress in precipitation-strengthened alloys with coherent particles.* Scripta Materialia, 2002. **47**(8): p. 503-508.

87. Lagneborg, R. and B. Bergman, *The stress/creep rate behaviour of precipitation-hardened alloys.* Metal Science, 1976. **10**(1): p. 20-28.

88. Mishra, R., T. Bieler, and A. Mukherjee, *Superplasticity in powder metallurgy aluminum alloys and composites.* Acta metallurgica et materialia, 1995. **43**(3): p. 877-891.

89. Abe, F., *Strengthening mechanisms in steel for creep and creep rupture*, in *Creep-resistant steels*. 2008, Elsevier. p. 279-304.

90. Srolovitz, D.J., R.A. Petkovic-luton, and M.J. Litton, *Diffusional relaxation of the dislocation-inclusion repulsion.* Philosophical Magazine A, 1983. **48**(5): p. 795-809.

91. Arzt, E. and D. Wilkinson, *Threshold stresses for dislocation climb over hard particles: the effect of an attractive interaction.* Acta Metallurgica, 1986. **34**(10): p. 1893-1898.

92. Evans, H. and G. Knowles, *Threshold stress for creep in dispersion-strengthened alloys.* Metal Science, 1980. **14**(7): p. 262-266.

93. Mishra, R., T. Nandy, and G. Greenwood, *The threshold stress for creep controlled by dislocation-particle interaction.* Philosophical Magazine A, 1994. **69**(6): p. 1097-1109.

94. Burton, B., *On the mechanism of the inhibition of diffusional creep by second phase particles.* Materials Science and Engineering, 1973. **11**(6): p. 337-343.

95. Ashby, M., *Results and consequences of a recalculation of the frank-read and the orowan stress.* Acta Metallurgica, 1966. **14**(5): p. 679-681.

96. Allen, M.P., *Introduction to molecular dynamics simulation.* Computational soft matter: from synthetic polymers to proteins, 2004. **23**(1): p. 1-28.

97. Binder, K., J. Horbach, W. Kob, W. Paul, and F. Varnik, *Molecular dynamics simulations.* Journal of Physics: Condensed Matter, 2004. **16**(5): p. S429.

98. Hansson, T., C. Oostenbrink, and W. van Gunsteren, *Molecular dynamics simulations.* Current opinion in structural biology, 2002. **12**(2): p. 190-196.

99. Vakis, A.I., V.A. Yastrebov, J. Scheibert, L. Nicola, D. Dini, C. Minfray, A. Almqvist, M. Paggi, S. Lee, and G. Limbert, *Modeling and simulation in tribology across scales: An overview.* Tribology International, 2018. **125**: p. 169-199.

100. Lee, J.G., *Computational materials science: an introduction*. 2016: CRC press.

101. Lindahl, E., *Molecular dynamics simulations.* Molecular modeling of proteins, 2015: p. 3-26.

102. Tuckerman, M.E. and G.J. Martyna, *Understanding modern molecular dynamics: Techniques and applications*. 2000, ACS Publications. p. 159-178.

103. NOSÉ, S.I., *A molecular dynamics method for simulations in the canonical ensemble.* Molecular Physics, 2002. **100**(1): p. 191-198.

104. van Gunsteren, W.F. and A.E. Mark, *Validation of molecular dynamics simulation.* The Journal of chemical physics, 1998. **108**(15): p. 6109-6116.

105. Daw, M.S., S.M. Foiles, and M.I. Baskes, *The embedded-atom method: a review of theory and applications.* Materials Science Reports, 1993. **9**(7-8): p. 251-310.

106. Liao, X., H. Gong, Y. Chen, G. Liu, T. Liu, R. Shu, Z. Liu, W. Hu, F. Gao, and C. Jiang, *Interatomic potentials and defect properties of Fe–Cr–Al alloys.* Journal of Nuclear Materials, 2020. **541**: p. 152421.

107. Liao, X., Y. Chen, H. Gong, T. Liu, H. Deng, W. Hu, and F. Gao, *The stability and behavior of Cr-rich α' precipitates under cascade damage in Fe-15Cr-8Al ternary alloys: An atomic-scale simulation study.* Journal of Nuclear Materials, 2022. **570**.

108. Liu, Z., Q. Han, Y. Guo, J. Lang, D. Shi, Y. Zhang, Q. Huang, H. Deng, F. Gao, and B. Sun, *Development of interatomic potentials for Fe-Cr-Al alloy with the particle swarm optimization method.* Journal of Alloys and Compounds, 2019. **780**: p. 881-887.

109. Lindahl, E.R., *Molecular dynamics simulations.* Molecular modeling of proteins, 2008: p. 3-23.

110. Ennis, P., *a. Zielinska-Lipiec, O. Wachter, a. Czyrska-Filemonowicz, Microstructural stability and creep rupture strength of the martensitic steel P92 for advanced power plant.* Acta Mater, 1997. **45**(12): p. 4901-4907.

111. Wasilkowska, A., M. Bartsch, U. Messerschmidt, R. Herzog, and A. Czyrska-Filemonowicz, *Creep mechanisms of ferritic oxide dispersion strengthened alloys.* Journal of materials processing technology, 2003. **133**(1-2): p. 218-224.

112. Ukai, S., S. Kato, T. Furukawa, and S. Ohtsuka, *High-temperature creep deformation in FeCrAl-oxide dispersion strengthened alloy cladding.* Materials Science and Engineering: A, 2020. **794**.

113. Sugino, Y., S. Ukai, N. Oono, S. Hayashi, T. Kaito, S. Ohtsuka, H. Masuda, S. Taniguchi, and E. Sato, *High temperature deformation mechanism of 15CrODS ferritic steels at cold-rolled and recrystallized conditions.* Journal of Nuclear Materials, 2015. **466**: p. 653-657.

114. Sugino, Y., S. Ukai, B. Leng, N. Oono, S. Hayashi, T. Kaito, and S. Ohtsuka, *Grain boundary sliding at high temperature deformation in cold-rolled ODS ferritic steels.* Journal of Nuclear Materials, 2014. **452**(1-3): p. 628-632.

115. Murty, K.L., J. Ravi, and Wiratmo, *Transitions in creep mechanisms and creep anisotropy in Zr□1Nb□1Sn□0.2Fe sheet.* Nuclear Engineering and Design, 1995. **156**(3): p. 359-371.

116. Murty, K.L., G. Dentel, and J. Britt, *Effect of temperature on transitions in creep mechanisms in class-A alloys.* Materials Science and Engineering: A, 2005. **410-411**: p. 28-31.

117. Murty, K.L., *Transition from class I to class II creep behaviors at low stresses in Pb-9Sn.* The Philosophical Magazine: A Journal of Theoretical Experimental and Applied Physics, 1974. **29**(2): p. 429-431.

118. Shahbeigi Roodposhti, P., A. Sarkar, K.L. Murty, and R.O. Scattergood, *Effects of Microstructure and Processing Methods on Creep Behavior of AZ91 Magnesium Alloy.* Journal of Materials Engineering and Performance, 2016. **25**(9): p. 3697-3709.

119. Charit, I. and K.L. Murty, *Creep behavior of niobium-modified zirconium alloys.* Journal of Nuclear Materials, 2008. **374**(3): p. 354-363.

120. Chokshi, A. and T. Langdon, *Characteristics of creep deformation in ceramics.* Materials Science and Technology, 1991. **7**(7): p. 577-584.

121. Alomari, A.S., N. Kumar, and K. Murty, *Creep behavior and microstructural evolution of a Fe-20Cr-25Ni (mass percent) austenitic stainless steel (Alloy 709) at elevated temperatures.* Metallurgical and Materials Transactions A, 2019. **50**: p. 641-654.

122. Graham, D. and D.H. Tomlin, *Self-diffusion in iron.* Philosophical Magazine, 1963. **8**(93): p. 1581-1585.

123. Zhang, B., *Calculation of self-diffusion coefficients in iron.* AIP Advances, 2014. **4**(1).

124. Arivu, M., A. Hoffman, J. Duan, H. Wen, R. Islamgaliev, and R. Valiev, *Severe plastic deformation assisted carbide precipitation in Fe-21Cr-5Al alloy.* Materials Letters, 2019. **253**: p. 78-81.

125. Isik, M.I., A. Kostka, V.A. Yardley, K.G. Pradeep, M.J. Duarte, P.P. Choi, D. Raabe, and G. Eggeler, *The nucleation of Mo-rich Laves phase particles adjacent to M23C6 micrograin boundary carbides in 12% Cr tempered martensite ferritic steels.* Acta Materialia, 2015. **90**: p. 94-104.

126. Hoelzer, D.T., *History and outlook of ODS/NFA ferritic alloys for nuclear applications*. 2018, Oak Ridge National Lab.(ORNL), Oak Ridge, TN (United States).

127. Alam, M.E., S. Pal, S.A. Maloy, and G.R. Odette, *On delamination toughening of a 14YWT nanostructured ferritic alloy.* Acta Materialia, 2017. **136**: p. 61-73.

128. Bhattacharyya, D., P. Dickerson, G.R. Odette, S.A. Maloy, A. Misra, and M.A. Nastasi, *On the structure and chemistry of complex oxide nanofeatures in nanostructured ferritic alloy U14YWT.* Philosophical Magazine, 2012. **92**(16): p. 2089-2107.

129. Dahl, M.E., C.A. Lavender, K.M. McCoy, R.P. Omberg, and M.T. Smith, *Processing and Characterization of Pilgered 14YWT Tubing*. 2019, Pacific Northwest National Lab.(PNNL), Richland, WA (United States).

130. Eftink, B.P., C.R. Lear, T.J. Lienert, and S.A. Maloy, *Characterization of 14YWT & ODS Base Metals*. 2019, Los Alamos National Lab.(LANL), Los Alamos, NM (United States).

131. Hoelzer, D.T., *Report on the Production by Mechanical Alloying of New Heats of 14YWT*. 2019, Oak Ridge National Lab.(ORNL), Oak Ridge, TN (United States).

132. Miller, M., D. Hoelzer, S. Babu, E. Kenik, and K. Russell, *High Temperature Microstructural Stability of a MA/ODS Ferritic Alloy*. High Temperature Alloys: Processing for Properties, 2003.

133. Cunningham, N., Y. Wu, G. Odette, D. Hoelzer, and S. Maloy, *Characterization of a larger best practice heat of 14YWT in annealed powder, HIP consolidated and extruded forms.* Fusion Materials Semiannual Progress Report for Period Ending June, 2013. **30**: p. 15-26.

134. Cunningham, N.J., Y. Wu, A. Etienne, E.M. Haney, G.R. Odette, E. Stergar, D.T. Hoelzer, Y.D. Kim, B.D. Wirth, and S.A. Maloy, *Effect of bulk oxygen on 14YWT nanostructured ferritic alloys.* Journal of Nuclear Materials, 2014. **444**(1-3): p. 35-38.

135. Miller, M.K., C.M. Parish, and Q. Li, *Advanced oxide dispersion strengthened and nanostructured ferritic alloys.* Materials Science and Technology, 2013. **29**(10): p. 1174-1178.

136. Pal, S., M.E. Alam, S.A. Maloy, D.T. Hoelzer, and G.R. Odette, *Texture evolution and microcracking mechanisms in as-extruded and cross-rolled conditions of a 14YWT nanostructured ferritic alloy.* Acta Materialia, 2018. **152**: p. 338-357.

137. Hayashi, T., P.M. Sarosi, J.H. Schneibel, and M.J. Mills, *Creep response and deformation processes in nanocluster-strengthened ferritic steels.* Acta Materialia, 2008. **56**(7): p. 1407-1416.

138. Han Kim, J., T. Sang Byun, and D.T. Hoelzer, *Stress relaxation behavior of nanocluster-strengthened ferritic alloy at high temperatures.* Journal of Nuclear Materials, 2012. **425**(1-3): p. 147-155.

139. Brandes, M.C., L. Kovarik, M.K. Miller, G.S. Daehn, and M.J. Mills, *Creep behavior and deformation mechanisms in a nanocluster strengthened ferritic steel.* Acta Materialia, 2012. **60**(4): p. 1827-1839.

140. Hoelzer, D.T., I. Stinson, and C. Massey, *High-Temperature Tensile and Creep Test Results on Thin Wall Tube Specimens of ODS Alloys 14YWT and OFRAC*. 2022, Oak Ridge National Lab.(ORNL), Oak Ridge, TN (United States).

141. Charit, I., Y.T. Zhu, S.A. Maloy, and P.K. Liaw, *Mechanical and Creep Behavior of Advanced Materials: A SMD Symposium Honoring Professor K. Linga Murty*. 2017: Springer.

142. Chang, K., F. Meng, F. Ge, G. Zhao, S. Du, and F. Huang, *Theory-guided bottom-up design of the FeCrAl alloys as accident tolerant fuel cladding materials.* Journal of Nuclear Materials, 2019. **516**: p. 63-72.

143. Heino, P., H. Häkkinen, and K. Kaski, *Molecular-dynamics study of mechanical properties of copper.* Europhysics Letters, 1998. **41**(3): p. 273.

144. Khoei, A. and M. Khorrami, *Mechanical properties of graphene oxide: A molecular dynamics study.* Fullerenes, Nanotubes and Carbon Nanostructures, 2016. **24**(9): p. 594-603.

145. Li, Q.-K. and M. Li, *Molecular dynamics simulation of intrinsic and extrinsic mechanical properties of amorphous metals.* Intermetallics, 2006. **14**(8-9): p. 1005-1010.

146. Herman, J., M. Govednik, S.P. Patil, and B. Markert, *Molecular Dynamics Simulation Study of the Mechanical Properties of Nanocrystalline Body-Centered Cubic Iron.* Surfaces, 2020. **3**(3): p. 381-391.

147. Beeler, B., S. Hu, Y. Zhang, and Y. Gao, *A improved equation of state for Xe gas bubbles in γU-Mo fuels.* Journal of Nuclear Materials, 2020. **530**: p. 151961.

148. Beeler, B., A. Casagranda, L. Aagesen, Y. Zhang, and S. Novascone, *Atomistic calculations of the surface energy as a function of composition and temperature in γ U–Zr to inform fuel performance modeling.* Journal of Nuclear Materials, 2020. **540**: p. 152271.

149. Li, Y.P., M.S. Yu, G. Ran, N. Gao, Y. Chen, Q. Han, H. Wang, Z.H. Zhou, and J.C. Huang, *In situ transmission electron microscopy study and molecular dynamics simulation of dislocation loop evolution in FeCrAl alloys under Fe+ irradiation.* Materials Today Energy, 2021. **21**.

150. Yao, H., T. Ye, J. Wu, Y. Wu, C. Yin, and P. Chen. *Creep Properties of FeCrAl Alloy at High Temperature Under Neutron Irradiation*. in *International Conference on Nuclear Engineering*. 2022. American Society of Mechanical Engineers.

151. Yao, H., T. Ye, P. Wang, J. Wu, J. Zhang, and P. Chen, *Structural Evolution and Transitions of Mechanisms in Creep Deformation of Nanocrystalline FeCrAl Alloys.* Nanomaterials (Basel), 2023. **13**(4).

152. Yao, H., T. Ye, W. Yu, P. Wang, J. Wu, Y. Wu, and P. Chen, *Atomic-scale investigation of creep behavior and deformation mechanism in nanocrystalline FeCrAl alloys.* Materials & Design, 2021. **206**: p. 109766.

153. Li, Y., Z. Sun, N. Liao, Z. Cao, X. Liu, Y. Li, Y. Ding, X. Qiu, and G. Ran, *Formation of helical dislocations mediated by interstitials in ion irradiated FeCrAl alloy.* Journal of Nuclear Materials, 2023. **579**.

154. Yu, M., Z. Wang, F. Wang, W. Setyawan, X. Long, Y. Liu, L. Dong, N. Gao, F. Gao, and X. Wang, *Coupled effect of Cr and Al on interactions between a prismatic interstitial dislocation loop and an edge dislocation line in Fe-Cr-Al alloy.* Acta Materialia, 2023. **245**.

155. Ye, T., Z. Wang, Y. Wu, J. Zhang, P. Chen, M. Wang, W. Tian, G.H. Su, and S. Qiu, *Molecular dynamics simulation of tensile deformation behavior of single-crystal Fe–Cr–Al before and after irradiation.* Journal of Materials Research, 2022. **38**(3): p. 828-840.

156. Atomic, L.-s. and M.M.P. Simulator, *Lammps.* available at: http:/lammps. sandia. gov, 2013.

157. Yoo, S., X.C. Zeng, and J.R. Morris, *The melting lines of model silicon calculated from coexisting solid-liquid phases.* J Chem Phys, 2004. **120**(3): p. 1654-6.

158. Belonoshko, A.B., N.V. Skorodumova, A. Rosengren, and B. Johansson, *Melting and critical superheating.* Physical Review B, 2006. **73**(1).

159. Stukowski, A., *Visualization and analysis of atomistic simulation data with OVITO–the Open Visualization Tool.* Modelling and simulation in materials science and engineering, 2009. **18**(1): p. 015012.

160. Yang, H., Y. Lü, M. Chen, and Z. Guo, *A molecular dynamics study on melting point and specific heat of Ni3Al alloy.* Science in China Series G: Physics, Mechanics and Astronomy, 2007. **50**(4): p. 407-413.

161. Komanduri, R., N. Chandrasekaran, and L. Raff, *Molecular dynamics (MD) simulation of uniaxial tension of some single-crystal cubic metals at nanolevel.* International Journal of Mechanical Sciences, 2001. **43**(10): p. 2237-2260.

162. Sun, Z.H., J. Zhang, G.X. Xin, L. Xie, L.C. Yang, and Q. Peng, *Tensile mechanical properties of CoCrFeNiTiAl high entropy alloy via molecular dynamics simulations.* Intermetallics, 2022. **142**: p. 107444.

163. Koyanagi, J., N. Takase, K. Mori, and T. Sakai, *Molecular dynamics simulation for the quantitative prediction of experimental tensile strength of a polymer material.* Composites Part C: Open Access, 2020. **2**: p. 100041.

164. Zhang, L., K. Qian, J. Huang, M. Liu, and Y. Shibuta, *Molecular dynamics simulation and machine learning of mechanical response in non-equiatomic FeCrNiCoMn high-entropy alloy.* Journal of Materials Research and Technology, 2021. **13**: p. 2043-2054.